PRELIMINARY DESIGN OF A LIQUID BIPROPELLANT
MICROFABRICATED ROCKET ENGINE

by

OMAR M. AL-MIDANI

Bachelor of Science in Aerospace Engineering, University of California, Los Angeles (1996)

Submitted to the Department of Aeronautics and Astronautics
in partial fulfillment of the requirements for the degree of

MASTER OF SCIENCE

at the

MASSACHUSETTS INSTITUTE OF TECHNOLOGY

June 1998

© Omar M. Al-Midani. All rights reserved.

Author_____
Department of Aeronautics and Astronautics
June, 1998

Certified by_____
Professor Alan H. Epstein
R. C. Maclaurin Professor of Aeronautics and Astronautics
Thesis Supervisor

Accepted by_____
Associate Professor Jaime Peraire
Chairman, Department Graduate Committee

PRELIMINARY DESIGN OF A LIQUID BIPROPELLANT MICROFABRICATED ROCKET ENGINE

by

OMAR M. AL-MIDANI

ABSTRACT

This thesis discusses the design of a microfabricated rocket engine. Micro-rockets feature a thrust to weight ratio up to two orders of magnitude greater than conventional rocket motors at small thrust levels and hence are very attractive for satellite propulsion applications and micro-satellite development.

All major rocket components have been characterized and evaluated for micro-scale operation. These include a 300 atm pumping system, a 3000 K and 125 atm combustion chamber and a Mach 3.5 thrusting nozzle. Studies indicate that a turbopump system is feasible while further investigations on bearings are required to fully validate the concept. The viability of the combustion chamber is believed to be dependent on the mixing performance of an innovative injection scheme which features inter-digitated fuel/oxidizer jets impinging at a 180° angle. The nozzle is projected to perform satisfactorily, incurring a mere 2% loss in thrust according to 2D CFD calculations. Modeling of the system transients has indicated an acceleration time on the order of 0.1 sec. as well as notable sensitivities to the injector diameter and turbine blade turning angles.

The analysis suggests that the micro-rocket engine concept is feasible and identifies the engineering challenges ahead.

Thesis Supervisor: Professor Alan H. Epstein
Title: R. C. Maclaurin Professor of Aeronautics and Astronautics

ACKNOWLEDGMENTS

CONTENTS

LIST OF FIGURES

LIST OF TABLES

NOMENCLATURE

Roman

A_t	Throat area
A_e	Nozzle exit area
A_{eff}	Nozzle exit effective area (accounting for blockage)
b	Electrostatic motor height
Bi	Biot number
c	Journal bearing clearance
C_D	Injector discharge coefficient
CFD	Computational Fluid Dynamics
Cp	Heat capacity
d_e	Nozzle exit width
d_{inj}	Injector diameter
d_t	Throat width
e	Number of stator electrodes
e_c	Bearing eccentricity
e_{max}	Maximum number of electrodes
E	Electric field
f	Cooling passage fricition coefficient (related to surface roughness)
F	Frequency
F_b	Bearing load
F_{max}	Maximum frequency
g	Gravitational acceleration

G	Motor gap height
h	Height or depth (general)
h	Heat transfer coefficient
h_{fg}	Latent heat of vaporization
h_k	Enthalpy of species k
k	Thermal conductivity (silicon)
K	Nozzle aspect ratio
I	Pumping system inertia
I_{sp}	Specific impulse ($\frac{T}{\dot{m}g}$)
L	Length (general)
L^*	Chamber characteristic length
LOX	Liquid oxygen
$\dot{m}$	Mass flow rate
ma	Journal bearing mass
M	Electrode-pole count
M	Mach number
Ma	Non dimensional journal bearing mass parameter
N	Turbomachinery wheel speed [revs/sec]
Nu	Nusselt number
O/F	Oxydizer to fuel mass ratio
P	Pressure
P_a	Power dissipation in annulus gap
P_{avail}	Available pumping power
P_e	Nozzle exit flow pressure
$Peri$	Perimeter
P_g	Power dissipation in the motor gap
P_{motor}	Electrostatic micro-motor power
P_{pump}	Pumping power
P_t	Total pressure
P_∞	Ambiant pressure
Pr	Prandtl number
$\ddot{q}$	Heat flux

Q	Chamber heat loss
r	Radius
Re	Reynolds number
R_g	Gas constant
R_i	Inner radius
R_o	Outer radius
T	Rocket thrust
T_{ideal}	Ideal thrust
$T_{j=1}, T_{j=2}$	Temperature at grid indices j=1 & j=2 (j=1 denotes the wall boundary)
T_{loss}	Thrust loss ($T_{ideal} - T$)
T	Torque
T_t	Total temperature
u	Radial flow velocity (pump)
u	x-component of flow velocity (nozzle)
U_j	Jet velocity
U_{wall}	Fluid velocity at the wall
U_∞	Free stream velocity
v	Tangential flow velocity
V	Voltage
V	Volume
w	Cooling passage width
W	Rocket engine weight
W_b	Non dimensional bearing load parameter
x	Mixture quality
x_k	Mass fraction of species k
X_{tt}	Martinelli perameter
Y_j	Nozzle y-coordinate at index j

Greek

β_b	turbine nozzle vane turning angle
β_b'	Rotor blade incidence angle
β_c'	Rotor blade turning angle
Δ	Rotor insulator thickness
Δ	Change in property or state
ϵ_c	Bearing eccentricity ratio $\left(\frac{e_c}{c}\right)$
ϵ	Nozzle area expansion ratio
ϵ_B	Dielectric constant for the rotor insulator material
ϵ_o	Dielectric constant for air
η_p	Pump efficiency
η_r	Electric motor efficiency (related to signal resolution)
γ	Specific heat ratio
λ	Bearing aspect ratio $\left(\frac{b}{R_o}\right)$
μ	Viscosity
ω	Angular velocity
$\dot{\omega}$	Angular acceleration
ρ	Density
σ	Shear stress
τ_{comb}	Combustion kinetics minimum residence time (Chapter 4)
τ_{comb}	Combustion time lag (mixing and combustion) (Chapter 5)
τ_{noz}	Flow residence time in the nozzle
τ_{res}	Flow residence time in the chamber
φ	Electrode density $\left(\frac{e}{M}\right)$
ξ	Injector jet coordinate in the arc direction

Subscripts

1	Thrusting chamber inner wall

2	Thrusting chamber outer wall
$1P$	Single phase
$2P$	Two phase
a	Turbine nozzle vane inlet station
b	Turbine rotor inlet station
c	Turbine rotor exit station
$boil$	Boiling state
$bulk$	Bulk (fluid temperature)
ch	Chamber
$char$	Characteristic
$conv$	Convective
$comb$	Combustion
$crit$	Critical fluid state
e	Exit condition
$fluid$	Fluid
hx	Heat exchanger
in (or i)	Inlet
inj	Injector
inj, e	Injector exit
$inje, i$	Injecor inlet
k	Chemical species index
l	Liquid state
p	Pump
p, i	Pump inflow
p, o	Pump outflow
ref	Calculated at an indicated reference state
sat	Saturation
si	Silicon
t, i	Turbine inflow
t, o	Turbine outflow
v	Vapor state
$wall$	Conditions at the wall boundary

Other Notations

$\overline{[\cdot]}$ Average value

$X_{|[\cdot]}$ X is evaluated at $[\cdot]$

CHAPTER 1

MICRO-ROCKET ENGINE CONCEPT

1.1 Introduction

Micro-rocket engines [†] are highly compact thrusting units capable of delivering a thrust
to weight ratio which surpasses current rocket engines by up to two orders of magnitude.
While several innovative applications have been proposed for the device, micro-rocket engine
applications are currently being investigated for satellite attitude control.

Unlike conventional micro-thrusters which utilize pressurized propellant tanks, micro-rocket
engines feature an integrated pumping system which eliminates the need for high pressure
fluid storage thus greatly reducing structural tank mass. Satellite buses with smaller tank
volumes and lower thruster unit mass would then benefit from a greater payload carrying
capacity or an equivalent increase in propellant mass for a longer life in orbit. Further
advances in the technology may even lead to the development of micro-satellites as fully
integrated micro-electronic and micro-mechanical systems capable of being mass produced
and deployed at a fraction of the present cost.

The success of this innovation ultimately depends on the ability to build pumps using cur-
rent microfabrication techniques. Efforts are presently being pursued at the Massachusetts
Institute of Technology (towards the development of a micro-gas turbine engine [5]) where
research on a micro-compressor will advance the understanding of the design and manu-

---

[†]Micro-rocket engines have first been proposed for orbit maintenance and control by Adam P. London
in a master thesis on "A Systems Study of Propulsion Technologies for Orbit and Attitude Control for
Microspacecraft" (see Reference [15]).

facturing processes involved in building the liquid micro-pumps. While preliminary studies have been performed on the pumping system, research work to date has been primarily focused on designing the rocket engine around its liquid pumps. Experimental testing of the rocket will initially require the use of an externally pressurized propellant feed system as a temporary replacement for the integrated pumps.

1.2   Rocket Layout

The micro-rocket engine layout ([14] , [16]) is presented below (see Figure 1-1), illustrating the valves, pumps and cooling passages. Dimensions are provided for reference but do not necessarily dictate the current baseline design for the device. Indeed, specifications are constantly updated as detailed analyses progress. Most design variables however, are expected to lie within 20% of their suggested preliminary values. A brief summary of the current micro-rocket engine specifications is provided in Table 1.1.
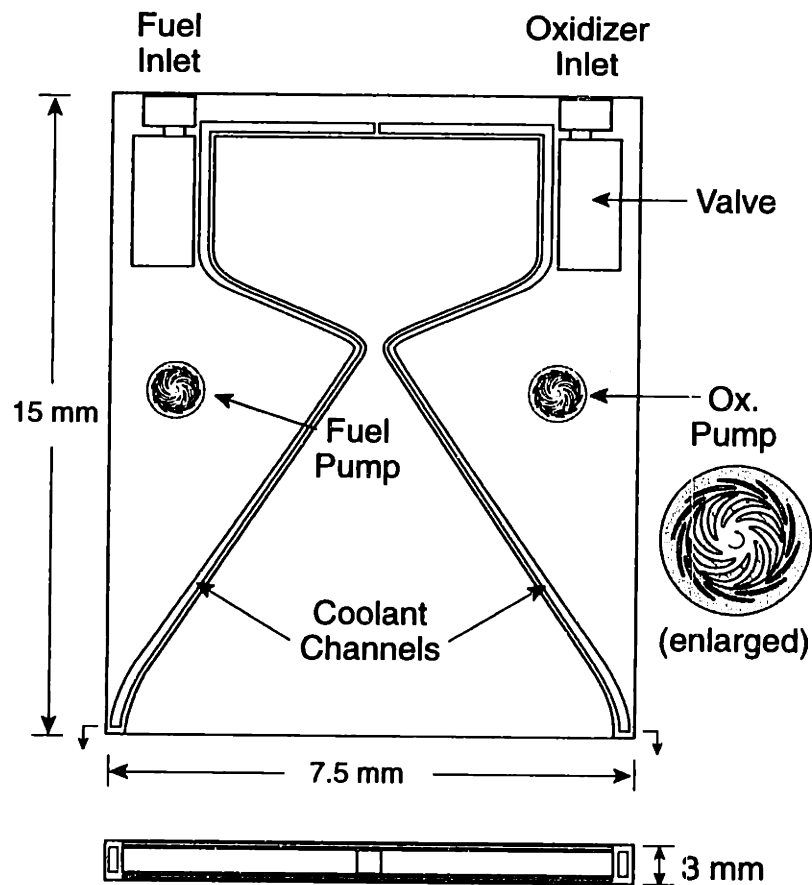
Figure 1-1: Micro-Rocket Engine Layout, [14] & [16].

Thrust	15 N
Mass Flow	5 g/s
Propellants	LOX/Ethanol
Chamber Pressure	125 atm
Pump Power	$\sim$ 75 watts (each)
Structure	Silicon
Thrust/Weight	$\sim$ 10,000:1

Table 1.1: Micro-Rocket Engine Specifications.

1.3 Thrust to Weight Ratio

Rocket thrust (T) essentially depends on the chamber pressure and the nozzle throat area. One measure of performance is the thrust to weight ratio where the weight only encompasses the engine unit and does not account for the propellant mass. For traditional chemical-solid or liquid bipropellant engines, this number reaches maximum values on the order of 100 [24]. On the other hand, miniaturization allows micro-rocket engines to reach a thrust to weight ratio two orders of magnitude greater ($\sim 10^4$) rendering the engine weight a negligible portion of the overall propulsion system. This can be explained very simply by approximating the rocket thrust as:

$$T \simeq P_{ch} A_t C_F \qquad (1.1)$$

and the engine silicon chip weight as:

$$W \simeq \rho g L \epsilon A_t \qquad (1.2)$$

where P_{ch} is the chamber pressure, A_t the throat area, C_F the thrust coefficient [24], ϵ the nozzle expansion ration [24], L the engine length, ρ the silicon density and g the gravitational acceleration.

Thus if $\epsilon \sim 10$, $P_{ch} \sim 100$ atm $\simeq 10^7$ Pa, $L \sim 10^{-2}$ m, $C_F \sim 1$ and $\rho \sim 1000 \frac{kg}{m^3}$ then:

$$\frac{T}{W} \simeq \frac{10^7}{(10^3)(10)(10^{-2})(10)} \simeq 10^4 \qquad (1.3)$$

Micro-sizing would thus offer substantial weight savings in satellite propulsion systems al-

lowing for additional payload capacity or propellant storage for an extended life in orbit.

1.4 Applications

Micro-rocket engines have initially been proposed for attitude control. Envisioning more powerful thrusting devices however, would require the assembly of a multitude of micro-rockets in a matrix configuration. Applications could range from apogee kick motors, Earth to orbit launches or even rocket assist takeoff and landing for atmospheric vehicles. Table 1.2 illustrates propulsion requirements for a satellite mass on the order of 1000 kg using micro-rockets.

Thrust essentially depends on the nozzle exit area given a fixed expansion ratio (ϵ) and chamber pressure (P_{ch}). Thus a conventional thruster may be replaced by a matrix of mini-thrusters with an equivalent total nozzle exit area. Figure 1-2 illustrates a thrusting matrix as a potential replacement for the larger thruster. As length scales decrease to meso-scales (~ 1 cm), the thruster can conceivably be shown to be fully interchanged by a 1 cm thick thrusting matrix. Ultra-compact and highly modular thrusting plates could then be integrated on almost any flying vehicle such as rockets, satellites or even fighter airplanes.

Application	Thrust [N]	# units
Attitude control	~ 10 (ea)	~ 1
Orbit Maneuvers	$\sim 10^2$	~ 10
Earth Launch	$\sim 10^6 - 10^7$	$\sim 10^5 - 10^6$

Table 1.2: Micro-Rocket Engine Satellite Applications: estimations are based on a satellite mass on the order of 1000 kg [24].

1.5 Manufacturing (Microfabrication)

1.5.1 Concept

Micro-rocket engines are fabricated out of silicon wafers as separate planar layers, stacked and bonded together to create a three dimensional device (see Figure 1-6). Each layer results from an intricate etching process allowing complex planar geometries to be formed along the

24
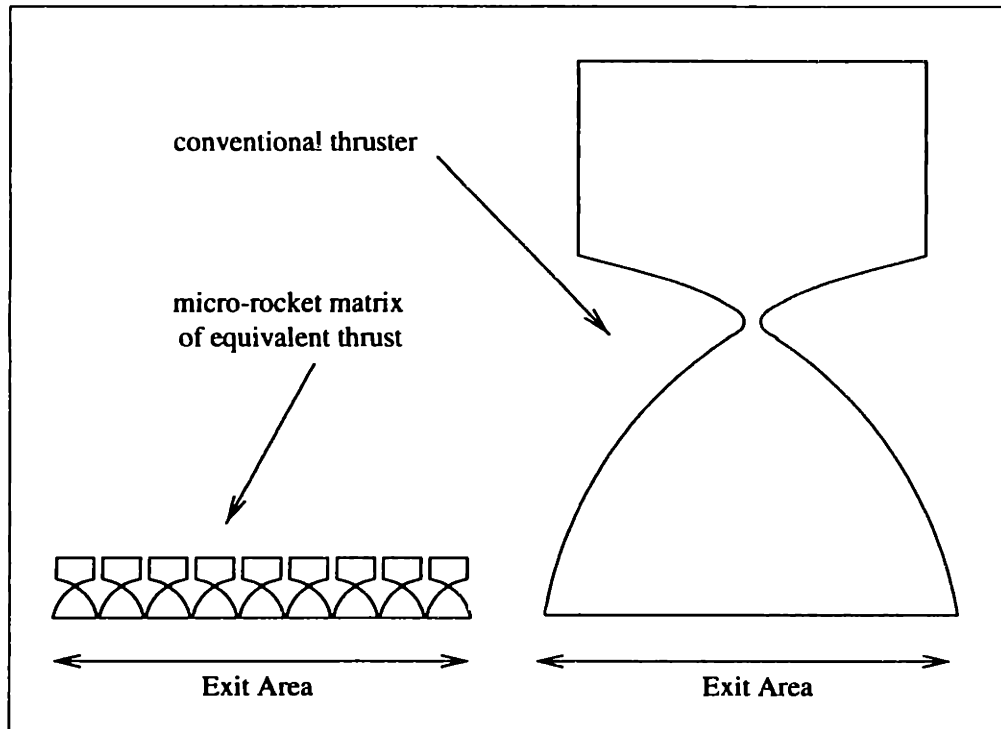
Figure 1-2: Micro-Rocket Thrusting Matrices vs. Conventional Rocket Propulsion Systems.

wafer's depth (see Figure 1-3). The amount of wafers necessary to build the device depends on both its complexity and its design height. Engine height may for example be altered in order to increase thrust by accommodating larger mass flow rates through the chamber. Changing the baseline design thrust requires minimal re-engineering work as most design considerations are intrinsically two-dimensional (to first order) and thus independent of engine height. Complex components such as the micro-pumps require several wafer bonds due to the different geometric planes of extrusion required to build the device. For a turbopump these would include at least five layers: one each for the pumping blades and turbine blades, a third to provide the pump sufficient structural mass and surface area for the journal bearing sleeve, and one each for the pump inlet and outlet.

Additional fabrication complexities also arise when there is a need for three dimensional features (i.e. injectors, cooling passages and ignition). Auto-ignition for example, may require depositing catalytic material along the chamber walls as part of the fabrication process. Moreover, providing an ignition source would necessitate the incorporation of a spark generator inside the chamber along with a shrewd wiring scheme. While these issues

have not yet been addressed, they provide a sense of appreciation for the challenges facing the microfabrication of the rocket engine.

A fabrication demonstration has been performed [16], and Figure 1-3 illustrates a close-up view of the nozzle throat with the cooling passage running along the chamber and nozzle. Note that the passage becomes thinner near the throat due to the higher local heat flux rates (see Figure 4-9). Figure 1-4 features a single micro-rocket engine chip, cut out from a wafer containing several micro-rockets. Figure 1-5 illustrates a typical wafer layout where test structures and different rocket configurations are being manufactured for future testing and experiments. (Micro-pumps have not yet been fabricated).

1.5.2   Technical Implications

Having overviewed the basic concepts concerning the manufacturing of the micro-rocket engine, it is now necessary to underline the technical consequences of such fabrication processes on the performance of the device and its overall functionality.

The etching processes used in microfabrication generally impose limitations on both the geometry and performance of the device by restricting the design to two-dimensional features. Performance impacts translate into a loss in pumping efficiency (no out of plane blade twist in the impeller), viscous losses in the square nozzle corners as well as pressure losses in the sharp injector inlets and outlets. While pump losses are not of main concern in rocket engine design, pressure and viscous losses may significantly affect performance. Partial compensation for these losses has been provided by increasing the pressure head rise of the pump to 300 atm in order to offset undesired pressure drops throughout the engine.

Reproduction costs for microfabricated devices are irrespective of feature detail thus decoupling product complexity from the individual unit cost. Moreover this new type of manufacturing may potentially revolutionize the highly expensive design iteration cycles used in product development today. Technological innovations and product improvements require a great deal of analytical work and computer simulations in order to minimize the higher expenses associated with experiments. Because of its negligible reproduction costs, microfabrication would allow several design configurations to be developed and tested as an ultimate means of understanding the impact and performance of the design. Micro-

fabrication may thus encourage engineers to rethink their traditional design methodologies and adopt more innovative product development processes. In the case of the micro-rocket engine for example, fabrication techniques do not allow the injector design to follow conventional injection design practices and lack of empirical data left some uncertainty regarding the expected mixing performance. While conventional procedures would require computational fluid dynamics (CFD) calculations and mixing experiments to evaluate the present injection scheme, microfabrication allows for cheap manufacturing of several proposed injection schemes which could then be validated during an actual test firing . Research time may therefore be significantly compressed offering greater experimental value and an earlier product delivery date.
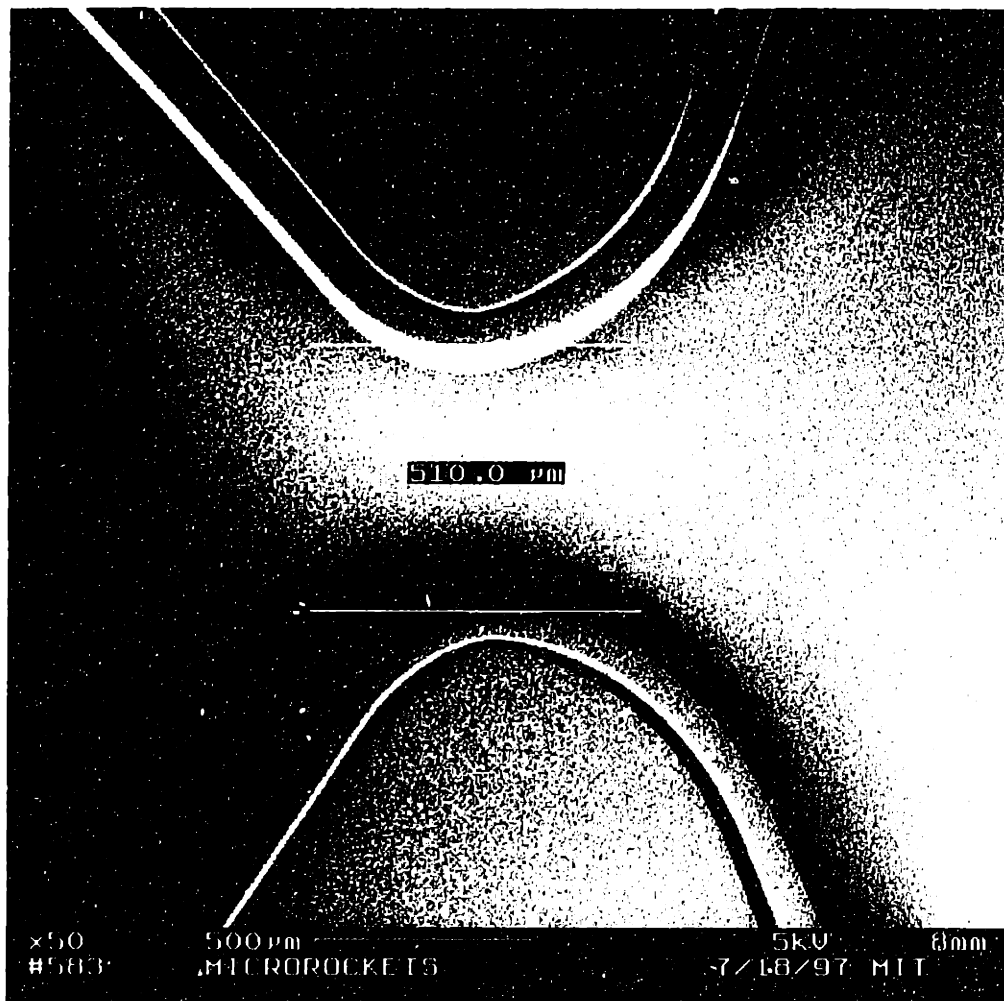
Figure 1-3: Close-Up of the Nozzle Throat [16].

27
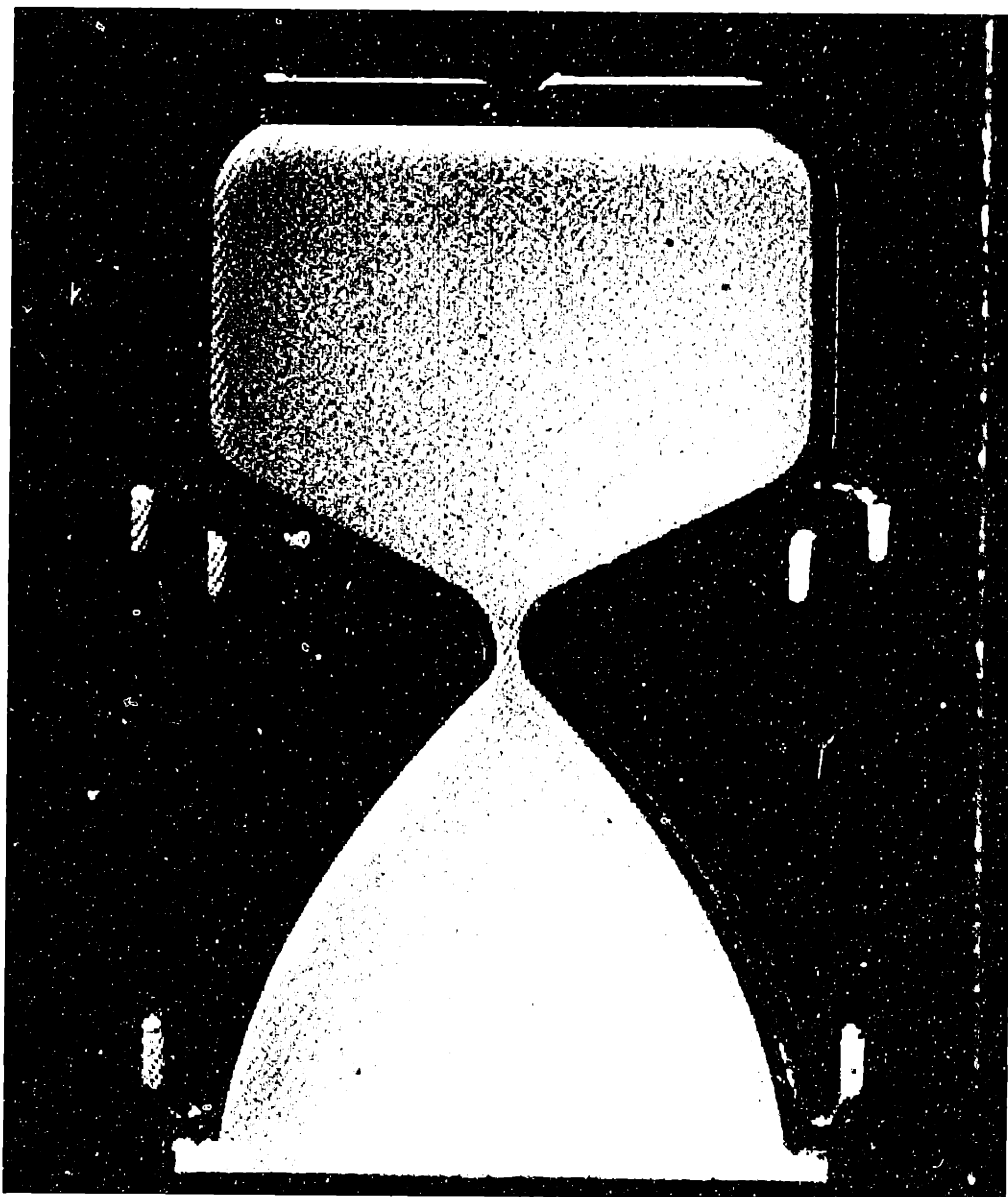
Figure 1-4: Micro-Rocket Engine Chip (1 Layer) [16].
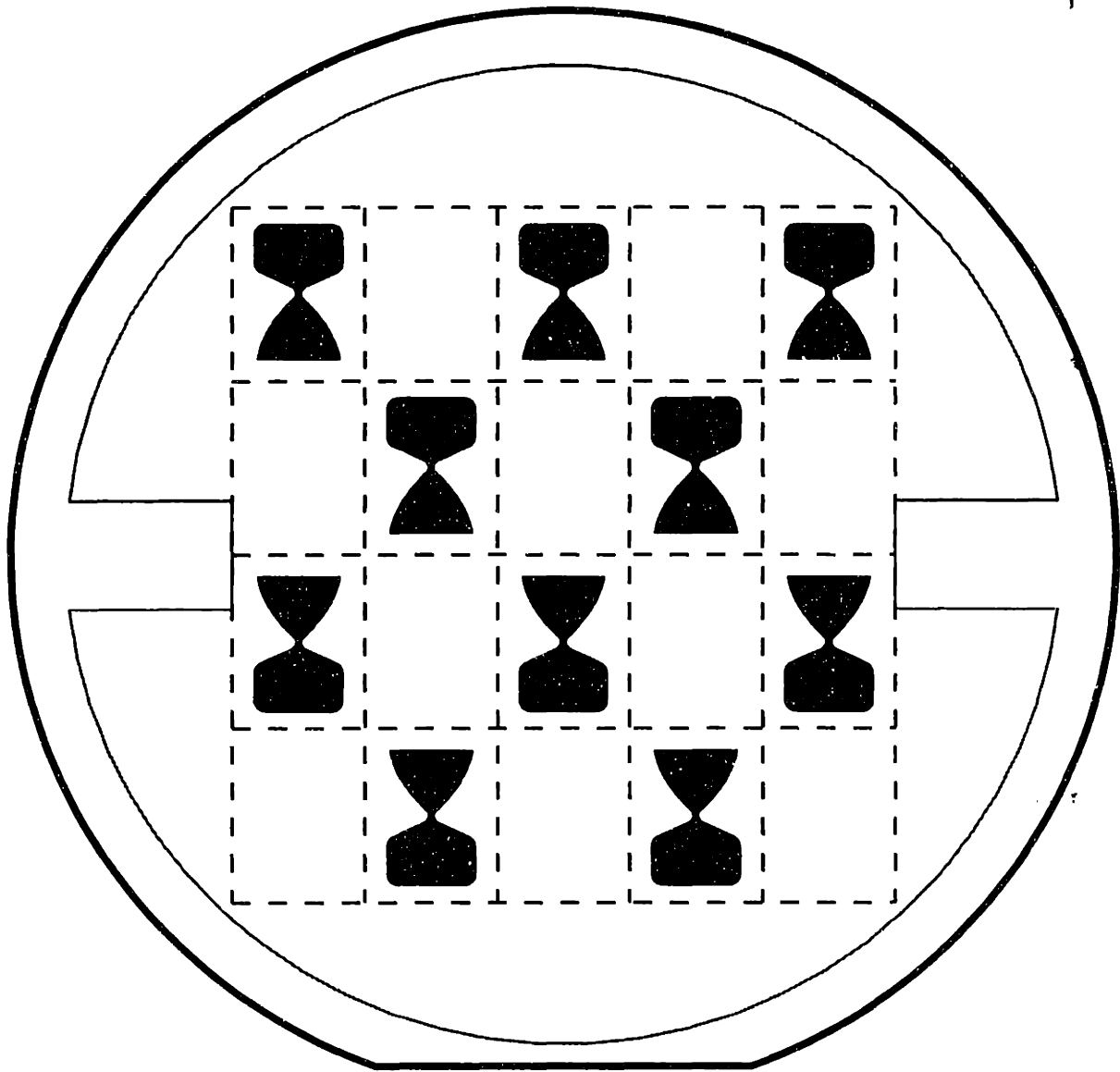
Figure 1-5: Silicon Wafer Featuring a Single Microfabricated Layer [16].
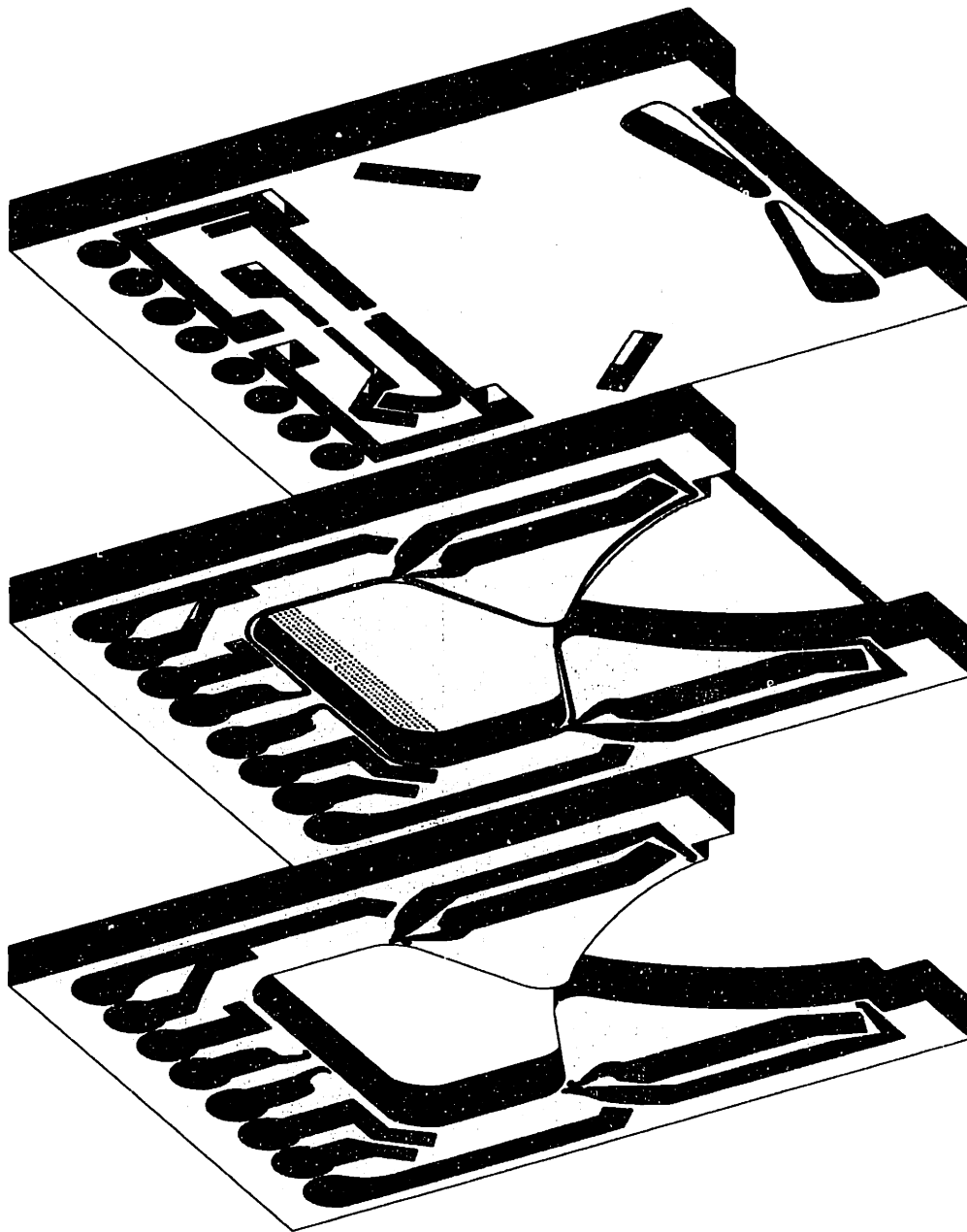
Figure 1-6: Micro-Rocket Engine Wafers Layout and Assembly.

Wafers are shown from their bottom view, suspended above the engine plane of symmetry for a total of 6 wafers for the entire micro-rocket engine (see Reference [16]).

1.6 Project Challenges and Thesis Overview

The ability to manufacture microfabricated rocket engines presents tremendous advantages in delivering fully modular ultra-compact thrusters for a broad range of space applications not to mention possible Earth applications as well. However, several technical challenges need to be addressed before the project may be completed successfully. The following section identifies the various tasks necessary for the development of an operational micro-rocket engine, and outlines the issues tackled in the subsequent chapters of the thesis.

Joint efforts involving design, analysis, experiments and microfabrication expertise are crucial to the success of this project. The following enumerates and explains the various tasks at stake:

Valves

Conventional attitude control thrusters rely on bulky valve systems constituting most of the propulsion system weight. Micro-rockets on the other hand feature an integrated pumping system which eliminates the need for high pressure valve systems. Low pressure micro-valves are however necessary in order to deliver the propellants from the low pressure tanks to the pumping system. Valve design has not yet been pursued.

Pumping

There are two possible pumping configurations including a turbopump and an electro-statically driven pump. Chapter 2 determines the pumping choice and addresses preliminary design issues such as bearing performance and stability. Detailed design of the pump has not yet been pursued.

Combustion

Due to the small scales, the question arises, whether the fuel mixture inside the chamber experiences sufficient residence time necessary for combustion. Complete combustion occurs only after both propellant and oxidizer have properly mixed at the molecular scale. The

characteristic times associated with the chemical processes depend on both pressure and chemical kinetics considerations but do not depend on size. Scaling down of the rocket decreases residence time without reducing the required reaction time. Miniaturization thus imposes limits on combustion and analyses are required in order to determine an appropriate size for the chamber. Chapter 3 tackles this issue.

Injection and Mixing

Chapter 3 also discusses the microfabrication constraints on the injector design and proposes a mixing scheme. Ultimate validation of the design is scheduled to occur during the test firing phase of the project.

Cooling Scheme

Given that chamber and nozzle gas temperatures are 1500° above the melting point of silicon, considerable effort must be invested to provide the rocket adequate cooling. Furthermore thermal stress considerations require fine tuning of the cooling scheme in order to insure quasi-uniform temperatures along the nozzle and chamber walis. An extensive cooling discussion is not provided in this thesis but has been studied as part of a separate research effort [16].

Nozzle Design

Nozzle design is essential in order to determine the effects of length and geometry on performance. Analyses involving CFD calculations are also necessary in order to assess the viscous losses in the device as well as their consequences on efficiency. Obtaining accurate temperature distributions for the nozzle contour is also crucial in establishing an isothermal wall cooling scheme. Chapter 4 explores these issues in detail.

Dynamic Modeling

Dynamic modeling of the micro-rocket engine is necessary to estimate the system transients as well as to determine the start-up feasibility envelope of the engine. System modeling

also generates useful information concerning the sensitivities of the device to key design parameters and provides insight on the inherent stability of the system. Modeling and simulations of the micro-rocket engine transients are discussed in Chapter 5.

Miro/Macro Interfacing

This experimental task is indispensable to any microfabricated machine, dealing with the problem of connectivity between microfabricated (silicon) devices and the "macro-world" (i.e. testing apparatus, instrumentation, fittings etc.). Clearly this issue must be resolved in order to test and integrate the micro-rocket engine with a macro-system (i.e. a satellite). An extensive discussion is not provided in this thesis but has been studied as part of a separate research effort [16].

Ethanol Heat Transfer Experiment

An experiment is underway to characterize the heat transfer rates of ethanol subject to the supercritical pressures and high heat flux rates present in the nozzle cooling passages. Lack of data for the conditions of interest have made this experimental effort indispensable. Ethanol provides the majority of the cooling power for the micro-rocket engine, therefore validating the need to accurately predict its cooling performance. Chemical decomposition at high temperatures is also of interest as precipitation of solid carbon could block the cooling passages causing the rocket engine to instantly melt or even disintegrate. An extensive cooling discussion is not provided in this thesis but has been extensively studied as part of a separate research effort [17].

CHAPTER 2

PUMPING SYSTEM CHARACTERISTICS

2.1 Introduction

High performance requirements are imposed on the pumping system in order to ensure the overall feasibility of the micro-rocket concept (a pressure rise of 300 atm or a corresponding rotor tip speed of 170 ms^{-1}). These high pressures are desired to give a high thrust/weight ratio and are required to enable regenerative cooling of the thrust chamber.

In determining the pumping system baseline design, two design alternatives have been examined. One consists of turbopumps where the fluid enthalpy rise required to drive the turbine is achieved through heat transfer mechanisms occurring in the chamber and nozzle cooling jacket.

The other alternative consists of having an electrically driven pump. Such a device would present several advantages such as:

- Inherent self-starting capability (using an auxiliary electrical power source).

- Propellant mass flow throttling capability for variable thrust and increased modularity.

- Decoupling of the pumping power from the thermodynamic processes (involved in cooling the rocket) for increased system robustness.

The latter would allow the test engineer to offset design uncertainties (i.e. microfabrication off-design tolerances and empirical misrepresentations of thermodynamic processes) and

adjust the device's thrust to meet its exact performance specifications.

In this chapter, both design alternatives have been examined against the pumping power requirements for the micro-rocket. While the turbopump concept borrows from established technology, the electrostatic micro-pump is based on current research work [19] and is thus explored in greater detail.

2.2 Electrostatic Micro-Pumps

2.2.1 System Description

The electrostatic micro-pump [†] (see Figure 2-1) architecture consists of a rotor disc and a stator case. The rotor supports the impeller blades and is embedded in the stator case forming the pump housing around its circumference and a motor gap at its base. The power generation unit (or motor) is built of a series of electrodes (distributed circumferentially around the stator motor gap surface) and a conducting sheet located on the rotor bottom surface. The electrodes and conducting sheet are separated by a few microns (~ 1 to 3 μm) and interact through an elaborate excitation scheme [19] to generate torque.

2.2.2 Power Generation

Studies on micro-electrostatic induction machines have been conducted at the MIT Laboratory for Electromagnetic and Electronic Systems (LEES). Simulations modeling the actual physical processes have been developed to characterize motor performance for a fixed set of design parameters. For the present preliminary design considerations, the motor power was approximated, allowing different geometric layouts to be considered, and the simplified expression for the motor power is given by [19]:

$$P_{motor} = \frac{\pi^2 \epsilon_0 EVF(R_0{}^2 - R_i{}^2)}{2(1 + \frac{\epsilon_a G}{\epsilon_0 \Delta})} \tag{2.1}$$

[†]The technical analyses involving the electrostatic motor were performed by S. Nagle. The author has substituted numerical values appropriate for the micro-rocket.
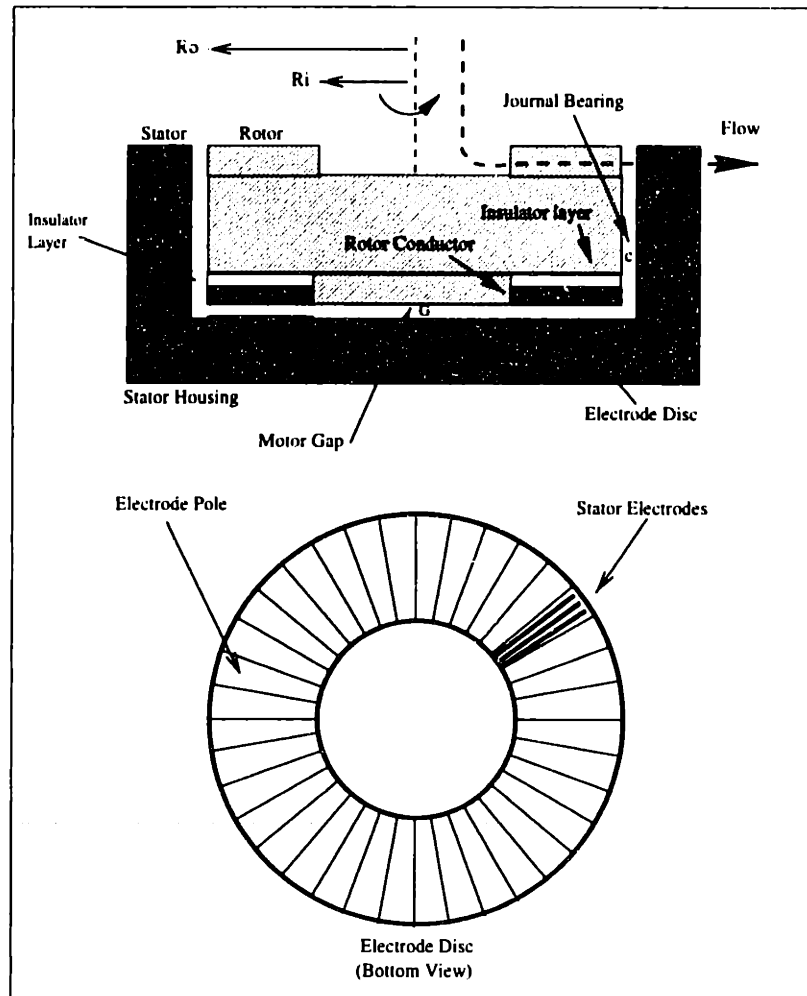
Figure 2-1: Electric Pump Layout.

where V is the voltage potential across a pole, E the electric field acting on the rotor plane, F the pole excitation frequency, Δ the rotor insulator layer thickness, ϵ_0 and ϵ_B the dielectric constants for oxygen and the insulator material respectively, R_o and R_i the motor outer and inner radii, and G the motor gap.

Since $E = \frac{V}{G}$, the electric power is increased by raising V and F while minimizing the gap G for a fixed motor size. However, the following limits exist:

- Voltage is restricted by the electrical field breakdown in the motor gap and across the electrodes (to about 300 Volts).

- Gap size G is limited by microfabrication tolerances to 1 μm, and by viscous shear in the motor gap.

- Excitation Frequency F (associated with the charge relaxation time [19]) is currently limited to 3 MHz.

2.2.3 Signal Resolution

The motor power expression (Equation 2.1) assumes the generation of a sinusoidal traveling wave. It would be achieved by having electrode poles produce amplitude modulated sine waves with a phase shift such that the aggregate electrode disc field would resemble a traveling sine wave. Individual electrodes however, produce square waves which would significantly reduce the real power output of the device to about 40% (see Table 2.1). One way around this involves regrouping several electrodes into a single pole. Each electrode would then produce a phase shifted square wave and using superposition principles would allow for a better sine wave approximation for the individual pole signal. Clearly then, as the number of electrodes per pole increases, signal resolution becomes more refined. Electrode count per pole (or electrode density φ) determines the efficiency of the motor performance as compared to its predicted value obtained from the simplified power equation. It is then necessary to account for the electrode count by means of a calculated relative efficiency term η_r. Current work on the development of a micro-electrostatic motor compressor [6] has provided quantitative data regarding the impact of electrode density on the relative power output of the electric motor. Table 2.1 provides a basis for determining an efficiency for the device. Note that a minimum electrode density of 2 (representing two square waves with a phase difference of 180°) is required to give a first approximation of a sine wave and thus produce power. Clearly then, maximizing the electrode density is desirable if

Electrode Density	η_r
$\varphi = 2$	40%
$\varphi = 3$	65%
$\varphi = 4$	80%
$\varphi = 5$	85%
$\varphi = 6$	90%
$\varphi = 7$	90%

Table 2.1: Impact of Electrode Density on Performance [6].

the electrode size may be chosen arbitrarily. Current microfabrication techniques however

limit the minimum electrode size and the associated spacing per electrode to 4 μm. Taking $Peri = 2\pi\frac{R_o+R_i}{2}$ as the mean perimeter for the motor, the maximum allowable number of electrodes for a specific device is thus:

$$e_{max} = \frac{Peri}{(4+4)(10^{-6})} = \pi\frac{R_o + R_i}{8(10^{-6})} \tag{2.2}$$

Excitation frequency depends on the rate of rotation of the device ω as well as the number of poles M along its perimeter; it may be expressed as follows:

$$F = \frac{1}{2\pi}\omega M \tag{2.3}$$

For very small devices, size sets the limit for the maximum allowable frequency (F_{max}) by constraining the number of poles. Small devices also inherit low signal resolution ($\varphi = 2$) as efficiency must be sacrificed in favor of higher frequencies (thus setting the electrode density to its minimum value of two). On the other hand, as devices become larger, the maximum number of electrodes (e_{max}) no longer restricts frequency. Thus for a given rotational rate, F_{max} can then be achieved with its associated maximum pole count M_{max}. Electrode density may also be increased with pump diameter since e_{max} increases while M_{max} remains constant. Therefore, for equal rotational rates, larger pump sizes benefit from an improved efficiency (η_r).

2.2.4   Modeling of Viscous Losses

Assuming Couette flow (no pressure variation along the circumferential direction of the pump) and taking the fluid velocity to be tangent to the motor surface velocity, fluid shear stress may be written as $\sigma = \frac{\partial U_{wall}}{\partial y} \simeq \mu\frac{U_{wall}}{h}$ where h is the fluid passage height, μ the fluid viscosity and U_{wall} the motor velocity at a given radial station.

Annulus Gap Losses

Shear losses in the pump housing may be expressed as follows:

$$\sigma_a = \mu\frac{\omega R_o}{c} \tag{2.4}$$

and friction power may thus be obtained as:

$$P_a = 2\pi\mu\frac{b}{c}\omega^2 R_o{}^3 \tag{2.5}$$

where b is the motor height and c the journal bearing clearance.

Motor Gap Losses

For a given radial station r, the above expression may be re-derived for a disc section of angular span $d\theta$ and radial span dr. The resulting expression for the motor gap power is then:

$$P_g = \int_{R_o}^{R_i} \omega r^2 \sigma_g dr = 2\pi\mu\frac{\omega^2}{G}\frac{(R_o{}^4 - R_i{}^4)}{4} \tag{2.6}$$

where $\sigma_g = \mu\frac{\omega r}{G}$ and G is the motor gap clearance height.

2.2.5 Pumping Power

For a set wheel speed ω, the electric motor power is given by P_{motor} while the sum $P_a + P_g$ expresses the total viscous losses. The total available power for pumping then becomes $P_{avail} = P_{motor} - P_a - P_g$. The pumping power is related to the mass flow rate, pressure rise and fluid enthalpy rise ΔH according to the following expression [18]:

$$P_{pump} = \dot{m}\Delta H = \dot{m}\frac{\Delta P}{\rho} \tag{2.7}$$

A first order approximation (appropriate for our purpose) of the pressure rise gives [13]:

$$\Delta P = \eta_p\rho(\omega R_o)^2 \tag{2.8}$$

where the pump efficiency η_p accounts for viscous losses within the pump impeller blades. (Note that η_p is different from the electric efficiency η_r associated with the electrode density.)

Having identified the governing equations for the electrostatic pump, the system can now be characterized and a performance map may be established.

2.2.6 Performance Assessment of Micro-Electrostatic Pumps

Design Methodology

In order to determine the applicability of electrostatic pumps to the micro-rocket engine as well as other devices, it is necessary to evaluate its performance against key parameters. As mentioned previously, motor performance is constrained in achieving the maximum allowable frequency as well as an adequate signal resolution and is also subject to competing geometric constraints: for example, while having a larger motor gap G reduces viscous losses (see Equation 2.6), it significantly reduces the motor power as indicated by Equation 2.1.

The design methodology involves maximizing the available pumping power for a desired pressure rise by identifying the optimal pump layout (pole count and electrode density) for each design point. The performance map thus illustrates the available performance envelope for the device where each point on the map represents an electric pump which has been optimized for that specific design target.

Given a pressure requirement and a fixed pump size, the rotational speed of the device may be obtained from Equation 2.8. For this given wheel speed, the motor power is then evaluated, and after estimation of the relevant losses, the available power P_{avail} may be obtained from equations 2.1, 2.5 and 2.6. Cases where $P_{avail} \leq 0$ would indicate that the pressure rise ΔP, chosen initially, may not be achieved for the given motor geometry. For these cases, solutions are omitted as they are unphysical.

The steps involved in maximizing the motor power are presented below. They consist in identifying an optimal layout for the given application:

- Given a pump diameter, evaluate the maximum amount of electrodes for the device using Equation 2.2.

- Using the minimum electrode density ($\varphi = 2$), determine the pole count M corresponding to e_{max} (by definition $M = \frac{e_{max}}{\varphi}$).

- Determine the frequency associated with M using Equation 2.3.

- If $F > 3$ MHz, increase the electrode density such that F takes the maximum allowable value of 3 MHz. Set the frequency to 3 MHz and increase the efficiency η_r accordingly

(see Table 2.1).

- If $F < 3$ MHz, set the frequency to F and maintain the efficiency η_r at 40% (see Table 2.1).

Figure 2-2 shows the different achievable efficiencies for a constant size pump at different rotation rates. While size is held constant, the device layout changes with increasing ω as electrode density is allowed to vary. As ω increases, less poles are required to maintain the maximum excitation frequency of 3 MHz and thus, poles may regroup a larger number of electrodes which inherently enhances the signal resolution.
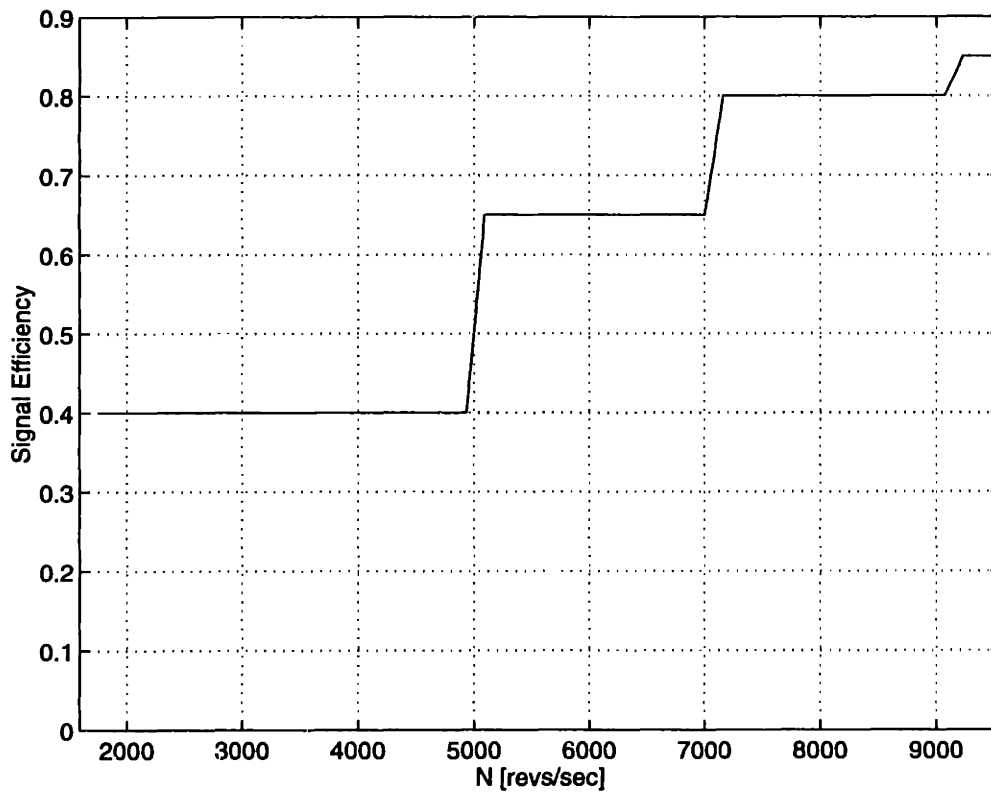
Figure 2-2: Signal Resolution for an Electrostatic Pump.

Figure 2-3 shows the typical power curves for a fixed pump geometry illustrating both the motor gap and annulus gap viscous losses as well as the motor generator power. Note that for this case, the total viscous losses account for more than 50% of the motor power. These large viscous losses occur due to the micro-scale clearances in the motor gap and the journal housing. Motor gap losses have been shown to scale as R^4 as opposed to R^3 for annulus losses. Thus as the device increases in size, motor gap viscous dissipation dominates over

the annulus losses. The motor generator power curve is shown to increase with N while suddenly leveling off to a constant value. This is because motor power varies linearly with frequency and while F is initially restricted by the low rotational rates, it eventually reaches a maximum value (3 MHz) thus establishing a maximum power. As mentioned previously, higher wheel speeds may further increase the available power by allowing higher pump efficiencies (η_r). Figure 2-3 however does not portray this particular phenomenon as it occurs at larger rotational rates than depicted.
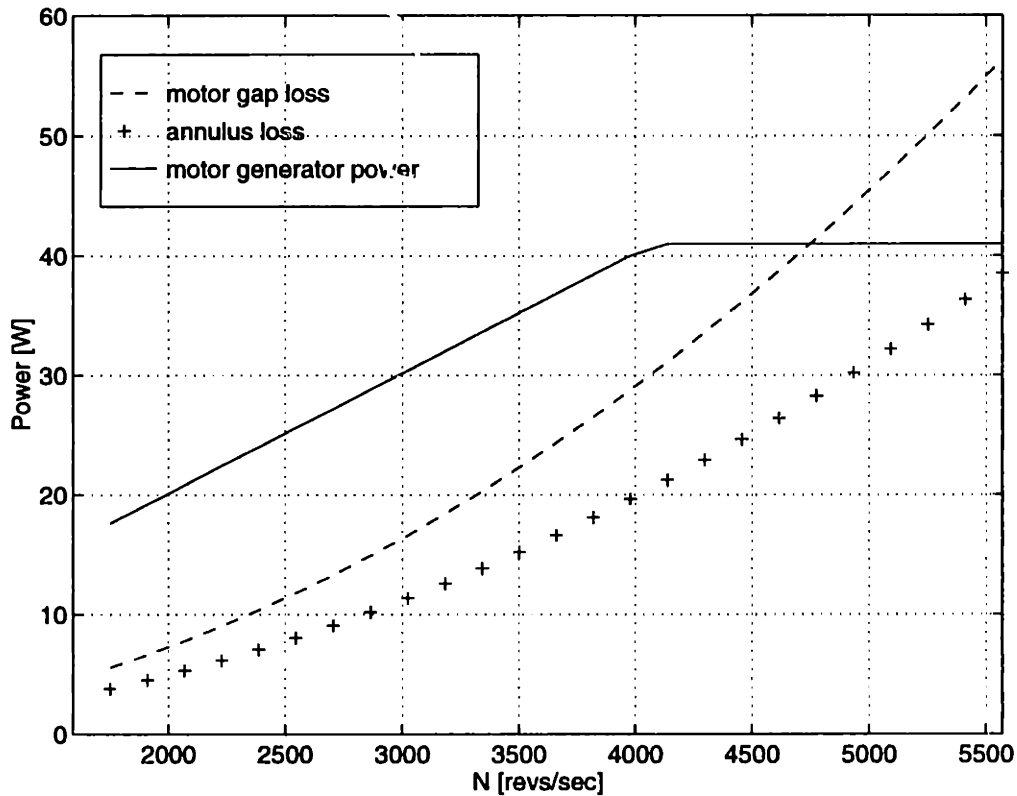
Figure 2-3: Micro-Pump Power Curves (fixed size).

Figure 2-4 shows the net available pumping power corresponding to the power curves in Figure 2-3. Power quickly drops to zero due to the fact that viscous losses increase with N while the motor power levels off to a constant value. The figure also reveals a somewhat narrow margin of operation for micro-electric pumps indicated by the steep negative slope of the power curve. It can then be inferred that maximum wheel speed and thus pressure rise are predominantly determined by size. This fact is better illustrated in Figures 2-5 and 2-6.
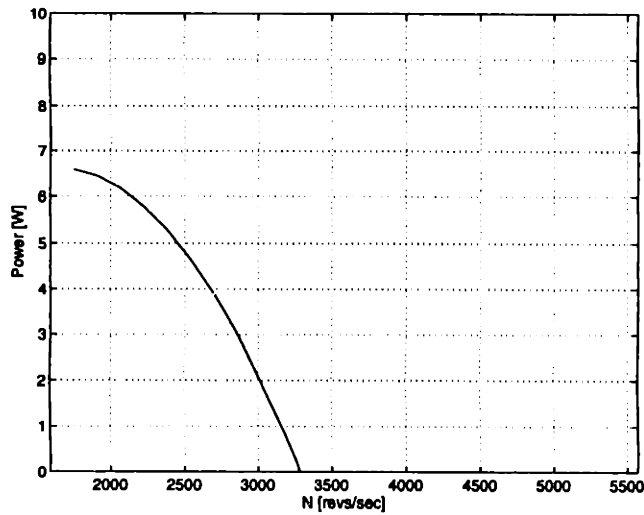
Figure 2-4: Available Pumping Power (corresponding to Figure 2-3).

Performance Map

A performance map has been established for two different motor gap sizes ($G = 1$ μm and $G = 3$ μm). While having a 1 μm gap size clearly improves pump performance (given that motor power scales as $\frac{1}{G}$), feature sizes of 1 μm are however challenging in terms of microfabrication not to mention design offsets associated with the pump disc bending (which may account for a significant percentage of the total gap size). Results for a 3 μm motor gap may then be considered conservative, giving a more reliable performance characterization for the pump.

Figure 2-5 illustrates performance curves relating mass flow rate to pump diameter for different pressure rise values ΔP. Trends indicate that for a 3 μm gap, the maximum achievable pressure rise is about 20 atm, which is an order of magnitude less than that required for the micro-rocket ($\Delta P \simeq 300$ atm). At this pressure however, the maximum mass flow rate is about 2.5 g/sec per pump which agrees with the micro-rocket requirements.

Figure 2-6 shows the same results for a 1 μm gap size. Performance increases as gap size is reduced, producing a maximum pressure rise of 50 atm at the desired mass flow rates.

Note that in both cases ($G = 1$ μm and $G = 3$ μm) the pump sizes needed to develop attractive performances become disconcerting, reaching diameters on the order of the entire rocket unit size (~ 1 cm). Clearly then, micro-electrostatic pumps do not meet the requirements of the micro-rocket pumping system and another alternative must be adopted.

44
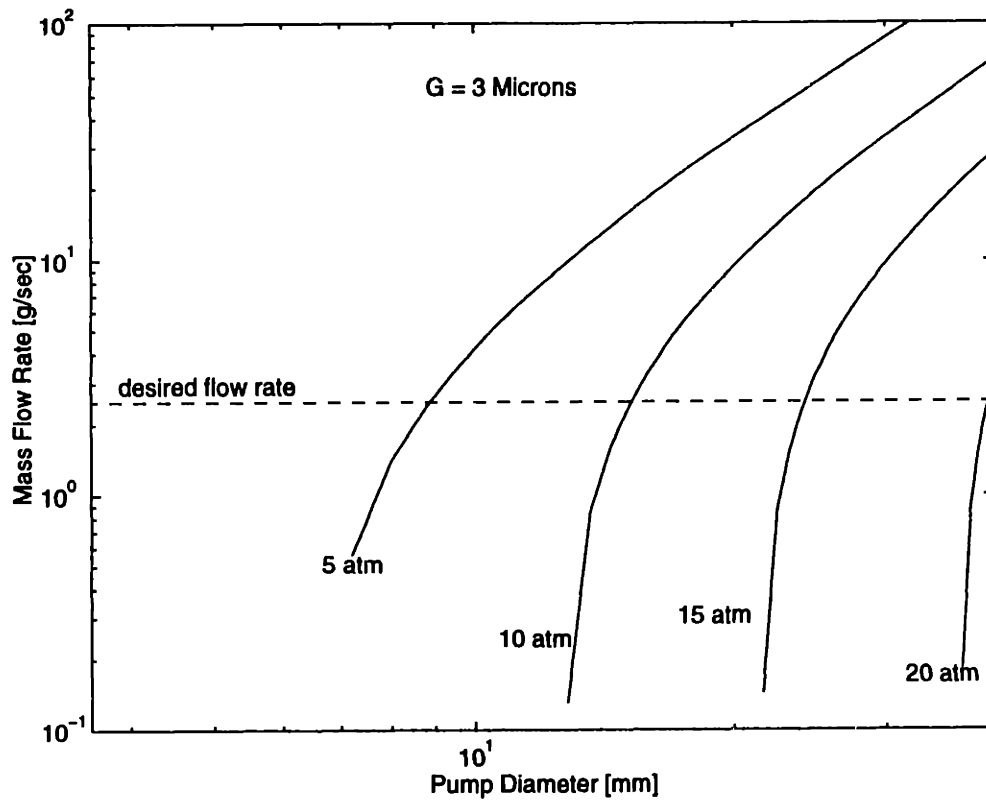
Figure 2-5: Performance Map for a Micro-Electrostatic Pump $(G = 3~\mu m)$.
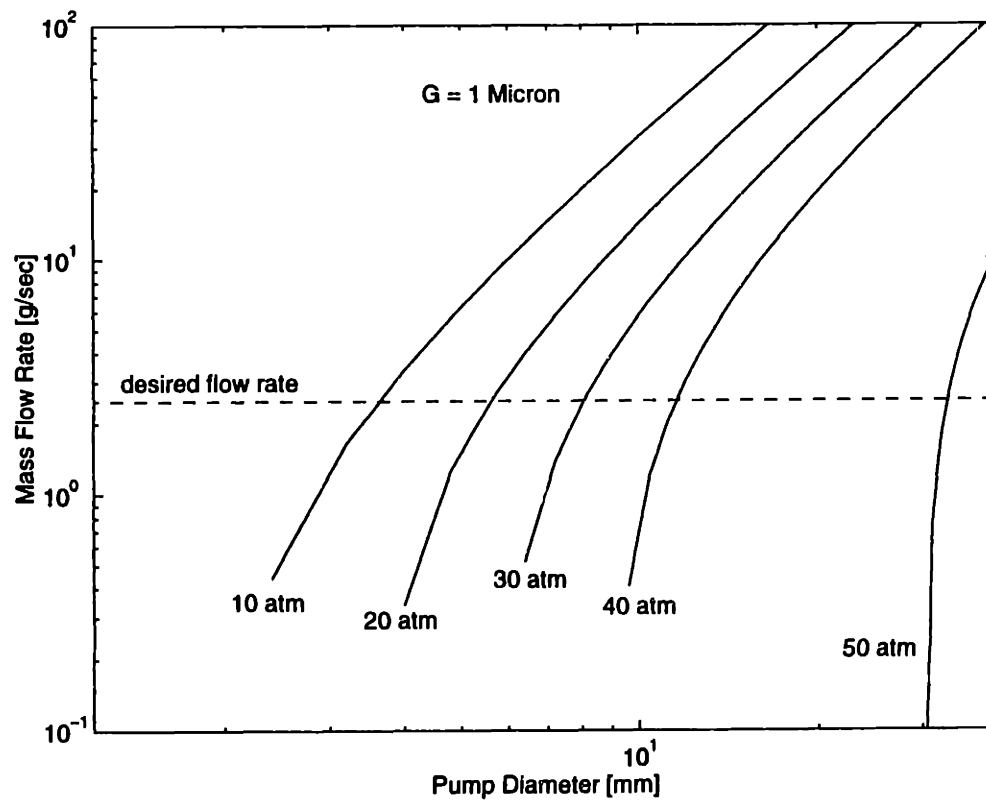
Figure 2-6: Performance Map for a Micro-Electrostatic Pump $(G = 1~\mu m)$.

2.3   Turbopumps

2.3.1   Concept

This section discusses the feasibility of utilizing a turbine driven liquid micro-pump to generate a pressure rise requirement of 300 atm for the micro-rocket engine. At steady state, the pumping power equals the turbine power. Using Equation 2.7 for the pumping power and expressing the turbine power as the fluid enthalpy drop through the rotor blades, then, assuming constant Cp, the power balance can be written as:

$$\dot{m}\frac{\Delta P}{\rho} = \dot{m}Cp\Delta T \tag{2.9}$$

where ΔT is the fluid total temperature drop through the turbine and ρ the fluid density on the pumping side (assumed constant for liquid ethanol and LOX).

Reorganizing Equation 2.9 gives the following expression for ΔT:

$$\Delta T = \frac{\Delta P}{\rho Cp} \tag{2.10}$$

Given that the desired pressure rise is on the order of 300 atm, and assuming $\rho \sim 1000$ and $Cp \sim 1000$, the required temperature drop is thus on the order of:

$$\Delta T \sim \frac{(300)(10^5)}{(1000)(1000)} \simeq 30 \text{ K} \tag{2.11}$$

Assuming an average mass flow rate of 2.5 g/sec for each pump, the required pumping power thus becomes:

$$P_{pump} \simeq \dot{m}Cp\Delta T \simeq 75 \text{ Watts} \tag{2.12}$$

The turbine inlet flow enters at temperatures exceeding 500 K and thus a temperature drop neighboring 30° is conceivable. Power is thus not a constraint for the turbopump as was the case for the electro-static pump and thus the concept seems feasible so far.

2.3.2 Turbine Blade Design

For an Euler turbine [13], the torque is obtained by considering the change in angular momentum between the rotor inlet and outlet sections. It is expressed as:

$$Torque = \dot{m}Cp(r_b v_b - r_c v_c) \tag{2.13}$$

where subscripts b and c represent the rotor inlet and outlet stations respectively (see Figure 2-7), r is the turbine radius and v the blade tangential speed at the given radial station.

From Figure 2-7, the blade angles are related through the following geometric relations:

$$\begin{cases} v_b = u_b \tan(\beta_b) \\ v_c = \omega r_c - u_c \tan(\beta'_c) \\ v_b - \omega r_b = u_b \tan(\beta'_b) \end{cases} \tag{2.14}$$

where β_b is the turbine nozzle vane turning angle, β'_b is the turbine rotor blade incidence angle (or the flow angle relative to the rotor blade), β'_c is the turbine rotor blade turning angle (or the flow exit angle relative to the rotor blade). The radial flow velocity is denoted by u and the tangential flow velocity by v where subscripts b and c refer to the radial stations depicted in Figure 2-7.

Taking r_p as the pump radius, the wheel speed ω is obtained from 2.7 and 2.8:

$$\omega = \frac{1}{r_p}\sqrt{\frac{\Delta P}{\rho \eta_p}} \tag{2.15}$$

The turbine relative flow turning angle can then be computed as:

$$\tan(\beta'_c) = \frac{1}{r_c u_c}(\omega \frac{r_p{}^2}{\eta_p Cp} - r_b u_b \tan \beta_b) \tag{2.16}$$

Calculations of the radial flow velocities u are performed using continuity across the turbine radial stations and thus require the knowledge of the flow density across the turbine. Assuming a fluid inlet total temperature $T_{t,a} = 600$ K, the temperature drop ΔT through the turbine is given from the steady state power balance. The total temperature ratio $\frac{T_{t,c}}{T_{t,b}}$

is then obtained and assuming isentropic flow, the pressure ratio across the turbine can be evaluated as [13]:

$$\frac{P_{t,c}}{P_{t,b}} = \left[\frac{1}{\eta_t} \left(\frac{T_{t,c}}{T_{t,b}} - 1 \right) + 1 \right]^{\frac{\gamma}{(\gamma-1)}} \tag{2.17}$$

where γ is the fluid specific heat ratio and η_t is the turbine efficiency.

The fluid inlet pressure $P_{t,b}$ may be approximated as the pump exit pressure (neglecting pressure drop in the cooling passages). Densities can now be computed at the different radial stations allowing the calculation of the turbine blade angles. Figure 2-7 illustrates the turbine blade angles for a 300 atm pump design. Table 2.3, presented below, illustrates the different blade geometries necessary to sustain pressure rises ranging from 250 atm to 500 atm. Note that the inlet guide vane turning angle has been set at a constant value of 80°. Calculations were performed based on the specifications provided in Table 2.2 and were conducted by taking into account pressure losses across the cooling passages using the model presented in Chapter 5.

Pump Design Parameters	Specification
pump radius (r_p)	0.5 mm
turbine outer radius (r_b)	0.7 mm
turbine inner radius (r_c)	0.35 mm
blade aspect ratio	5
pump efficiency η_p	60%
turbine efficiency η_t	90%

Table 2.2: Pumping System Specifications.

Pressure Rise	β_b	β'_b	β'_c
250 atm	80°	78°	61°
300 atm	80°	82°	75°
400 atm	80°	86°	83°
500 atm	80°	87°	85°

Table 2.3: Turbine Blade Angles for Different Pressure Rise Requirements.
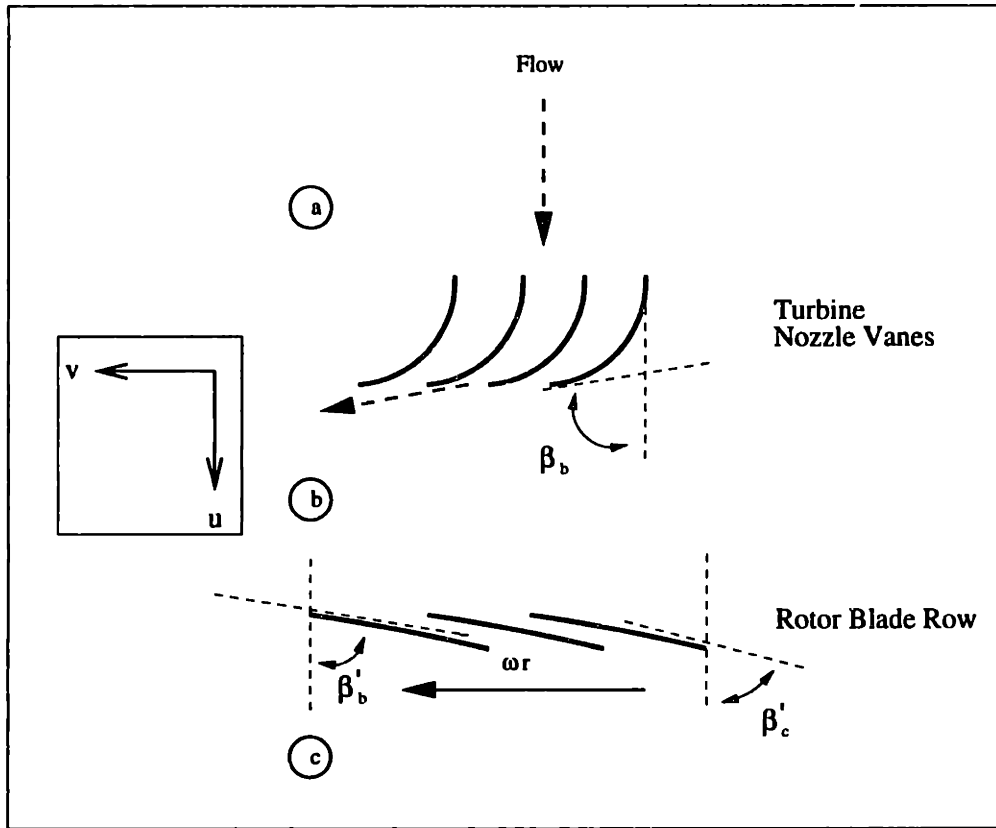
Figure 2-7: Turbine Blade Angles.
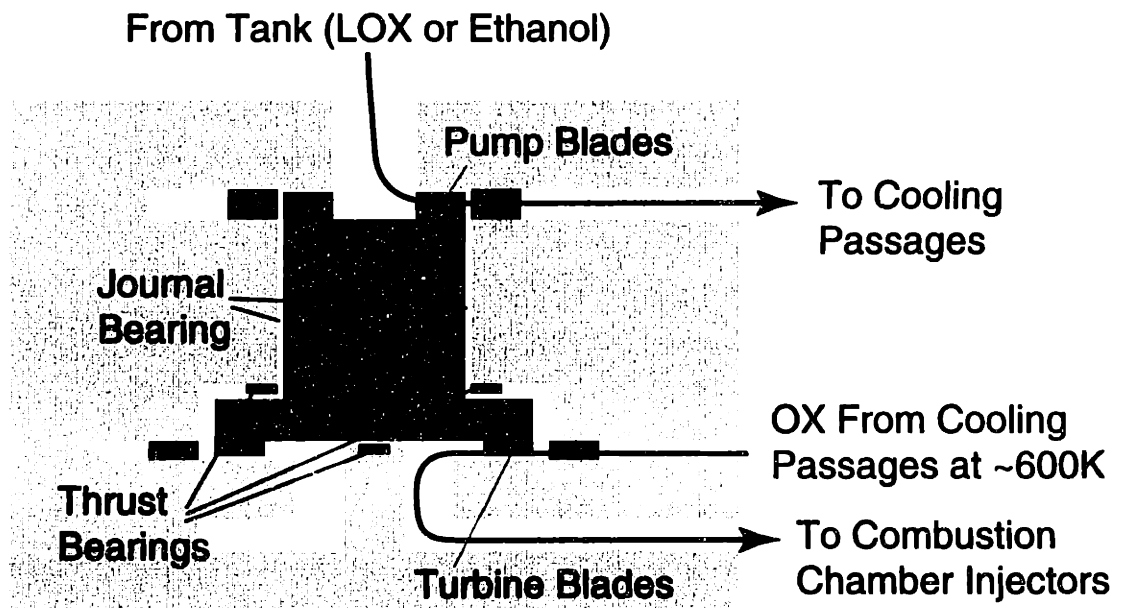
Figure 2-8: Micro-Turbopump Layout [16].

2.3.3 Bearings

While basic fluid dynamics considerations have shown micro-turbopumps capable of delivering the pumping performance required for the micro-rocket engine, proper bearing operation and stability must also be investigated so as to confirm the feasibility of the concept. Two types of bearings are required for this system. First are thrust bearings which are used to counteract the pressure forces on the pumping side of the turbomachinery. Second is a journal bearing arrangement which is able to provide the required lateral forces necessary for stability at the high rotational rates involved (about 1.6 million RPM for a 300 atm pump). Both configurations are illustrated in Figure 2-8.

Hydro-Dynamic Journal Bearing Layout and Definitions

Journal bearings are composed of a cylindrical journal and an annular sleeve. These are shown in Figure 2-8 as the pump unit and the stator case respectively. Clearance c is defined as the difference between the sleeve and journal radii. Journal bearings support loads by generating pressure differences along the annular gap circumference. Unlike ball bearings where reaction force depends on the ball's elastic spring constant and varies linearly with the deflection of the journal, journal bearings react through highly nonlinear fluid pressure differentials generated by a varying fluid film thickness h. The bearing eccentricity e_c represents the minimum film thickness deflection required to support an applied load and the eccentricity ratio ϵ_c is defined as the eccentricity to clearance ratio ($\epsilon_c = \frac{e_c}{c}$).

Design Approach

The governing equations for the journal bearing may not be solved analytically with sufficient generality and thus numerical results (see Reference [8]) have been used as a preliminary design tool. The model however is simplified and does not allow for any "wobbling" motion (motion occurs in a single plane). A recommended operating region [8] for journal bearings of different aspect ratios (λ), relates the eccentricity ratio ϵ_c to a dimensionless

load parameter W_b defined as [8]:

$$W_b = \frac{F_b}{\mu \omega b r (\frac{r}{c})^2} \qquad (2.18)$$

where F_b is the applied load, b the journal height, and μ the fluid lubricant viscosity.

The operating region suggested in Reference [8] may be approximated as a rectangular region with $0.4 \leq \epsilon_c \leq 0.7$ and $0.8 \leq W_b \leq 5.3$. It represents the suggested operating range for a journal bearing of arbitrary aspect ratio. Given the high rotation rates involved and the need to operate in low "g", pump weight does not meet the minimum loading requirement F_b necessary to ensure stability and thus additional asymmetrical pressure forces must be provided. These are generated by redirecting high pressure flow from the volute recuperator region to the journal bearing region thus providing additional loading.

Bearing Performance

Given a pump radius and aspect ratio, asymmetrical side pressure forces may be computed by assuming a value for the area subjected to the higher pressures. This area of exposure was taken to be at a maximum of 10% that of the impeller area (for efficiency considerations) and a minimum of 1% of the impeller area. The load factor W_b may then be calculated for different pump sizes using both the minimum and maximum journal bearing loads, establishing a load factor band as depicted by the crosses ('x') in Figure 2-9. If the load factor band overlaps (at any point) with the suggested operating band for W_b (depicted by the solid lines in Figure 2-9) then there exists a conceivable bearing design which operates in the recommended region. Depending on the locus of the intersection, the required bearing area would range between 1% and 10% of the total impeller area as mentioned before. The calculations have been performed for both an ethanol pump (with viscosity $\mu \sim 10^{-3}$) and a LOX pump ($\mu \sim 10^{-4}$). Figure 2-9a and 2-9b show that for the ethanol pump, the maximum allowable size for a pump with aspect ratio $\lambda = 1$ ($2r = b$) is 0.15 mm while aspect ratios of 2 and above are not recommended. The pump size limit is established by observing the radius where no more overlapping exists between the two bands. Figure 2-9c and 2-9d show that for the case of oxygen, larger pump sizes are feasible (due to the lower viscosity of LOX) with radii ranging from 0.75 mm for $\lambda = 2$ to 1.5 mm for $\lambda = 1$. In

51

summary, results show that pump operation is optimized for sizes of order 1 mm or less.

Stability Considerations

While the above is a recommendation for best bearing performance, the use of pump sizes outside the specified range may not be inconceivable and requires further investigating. In order to confirm that the above recommendations are stable, the pumps have been checked against a stability boundary provided in Reference [7]. This stability check is however only valid for short width bearings ($\lambda \leq .5$), but may nevertheless be used to verify the suggested performance results. A non dimensional mass parameter Ma is defined as [7]:

$$Ma = \frac{c(m_a)\omega^2}{F_b} \tag{2.19}$$

where m_a is the pump mass.

It is shown (see Reference [7]) that the journal bearing is inherently stable for $Ma \leq 5$. Figure 2-10 is a graph of Ma vs. pump radius using a thrust bearing load surface representing 10% of the impeller area. Clearly, $Ma \leq 1$ for the entire radius span thus confirming the previous results. Moreover, Ma may conceivably be increased by a factor of 5 or more indicating that the side loading necessary to achieve stability (for the recommended pump sizes) can in turn be decreased by a factor of 5 (see Equation 2.19). Thus, for stability purposes a journal bearing would only require an area of about 2% that of the impeller area to be exposed to the high pressure flow. Note that larger pump radii are also shown to be feasible but have not been suggested as they did not figure in the recommended design space.

In conclusion, while a formal bearing analysis is necessary for the detailed design phase of the project, micro-turbopumps have been shown to be a feasible and promising concept for the micro-rocket engine.
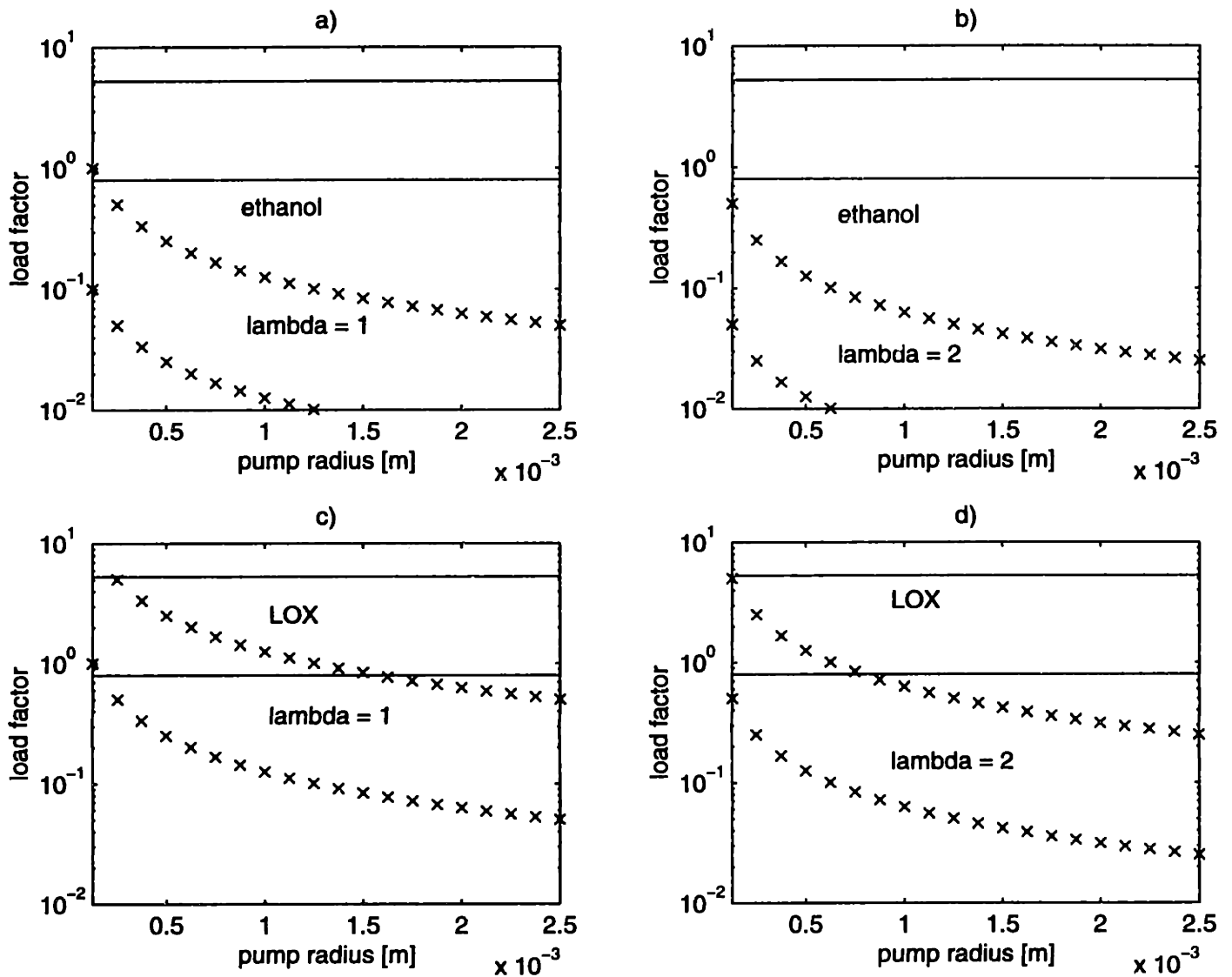
Figure 2-9: Recommended Pump Sizes for Micro-Turbopumps

The figure identifies several pump sizes which agree with the recommended pump operating conditions [8]. A band region indicated by the area comprised between the crosses ('x') represents the non dimensional load factor W_b associated with the minimum and maximum side loading forces available for the bearing. The region indicated by the area comprised between the solid lines indicates the recommended load factor range [8]. A pump is feasible whenever the two bands overlap.
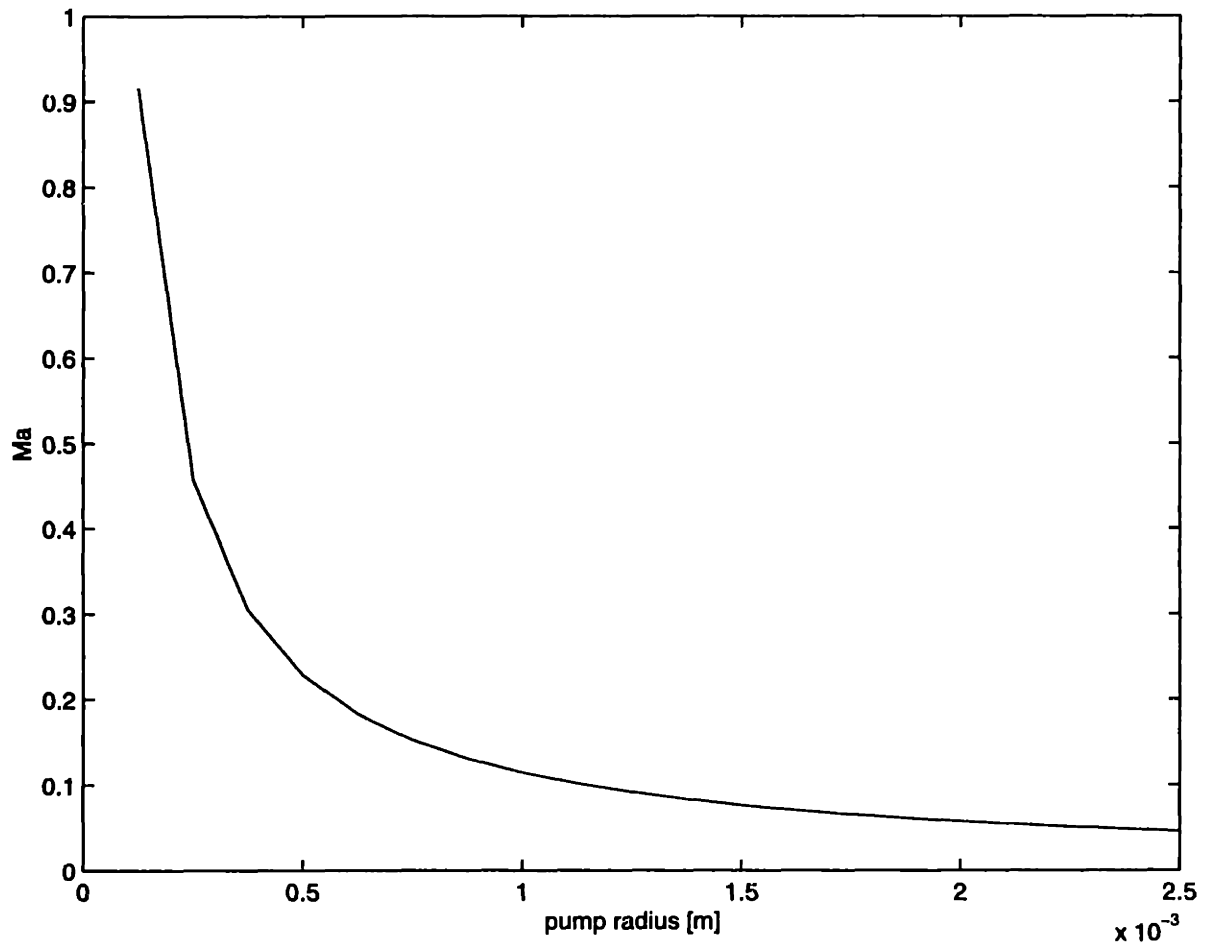
Figure 2-10: Stability Boundary for Short Width Bearings, adapted from Reference [7].

2.4 Conclusion

In this chapter, both the micro-electric and micro-turbopump concepts have been considered. Given current technology, micro-electric pumps have been shown capable of producing a 10 atm pressure rise with a mass flow rate of approximately 2.5 g/sec. Nevertheless, performance falls short of the required pumping power by an order of magnitude. Moreover, the motor sizes necessary to achieve these pressures are on the order of the overall size of the micro-rocket module (about 1 cm). Furthermore, rocket applications would require using several of these devices in series to produce the necessary pressure rise thus further increasing the module size. While micro-electric pumps are clearly not adequate for the micro-rocket engine, they may nonetheless present an attractive solution for micro-electronic circuitry cooling applications, fuel injection as well as other systems involving lower pressures.

Micro-turbopumps, on the other hand, deliver the required pumping power at the millimeter scales, allowing complete integration with the existing thrusting chip without compromising the overall micro-rocket chip size. Bearing performance and stability appear promising for the pump sizes of interest though further analyses need to be pursued in order to better evaluate and validate the pumping system performance.

CHAPTER 3

COMBUSTION CHAMBER DESIGN

3.1 Introduction

Fundamental issues concerning chamber design have been examined, including injection, mixing and combustion. Several injection schemes have been evaluated for the micro-rocket engine, and an attempt has been made to characterize the mixing processes involved. Moreover, thermochemical calculations were conducted in order to determine the chamber temperature and provide some insight on the overall combustion feasibility in micro-combustio chambers.

3.2 Injection and Mixing

Injection and mixing processes are determinant factors for the overall performance and reliability of rocket engines. Anderson et al [1] suggest that oscillations involving jet spray shedding may represent key mechanisms of combustion instabilities. The design objective thus involves establishing an injection scheme which not only allows for complete mixing of the propellants but also prevents significant fluctuations in the mixture quality. Such irregularities could translate into pressure fluctuations in the chamber which may eventually lead to combustion instabilities.

3.2.1 Injector Design

A great deal of literature has been devoted to the characterization of different injector designs and their implications on stability. Research papers (see Reference [1]) featuring analytical, computational and experimental models indicate that mixing performance (entailing both mixture quality and stability) is highly sensitive to injector geometry and operating parameters. Thus, lack of empirical data regarding micro-size injectors and supercritical jets indicate that propellant mixing for the micro-rocket engine presents a challenge which cannot be completely solved until actual test validations are performed.

Intermediate and high frequency (> 400 Hz [24]) combustion instabilities are linked with combustion processes and are therefore difficult to trace due to the injection and mixing uncertainties mentioned previously. Low frequency (10 − 400 Hz [24]) instabilities, on the other hand, are linked with pressure interactions between the combustion chamber and the propellant feed system. Pressure fluctuations inside the chamber propagate upstream and affect the propellant pumps, altering the mass flow rate of the system. This ultimately feeds back into the chamber where growing pressure oscillations may arise, possibly causing violent instabilities. The latter may, however, be avoided by utilizing choked injectors, thus preventing chamber pressure fluctuations from propagating upstream and altering the turbine exit pressure. Conventional rocket engines don't feature choked injectors due to the significant pressure drop ratio required across the injector plates (a factor of about 2). This, however, comes at the expense of costly experiments necessary to verify the reliability and stability of the propulsion system. The micro-rocket engine, on the other hand, will incorporate choked injectors during its preliminary testing stage in order to minimize the source of failures and increase system robustness. Pressure drops across the injectors may then be compensated for by increasing the propellant feed pressure.

Design Constraints

By restricting manufacturing to two dimensional features (see Chapter 1), current micro-fabrication technology imposes several constraints on injector design. In the case where injection occurs along the wafer plane, the injector hole cross section is then restricted to a rectangular profile. Figure 3-1 shows three common injection practices including doublets,

shower heads and coaxial injectors [24]. All have been extensively studied for circular cross sections and exhibit strong performance sensitivities to geometric variations [1]. Mixing characterization for square channel jets thus becomes a difficult task since typical empirical correlations only apply to a specific injector layout.
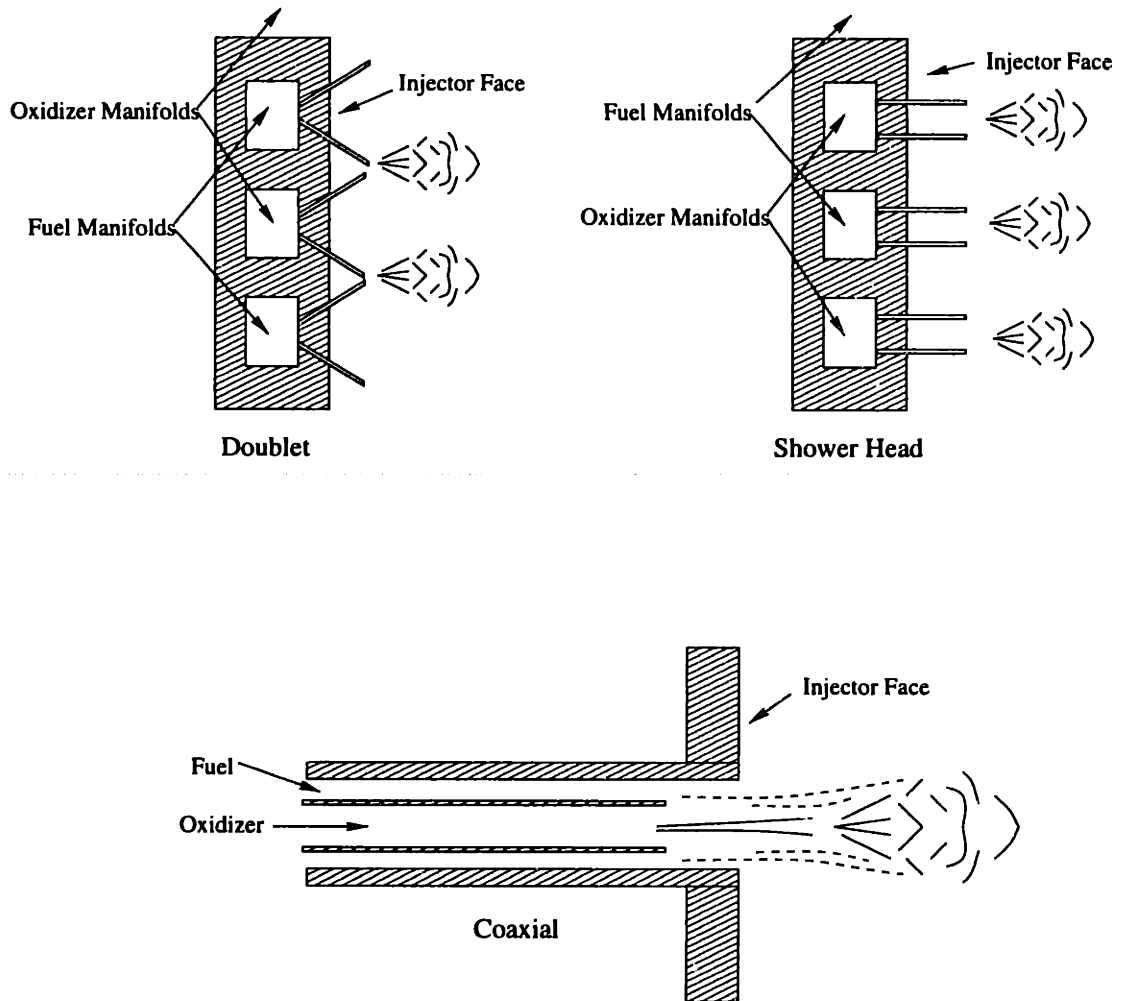
Figure 3-1: Schematic of Conventional Injection Practices, adapted from [24].

Injection may either take place along the nozzle flow direction using rectangular channels or across the chamber walls (normal to the nozzle flow direction) where circular holes may be fabricated. The goal is to adopt the mixing strategy which best suits the particular requirements of the micro-rocket engine. Jet velocities have been chosen to be sonic and thus considering the combustion chamber scale ($\sim$ 1 cm), any misalignment in the impingement

region may lead to unmixed propellant flow being injected far downstream of the chamber or even the nozzle. This could ultimately incur performance losses or even severe combustion instabilities, thus eliminating the first injection scheme as an attractive alternative and reinforcing the need to inject across the chamber walls (i.e. from top to bottom).

Proposed Layout

The proposed injector design for the micro-rocket engine is illustrated below in Figure 3-2. It consists of inter-digitated ethanol and oxygen injector holes, occupying both top and bottom surfaces of the chamber mixing region and impinging on each other at a 180° angle. The purpose of this layout is to maximize mixing within a fraction of the chamber length. This particular configuration is thought to enhance mixing by providing diffusion opportunities not only at the impingement plane (chamber mid-height) but also along the jet streamlines as parallel oxygen and ethanol flows start to coalesce. Moreover, such a layout would also prevent high momentum jets from escaping the chamber as they would immediately collide, "splashing" against the chamber opposing wall.
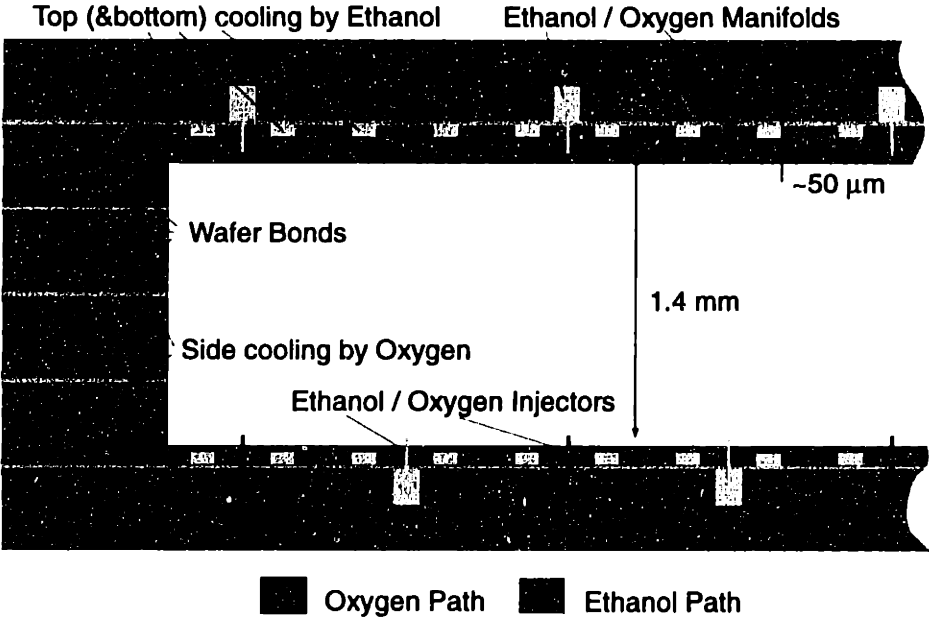
Figure 3-2: Schematic of the Proposed Inter-Digitated Injector Layout [16].

3.2.2 Mixing

One method used to evaluate whether the chamber is sufficiently large to allow for complete mixing of the propellants, is the calculation of the chamber characteristic length L^* [24] which is compared to common accepted values for conventional rocket engines. L^* represents the length of a straight tube of cross sectional area A_t (nozzle throat area) with a volume equivalent to that of the chamber. For the micro-rocket engine, the nozzle throat width is approximately 500 μm (see Chapter 4), the chamber height 1.4 mm and the chamber length (or width) of order 1 cm. The chamber characteristic length thus becomes:

$$L^* = \frac{V_{ch}}{A_t} \simeq \frac{1\ cm\ \text{X}\ 1\ cm\ \text{X}\ 1.4\ mm}{500\ \mu m\ \text{X}\ 1.4\ mm} = 0.20\ \text{m} \tag{3.1}$$

where V_{ch} is the chamber volume.

Typical values for L^* involving bipropellant rocket engines range from 0.8 to about 3.0 meters [24]. This suggests that the chamber volume would have to be increased by a factor of 10 to meet conservative industry guidelines. Such an increase in capacity would effectively translate into an increase in chamber area as depth is quasi-limited by the micro-fabrication etching processes, resulting in a bulky, "not so micro" rocket chip. While L^* represents a useful design benchmark, failure to meet it does not necessarily indicate poor mixing. The characteristic chamber length considers typical injection schemes and thus may conceivably be shortened with an enhanced mixing scenario.

In order to gain more confidence in the proposed mixing scheme, empirical correlations [23] have been used to determine whether the cross flow jets have enough momentum to penetrate the chamber half-height and whether their spreading is sufficient to mix with adjacent injector sprays. Consider 2 injector plates (top and bottom) featuring five rows of 20 injectors each for a total of 200 injectors. Assuming a chamber width of about 1 cm and a chamber height of 1.4 mm, the spacing per injector thus becomes on the order of 500 μm. For an injector discharge coefficient of 0.6 [24], the diameter required to accommodate a propellant mass flow of 5 g/sec at sonic conditions is approximately 20 μm. The required penetration height is then 0.7 mm ($= \frac{1.4}{2}$ mm) while the necessary spreading distance is approximately 500 μm (representing the length of 25 injector diameters).

For the case of transverse gas injection in a gaseous stream, correlations [23] relate the jet penetration height h with the jet arc direction ξ. The latter are non dimensionalized by the injector diameter d_{inj} and the ratio of the jet velocity U_j to the free stream velocity U_∞. Correlations results [23] are summarized below:

$$\frac{h}{d_{inj}(U_j/U_\infty)} = \begin{cases} \frac{\xi}{d_{inj}(U_j/U_\infty)} & \text{for } \frac{\xi}{d_{inj}(U_j/U_\infty)} \leq 2.0 \\[3ex] 1.63\sqrt[3]{\frac{\xi}{d_{inj}(U_j/U_\infty)}} & \text{for } \frac{\xi}{d_{inj}(U_j/U_\infty)} > 2.0 \end{cases} \tag{3.2}$$

The free stream velocity can be evaluated from continuity at approximately 0.3 m/sec while the jet velocity $U_j \simeq 450$ m/sec. Assuming an arc length equal to half the chamber height ($\xi = 0.7$ mm), the resulting non-dimensional arc length then becomes:

$$\frac{\xi}{d_{inj}(U_j/U_\infty)} \simeq 0.2 < 2.0 \tag{3.3}$$

The jet penetration height is then obtained from Equation 3.2 as $h = \xi = 0.7$ mm. This would then infer that the jet reaches the impingement plane (located midway along the chamber height) along a quasi-straight path with little or no curvature in its trajectory.

A similar correlation [23] may be used for jet spreading, relating the spreading distance of the stream to the axial distance traveled by the jet. Penetration results have hinted that axial jet velocities (or the axial distances traveled) are negligible until impingement thus inferring that the spreading may not prove sufficient ($< 500\mu m$) for the jet to properly mix along the injection flow stream direction. Conceivably, injectors could also be regrouped in denser clusters so as to verify the spreading requirement proposed above. Nonetheless, much uncertainty still resides on this subject and thus complete validation would only be established during an actual firing test.

3.3 Combustion

Combustion analyses and simulations are essential in order to characterize the thermo-chemical processes occurring in the combustion chamber. First, the combustion temperature and its relation to the propellant mixture must be determined in order to develop

62

an appropriate cooling strategy for the thrusting nozzle. Second, it is also important to evaluate the residence time necessary for the fluid mixture to achieve combustion equilibrium. The chemical kinetics occurring in the chamber depend on both pressure and the chemical composition of the mixture and are independent of scale. Therefore, by reducing the chamber size, the effective residence time seen by the fluid inside the chamber decreases while the required combustion time remains constant. This becomes an issue at very small scales where the chamber size cannot be reduced without incurring performance losses due to incomplete combustion or even flame-out. Third, in order to compute the rocket nozzle performance, the major species constituting the combustion products must be identified so as to accurately evaluate the fluid properties at stake.

3.3.1 Combustion Model

The combustion region is modeled separately from the injection and mixing regions as a perfectly stirred reactor (PSR) which assumes the entering flow to be perfectly mixed (mixing has occurred at the molecular level). The model therefore only considers the combustion chemical kinetics and thus ignores any further mixing processes occurring in the combustion region. This assumption is reasonable assuming the fuel and oxidizer have properly mixed in the injection and mixing regions, but provides a lower bound on the combustion time.

Figure 3-3 illustrates a schematic of the combustion control volume. Superscript i denotes inlet flow conditions while subscript k denotes the chemical species index.

Two different computational methods were used in this section. They are both part of the Chemkin software package (see References [20], [21] & [25]):

- PSR [20]: Uses reaction mechanisms to determine the combustion equilibrium for different flow residence times by solving the species and energy conservation equations (see Appendix A). Over 90 chemical reactions (see Appendix B) involving ethanol and oxygen have been used in order to characterize the processes involved (see References [27] & [26]). This software is primarily used for reactions where the residence time is smaller than that needed to achieve complete combustion.

- TCC [25]: The Thermo-Chemical Calculator solves the equilibrium problem by min-

imizing the Gibbs' free energy for individual species (it doesn't require any reaction mechanism). This software is strictly used for combustion equilibrium calculations.
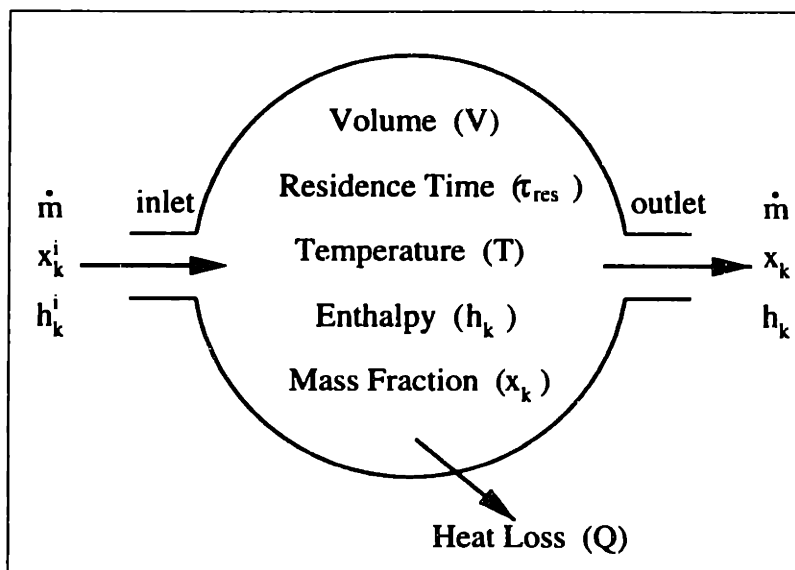
Figure 3-3: Schematic of the Combustion Control Volume, adapted from [20].

PSR calculations are very sensitive at or near stoichiometric conditions and thus it was necessary to calibrate the results with codes designed specifically for equilibrium calculations (i.e. TCC). On the other hand, TCC does not feature a heat loss mechanism and thus thermochemical calculations were performed using two different fluid inlet temperatures (300 K and 600 K) to obtain a bound for the chamber temperature. Fluid mixtures with an inlet temperature of 600 K give an upper bound for the rocket chamber temperature, accounting for the increased propellant enthalpy acquired in the regenerative cooling processes but discarding the associated chamber heat loss. PSR calculations on the other hand were performed in accordance with the actual micro-rocket mechanisms: a fluid inlet temperature of 500 K and a heat loss Q. Given that the heat flux from the hot combustion gases must equal the chamber heat loss into the propellants (or cooling flow), Q can be evaluated as $Q = Ah\Delta T$. Here, A denotes the heat exposure area, h the heat transfer coefficient inside the chamber and ΔT the temperature difference between the combustion temperature and the chamber walls. Given a design combustion temperature of 3000 K, a uniform wall temperature of 1000 K, and given that $h \simeq 10^4$ (see Chapter 5), then for a

chamber of size of 1 cm X 0.5 cm X 1.4 mm (width X length X depth): $Q \simeq 2000$ Watts.

3.3.2 Simulation Results

Chamber Temperature

Chemical equilibrium calculations were performed for different O/F (oxidizer to fuel) mass ratios. Results were obtained using both TCC and PSR software packages. Figure 3-4 shows that for non stoichiometric mixtures, PSR temperatures fall within the TCC temperature range, indicating that kinetic simulations can accurately portray equilibrium conditions. PSR data points are also shown to closely follow the TCC 300 K inlet temperature line. The effects of the regenerative cooling processes can thus be effectively approximated by considering the fluid to enter the chamber at room temperature. The design O/F ratio ensuring a combustion temperature of 3000 K was found to be O/F = 1.15 where a 5% error in O/F would cause temperature fluctuations of ± 100 K in the combustion chamber.
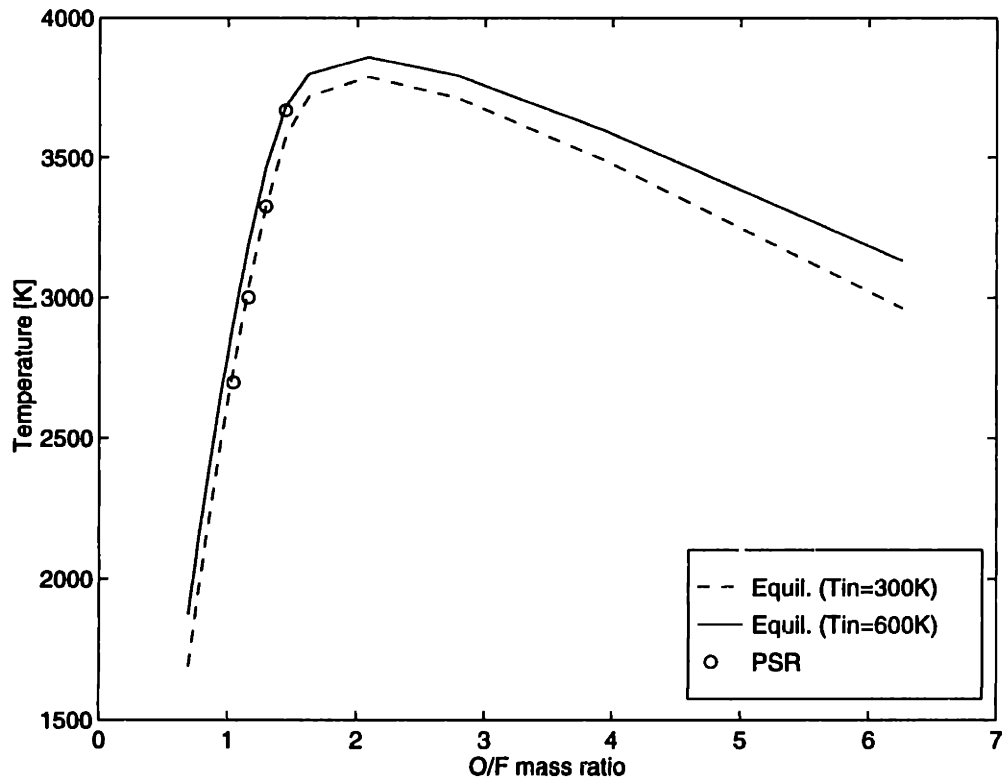
Figure 3-4: Combustion Chamber Equilibrium Temperatures for Different O/F Ratios.

Combustion Products

Assuming a design O/F ratio of 1.15, the chemical composition for the reaction products was obtained. Figure 3-5 shows the molar fractions for the reaction products major species: H_2O, CO, CO_2, H_2 and H. For each species, three concentration values are provided according to the different computational methods used (TCC (300K), TCC (600K) and PSR). This was essentially done to check for any discrepancies between the codes and also to determine how heat loss in the chamber affects the products of combustion. As illustrated below, chemical compositions vary by less than 20% (except for the Hydrogen atom population which appears to be very sensitive to the reaction processes and initial conditions).
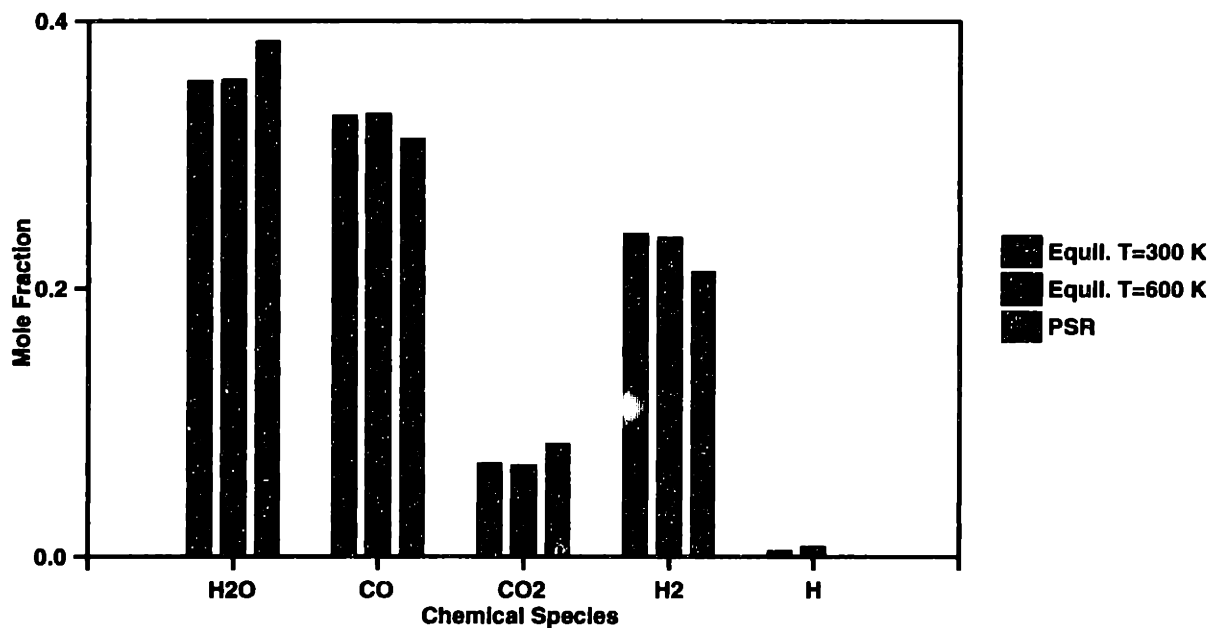
Figure 3-5: Chemical Composition of the Reaction Products.

Further calculations involving the chemical composition of the combustion products (i.e. nozzle CFD) will be based on the values provided by the PSR software due to its ability to model the chamber heat loss.

Flame Blow-Out Limit

The minimum residence time was evaluated for an O/F ratio of 1.15 by simulating the reaction chemical kinetics under different flow times spent inside the chamber. Minimum residence time was then determined as the time below which combustion cannot be sustained (blow-out limit). Figure 3-6 illustrates combustion temperature curves for different chamber residence times. This was done for the case of an adiabatic chamber and a chamber with heat loss $Q = 2000$ Watts. Whereas chamber temperatures are nearly constant for large residence times ($\tau_{res} > 10^{-5}$ sec), they start dropping dramatically as they approach their blow-out time limit. The minimum residence time for the case of an adiabatic chamber was found to be 3×10^{-7} sec. while that for the chamber with heat loss was found to be twice as large (7×10^{-7} sec.).
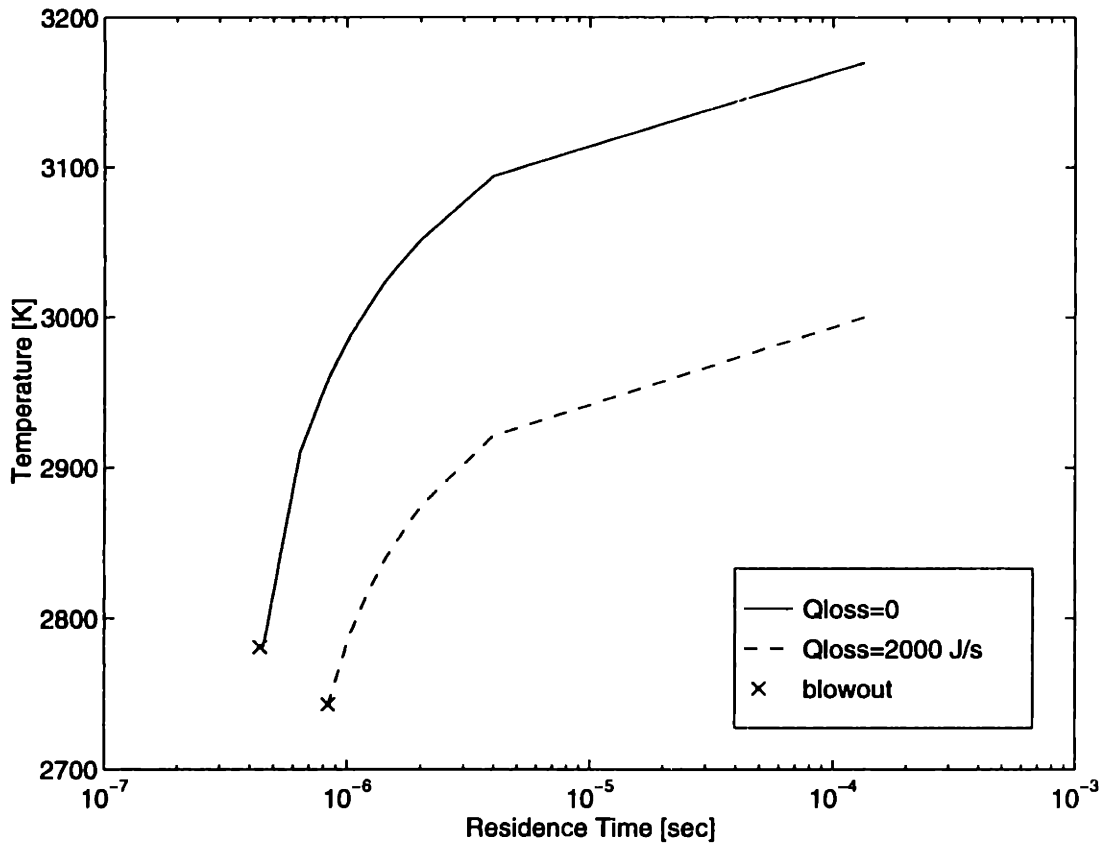
Figure 3-6: Chemical Kinetics Residence Time.

3.4 Discussion

Given a chamber flow density $\rho \simeq 500\ kg/m^3$ and mass flow rate $\dot{m} = 5\ g/s$, the actual residence time for a proposed chamber layout of width 1 cm, length 0.5 cm and depth 1.4 mm is:

$$\tau_{res} = \frac{\rho V}{\dot{m}} \simeq 0.05 \text{ sec.} \tag{3.4}$$

Clearly then, the chamber allows sufficient residence time for the chemical reactions, and the combustion characteristic time is then ultimately set by the mixing time. While chemical kinetics calculations indicate that shrinking the chamber volume by several orders of magnitude is feasible, mixing requirements may render even the current proposed layout a significant challenge.

CHAPTER 4

NOZZLE DESIGN AND ANALYSIS

4.1 Introduction

The micro-rocket nozzle is three orders of magnitude smaller than conventional rocket engines and thus aerodynamic analyses were required to investigate the performance penalties associated with the viscous losses. Several nozzle profiles were assessed in an effort to characterize performance tradeoffs and obtain a baseline design for the micro-rocket engine. Moreover, temperature contours inside the nozzle were used to estimate the local heat flux distribution to the nozzle walls in an effort to develop an appropriate cooling scheme for the engine (ensuring quasi-uniform wall temperatures across the nozzle length).

4.2 Design Parameters

4.2.1 Nozzle Profile

In adopting a nozzle profile, several geometries have been evaluated and examined for performance losses induced by either viscous losses or flow separation. The design goal was set at minimizing the nozzle length without significantly affecting the thrust of the device.

The contour was established in two parts:

- An arc section tracing an angle α and extending from the throat to the nozzle point of inflexion.

- A parabolic fit starting at the inflexion point and extending to the nozzle exit plane (matching the slope at the point of inflexion).

Geometry is then specified by the throat width d_t, the nozzle area expansion ratio $\epsilon = A_e/A_t$, and the aspect ratio $K \equiv L/d_e$ (see Figure 4-1). The radius of curvature for the arc portion of the nozzle was chosen to be twice the nozzle height ($R = 2d_t$). This method proved very effective in establishing efficient nozzle configurations while allowing for quick alterations during the design iteration cycle (for a fixed nozzle width and expansion ratio, only K and α need to be changed in order to generate a new contour).
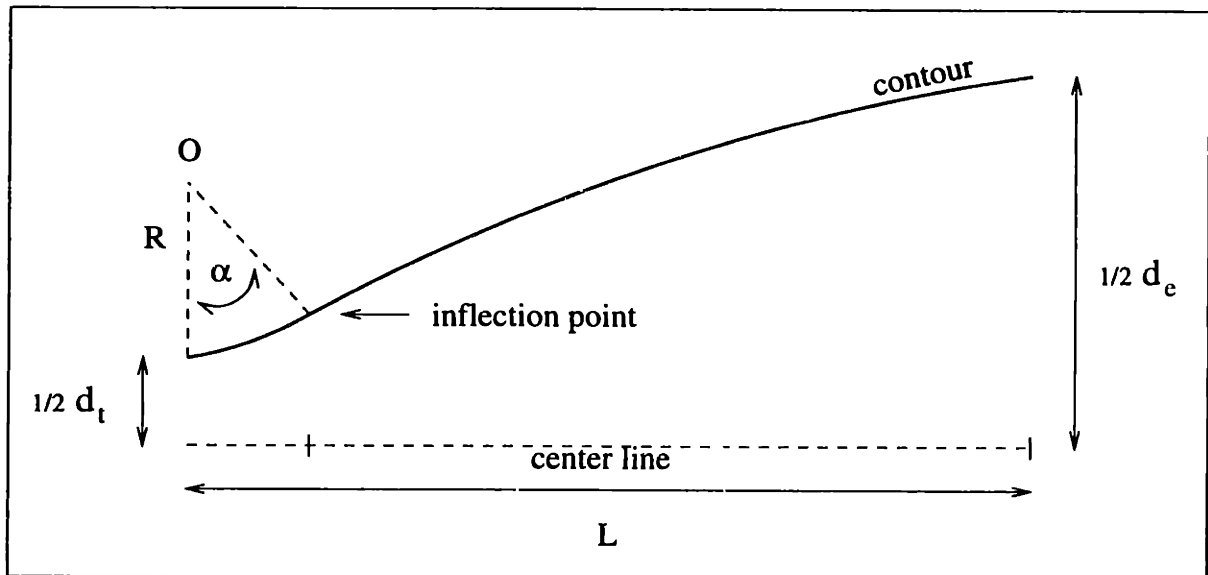
Figure 4-1: Nozzle Contour Design.

4.2.2 Sizing

The design chamber pressure was selected at 125 atm in order to ensure adequate thrust performance while keeping the turbomachinery blade tip speeds well under their critical stress regime. For a supersonic nozzle, the area expansion ratio ϵ may be related to the

nozzle exit and chamber pressure ratio according to the following 1D relation [24]:

$$\frac{1}{\epsilon} = \left(\frac{\gamma+1}{2}\right)^{\frac{1}{\gamma-1}} \left(\frac{P_e}{P_{ch}}\right)^{\frac{1}{\gamma}} \sqrt{\frac{\gamma+1}{\gamma-1}\left[1 - \left(\frac{P_e}{P_{ch}}\right)^{\frac{\gamma-1}{\gamma}}\right]} \qquad (4.1)$$

where P_e and P_{ch} represent the nozzle exit pressure and chamber pressure respectively.

Considering that the initial rocket tests will be performed in an atmospheric environment ($P_\infty = 1$ atm), then for $\gamma = 1.25$, Equation 4.1 gives $\epsilon \simeq 12.5$. For design purposes, the area expansion ratio was set at $\epsilon = 12$. In order to calculate the throat width, the following equation relating mass flow to the chamber pressure and throat area was used [24]:

$$\dot{m} = \frac{A_t P_{ch}}{\sqrt{\gamma R_g T_{ch}}} \gamma \sqrt{\left(\frac{2}{\gamma+1}\right)^{\frac{\gamma+1}{\gamma-1}}} \qquad (4.2)$$

The throat width was then evaluated as $d_t = A_t h$ where h is the nozzle depth (or height). Therefore, given that $\dot{m} = 5$ g/sec, $T_{ch} = 3000$ K and $h = 1.4$ mm, then $d_t \simeq 480$ μm. (The gas constant R_g was computed based on the flow chemical composition as shown in Figure 3-5).

4.3 Two Dimensional CFD

The following section discusses the computational tool used to analyze the nozzle flow aerodynamics including the various features utilized by the code. Flow assumptions are presented as well, along with a schematic of the nozzle computational grid and the specified boundary conditions.

4.3.1 Computational Method

Solver

Due to the two-dimensional nozzle layout, a 2D Navier-Stokes and chemistry solver (SPARK [12]) was found adequate to solve the nozzle supersonic flow. This code has been extensively validated in the past for a variety of different supersonic mixing problems (i.e. see Reference

71

[11]) and for the purpose of this project, has been successfully tested to capture shock waves, boundary layer growth and flow separation.

Code capabilities include:

- Viscous supersonic flow.

- Chemical reaction mechanisms.

- Local evaluation of thermodynamic and transport properties.

- Heat loss through the nozzle walls.

- Turbulence model.

Computational Grid and Boundary Conditions

The computational grid is composed of 84 grid points in the flow direction and 42 points in the transverse direction. Grid compression is applied near the nozzle wall to capture the viscous boundary layer. The fluid inlet conditions were set to be sonic ($M = 1$) at the throat with a stagnation pressure and temperature equal to the chamber total pressure and temperature ($P_t = 125$ atm, $T_t = 3000$ K). The nozzle wall boundary was maintained at 1000 K with a no-slip velocity condition. A zero gradient was maintained at the nozzle center line (symmetry plane) as well as the nozzle exit. The nozzle exit is supersonic and thus the fluid exit pressures only depend on downstream pressure information (hence the zero gradient condition). Subsonic flows were found to occur for only one or two grid points (near the wall) and changing the boundary condition for subsonic flow was found not to affect the results while considerably slowing down convergence.

Convergence

Convergence proved difficult to achieve for sharp turning angles at the throat as well as area expansion ratios greater than 5. It was then necessary to guide the solutions through approximately 10 intermediary nozzle layouts in order to obtain convergence for an area expansion ratio of 12 and a nozzle aspect ratio of order 1.
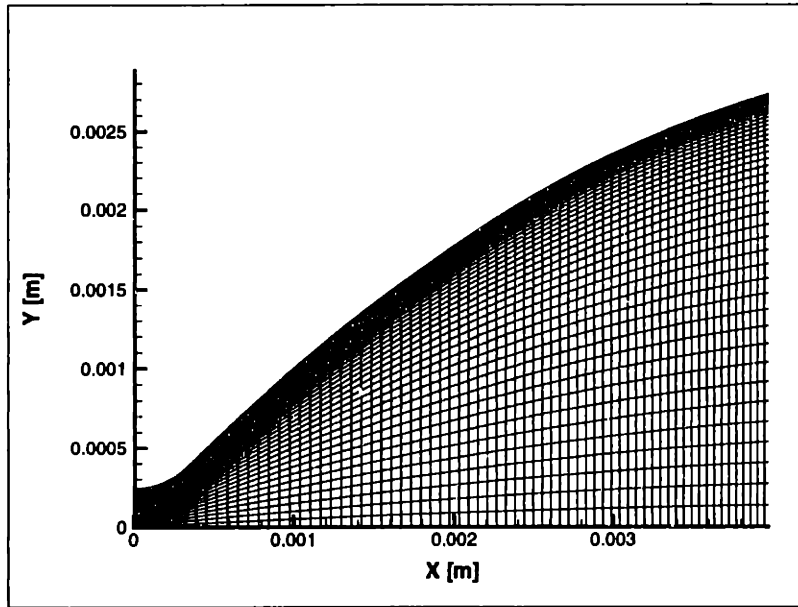
Figure 4-2: Nozzle Computational Grid.

4.3.2 Flow Assumptions

Frozen Flow

Flow calculations through the nozzle were achieved assuming frozen flow (i.e. no reactions occur through the expansion process) and thus no reaction mechanisms were required. This assumption holds reasonably well given that the residence time seen by the fluid inside the nozzle is of the same order as the characteristic chemical reaction time. If the flow velocity is taken to be sonic then using previous results on the minimum chemical residence time τ_{comb} (see Figure 3-6) :

$$\frac{\tau_{noz}}{\tau_{comb}} = \frac{L}{\tau_{comb}\sqrt{\gamma R_g T_{ch}}} \tag{4.3}$$

where L is the nozzle length. Now given that $L \simeq d_e \sim 4\mathrm{x}10^{-3}$ m, and $\tau_{comb} \simeq 10^{-6}$ sec. then:

$$\frac{\tau_{noz}}{\tau_{comb}} \sim 2 \tag{4.4}$$

The frozen flow assumption is thus validated or errors due to it should be small.

73

Inlet Fluid Composition

The ability to customize the fluid inlet chemical composition was taken advantage of, allowing an accurate representation of key thermodynamic [4] and transport [28] properties such as heat capacity, enthalpy and viscosity. Species molar fractions were obtained form the chemical equilibrium calculations provided in Chapter 3 (see Figure 3-5). They are tabulated below:

Chemical Species	Molar Fraction
H_2O	0.365
CO	0.312
H_2	0.231
CO_2	0.075

Table 4.1: Nozzle Flow Chemical Composition.

4.4 Performance Evaluation

Nozzle performance was evaluated by calculating the thrust and comparing it to the ideal thrust value assuming no losses. Since CFD calculations are two-dimensional, thrust calculations were estimated by multiplying the thrust per unit length by the nozzle height. Thrust calculations based on 2D CFD results thus only account for viscous losses along the nozzle side walls, neglecting losses induced by the top and bottom walls. While this overestimates thrust, it nevertheless allows to establish performance tradeoffs across different nozzle geometries.

CFD Thrust Calculation

Assuming an ambient pressure P_∞ of 1 atm, the thrust T of the device may be computed by calculating the momentum balance for the rocket engine control volume:

$$T = \int_{A_e} [\rho u^2 + (P - P_\infty)]dA_e \qquad (4.5)$$

where A_e is the nozzle exit area and u is the x-component of the exit flow velocity.

Ideal Thrust Calculation

The ideal thrust may be calculated using the ideal thrust equation [24] as follows:

$$T_{ideal} = A_t P_{ch} \sqrt{\frac{2\gamma^2}{\gamma - 1} \left(\frac{2}{\gamma + 1}\right)^{\frac{\gamma+1}{\gamma-1}} \left[1 - \left(\frac{P_e}{P_{ch}}\right)^{\frac{\gamma-1}{\gamma}}\right]} + (P_e - P_\infty)A_e \qquad (4.6)$$

In calculating T_{ideal}, γ was taken as its average value obtained from CFD results ($\gamma = 1.25$).

Loss Estimation

Losses can be estimated by computing the thrust difference between the actual nozzle and an equivalent ideal nozzle. The total computed losses would then reflect the viscous losses as well as the losses incurred by the nozzle geometry such as flow separation, shocks and insufficient flow turning at the nozzle exit (thrust is generated by the axial flow momentum and thus proper turning is crucial to the performance of the thruster). The following relation was used to estimate thrust performance losses ΔT_{loss}:

$$\Delta T_{loss} = \frac{T_{ideal} - T_{real}}{T_{ideal}} \qquad (4.7)$$

4.5 Results

The results are presented in two sections:

- In the first section, several nozzle geometries are evaluated and compared for performance. This section allows the selection of a baseline design for the nozzle.
- The second section adopts the baseline geometry, illustrating the flow characteristics including Mach, pressure and temperature contours as well as velocity vector fields and a characterization of the heat flux to the nozzle walls.

4.5.1 Performance Tradeoffs

Aspect Ratio, K	Turning Angle, $\alpha°$	Calculated Thrust, T [N]	Ideal Thrust, T_{ideal} [N]	ΔT_{loss} (%)
0.8	45	13.47	13.76	2
0.7	52	13.09	13.76	5
0.6	55	12.76	13.76	7
0.5	62	12.33	13.76	10
0.4	68	11.97	13.76	13

Table 4.2: Performance Tradeoffs for Different Nozzle Geometries.
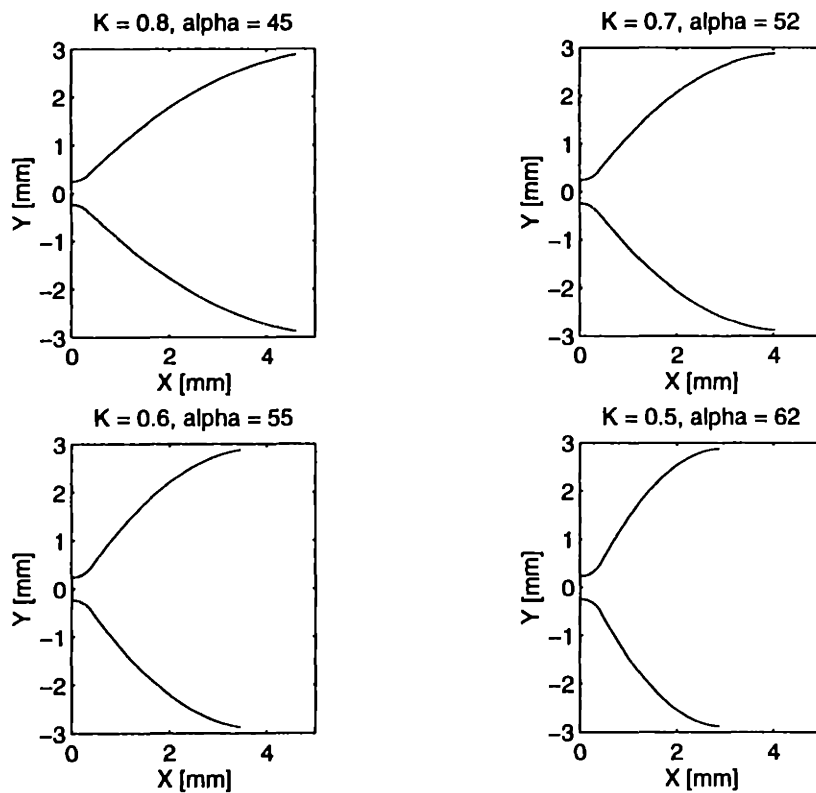
Figure 4-3: Nozzle Geometries for K=0.8 to 0.5.

4.5.2 Nozzle Baseline Design (K=0.8) Flow Characteristics
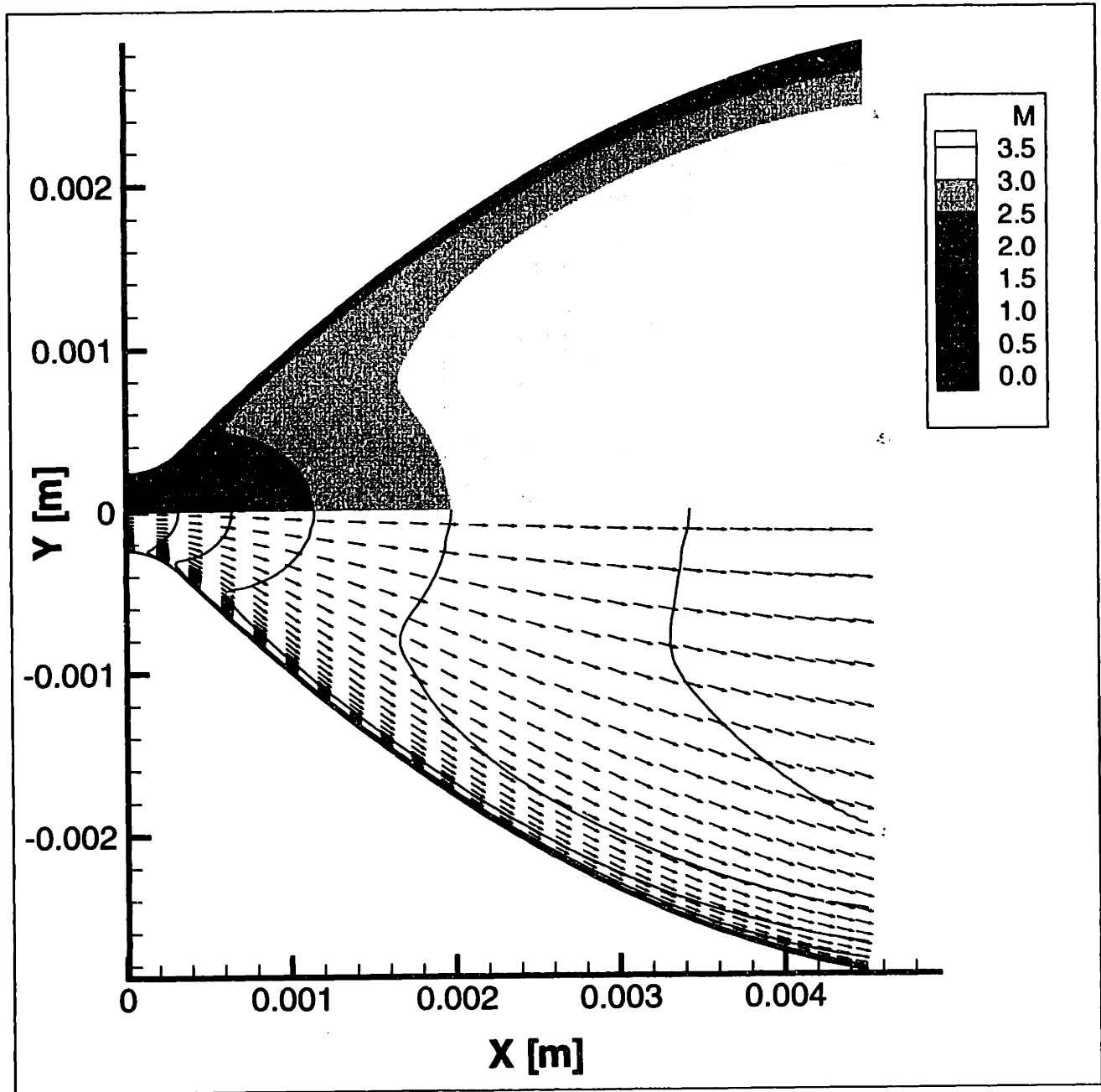
Figure 4-4: Mach Contours and Velocity Vector Fields.
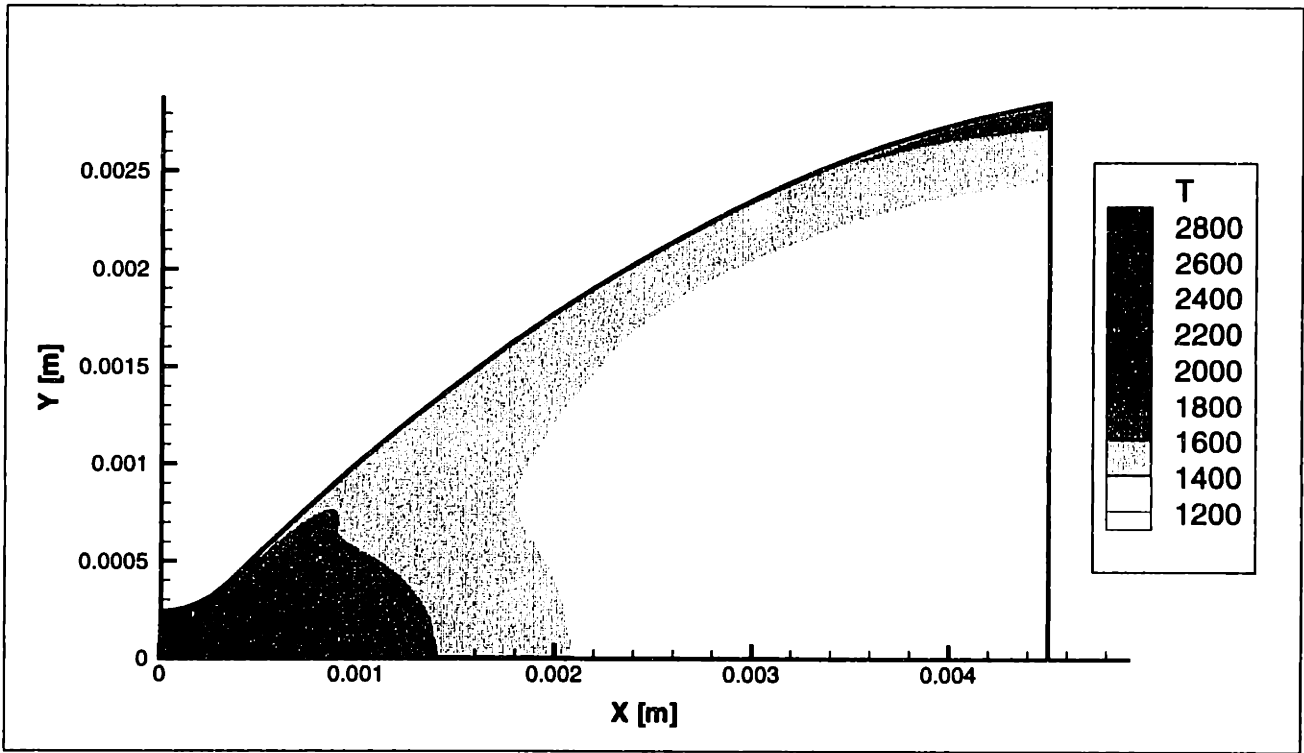
Figure 4-5: Nozzle Temperature Contours.
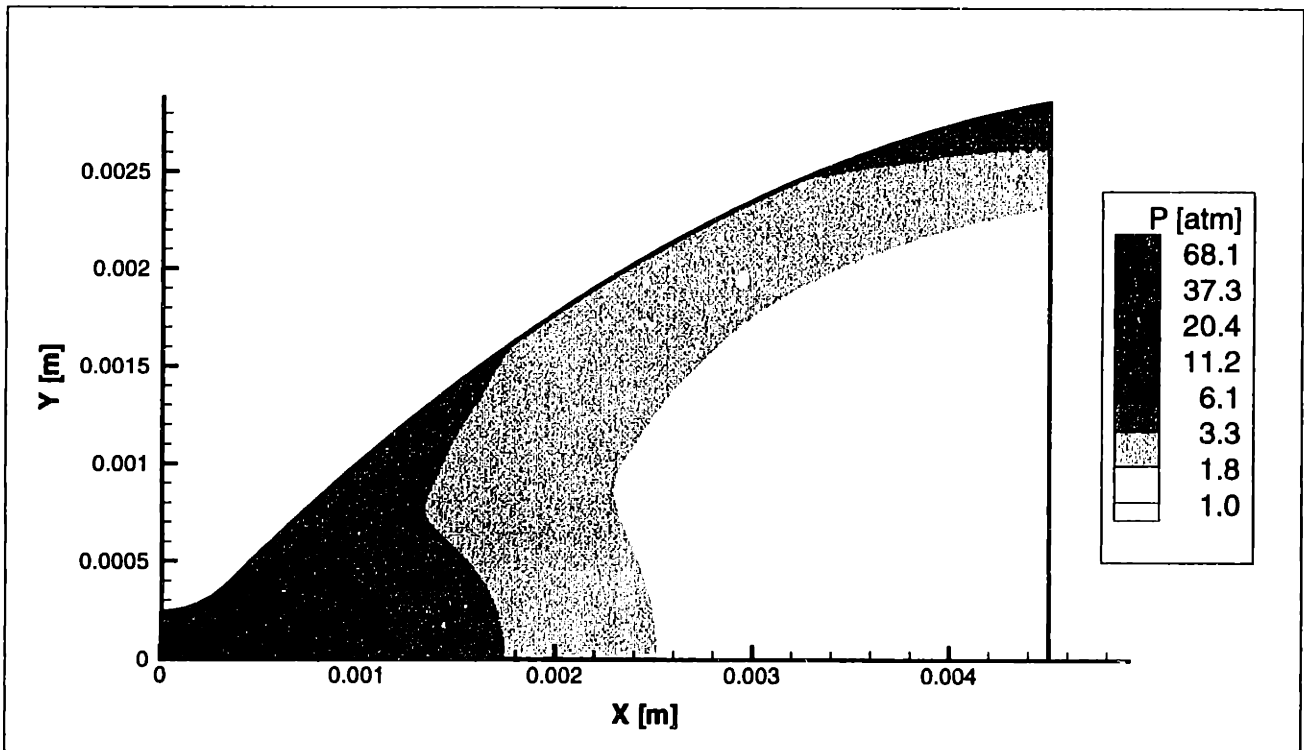
Figure 4-6: Nozzle Pressure Contours.
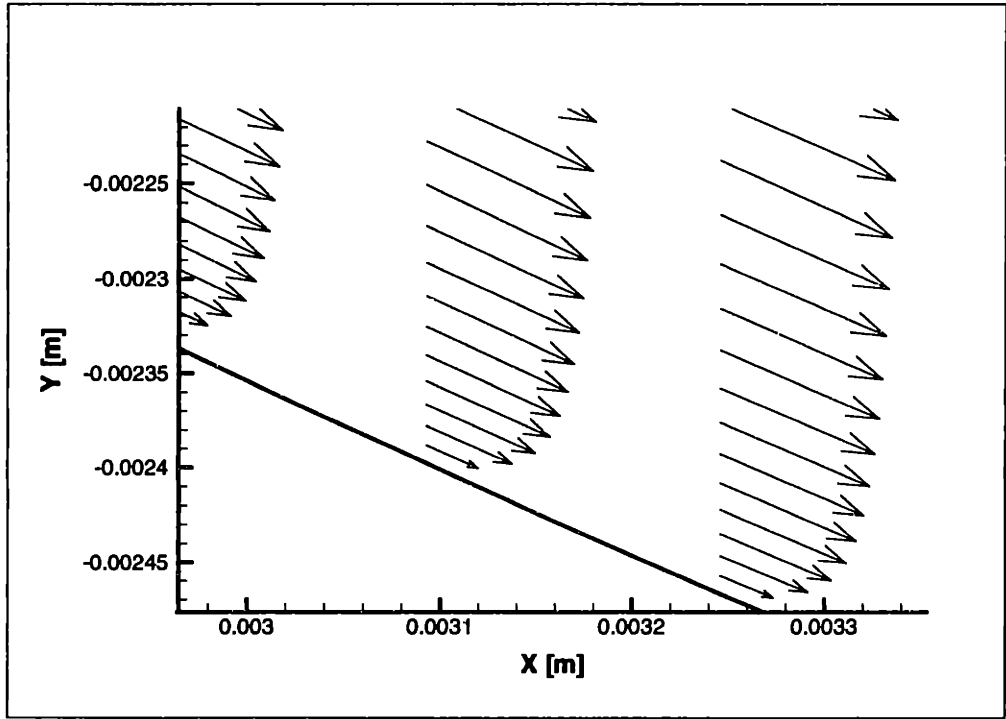
Figure 4-7: Nozzle Boundary Layer View.
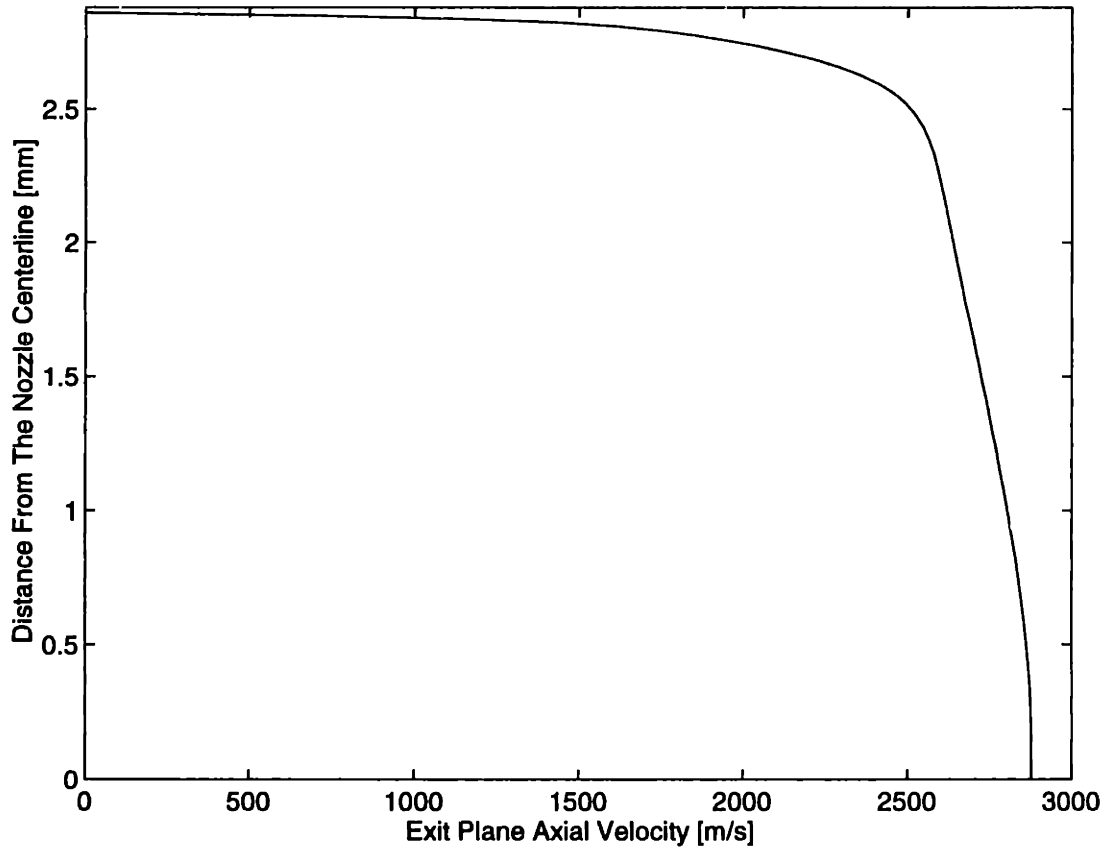
Figure 4-8: Nozzle Axial Velocity Profile (Exit Flow).
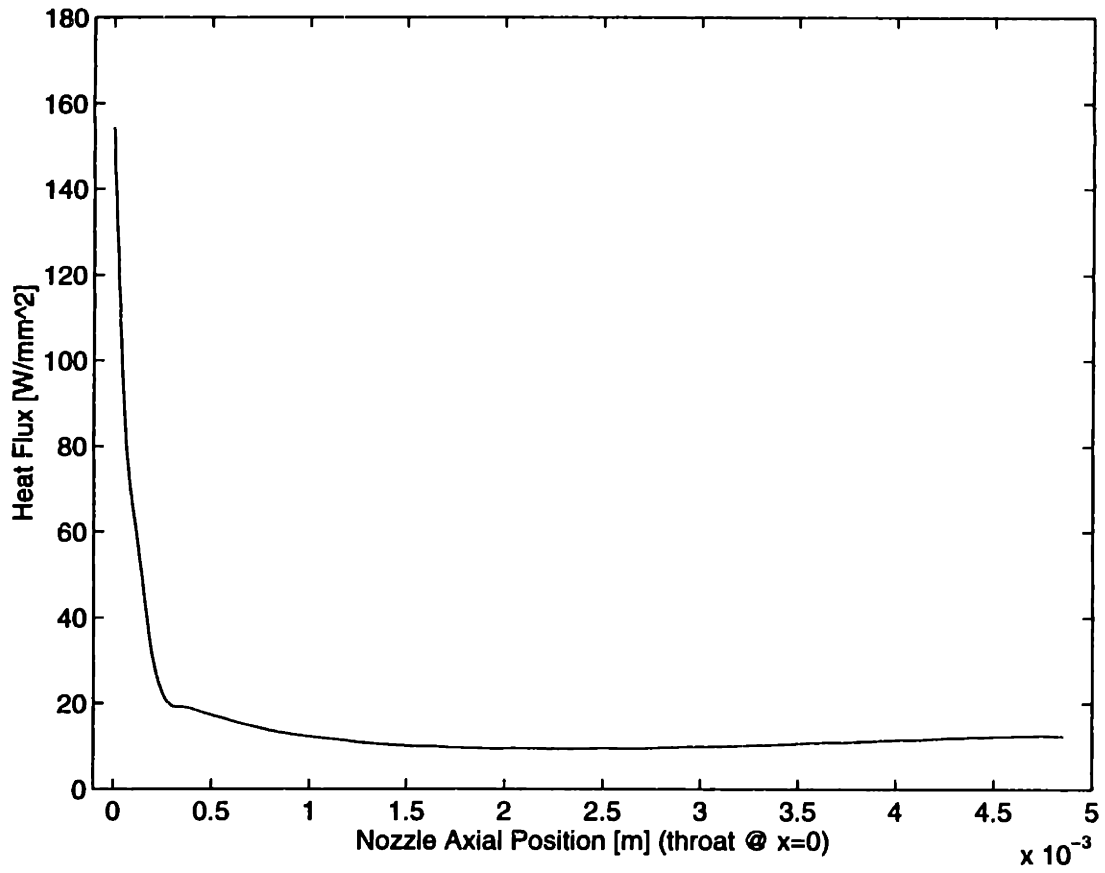
Figure 4-9: Heat Flux to the Nozzle Walls.

4.5.3 Discussion

CFD flow analyses and performance calculations have led to a significant reduction in the nozzle length. Adequate nozzle performance was achieved for aspect ratios as low as 0.4. Table 4.2 provides a list of the different thrust performances associated with nozzle aspect ratios ranging from 0.8 to 0.4 and Figure 4-3 illustrates their various geometries. Performance calculations have indicated total losses of approximately 2% for the case of a nozzle with an aspect ratio of 0.8. Nozzles with smaller aspect ratios exhibit greater losses, up to 13% for $K = 0.4$. Thrust losses for these geometries are mainly attributed to the nozzle's inability to turn the flow adequately in the axial direction, especially for streamlines away from the nozzle centerline. Flow separation only occurred for the shortest nozzle length ($K = 0.4$) at Mach numbers larger than 2.5. Longer nozzles ($K > 0.8$) were shown to behave quite similarly to the $K = 0.8$ nozzle, showing little improvement in performance.

The baseline design length was thus fixed at $K = 0.8$ (and $\alpha = 45°$). The total thrust was calculated to be 13.5 N for a mass flow of 5.0 g/sec with an associated specific impulse (I_{sp}) of 275 sec. Figure 4-4 illustrates the flow characteristics for that specific design, showing both Mach contours and velocity vector fields. Figure 4-8 shows the axial flow velocity profile at the nozzle exit. For $K = 0.8$ it appears fairly uniform up to the wall boundary layer where velocity quickly drops to zero (as expected by the no-silp condition). Figure 4-6 and 4-5 illustrate the associated pressure and temperature contours. Figure 4-9 provides a plot of the heat flux ($\ddot{q}$) to the nozzle wall. It is calculated assuming a linear temperature profile near the boundary layer using the following approximation: $\ddot{q} = k(T)\frac{(T_{j=2})-(T_{j=1})}{\Delta Y_j}$ where $k(T)$ is the thermal conductivity of the fluid calculated at the fluid temperature T. (As mentioned previously, this information will prove very useful in developing a successful cooling scheme). Note that the maximum heat flux ($\simeq 200 \ W/mm^2$) occurs at the throat, and is about one order of magnitude greater than that usually encountered in conventional rocket engines.

Supersonic flow has been shown to be feasible for nozzle scales in the millimeter range without incurring any significant losses in performance ($\Delta T_{loss} < 5\%$). Viscous loses appeared to be quite negligible at the millimeter scales involved. Figure 4-7 illustrates the boundary

layer showing a film thickness of about 0.1 mm, which represents about $\frac{1}{60}$th of the total nozzle exit width.

While this chapter focuses on the 2D flow characteristics of the nozzle, 3D aerodynamics are believed to behave quite similarly given the two-dimensional nature of the nozzle geometry. 3D viscous effects are expected to alter performance by reducing the effective nozzle exit area accordingly (3D CFD would be required to justify this assumption). The nozzle side walls have been shown to have a boundary layer thickness of approximately 0.1 mm with a zero momentum thickness of about 0.03 mm. Thus assuming the same losses for the top and bottom walls, the effective exit area for the 3D case is reduced to:

$$A_{eff} = (480 \ \mu m(12) - 0.06 \ mm)(1.4 \ mm - 0.06 \ mm) = 7.72 \ mm^2 \qquad (4.8)$$

and thus the total area blockage becomes: $\frac{A_{eff}}{A_e} \simeq 0.96$. 3D viscous losses may thus incur an additional performance loss of 2% (over the 2D losses) for a total loss of about 4% $(= 1.00 - 0.96)$ (3D CFD is required to validate the 3D performance loss estimation). This then indicates that the nozzle design is satisfactory and that 3D viscous losses are not significant for the baseline nozzle design $(K = 0.84)$.

_i_

Chapter 5

Micro-Rocket Start-Up Dynamics

5.1 Introduction

Modeling of the micro-rocket start-up dynamics is essential in examining the feasibility of the device as a system as well as determining its characteristic response time. The system can be characterized as a regenerative oxidizer expander cycle where a fraction of the heat released inside the chamber is absorbed by the oxidizer in the cooling passages and used to drive the turbines and the propellant pumps. Before ignition has occurred, the chamber walls are at room temperature and the question arises to whether there is enough latent heat capacity in the silicon structure to provide sufficient power to start-up the pumping system. In actuality, the device only requires sufficient energy to accelerate the pumps to the point where they will generate enough pressure for combustion to occur. Simulations can therefore help predict if the device is self-starting as well as provide insight on alternate design implications in the case it is not (i.e. influence of feed tank pressure, silicon case volume and initial temperature or even the need for an auxiliary electrical heat source). Secondly, simulation of transients can help uncover the overall characteristic time of the device as well as determine individual component time constants and their repercussions on the system. Identifying the rocket response time also provides insight on the different

possible applications for the device such as an eventual thrust pulsing capability.

Finally, depending on the plumbing ahead of the pump impeller, sufficient latent heat energy might be stored in the LOX delivery channels to immediately vaporize the oxidizer before it even reaches the pump. This would then cause the pump to initially act as a gas compressor and prevent the system from performing properly. Further investigations would thus be required in order to characterize the system performance in the case where gas ingestion occurs.

5.2 Modeling

5.2.1 System Layout

The system being considered is composed of an oxygen feed tank, a pump connected to a turbine via a shaft (pump and turbine rotation rates are equal), a heat exchanger representative of the heat transfer occurring between the chamber and nozzle cooling passages, an injector plate, as well as a combustion chamber and a thrust nozzle (see Figure 5-1). The micro-rocket only uses oxygen as the working fluid to drive the turbopumps. Because of its low boiling temperature, LOX can easily be vaporized in the cooling passages at room temperature conditions thus allowing the rocket self-starting capability. Heat transfer processes involving oxygen determine the pump performance and therefore the chamber pressure which ultimately sets the thrust. Therefore only the oxidizer is of interest in the model and the system does not account for ethanol apart from its contribution in achieving combustion.

In the following sections, individual components are studied and their characteristic times evaluated. In developing the system's governing equations, additional schematics are provided when necessary to better illustrate the processes involved. Pressures and temperatures refer to static values except for those pertaining to the turbine inlet and exit stations where they refer to stagnation temperatures. Furthermore, the gas state equation ($P = \rho RT$) is assumed whenever gaseous oxygen is being considered in the model.
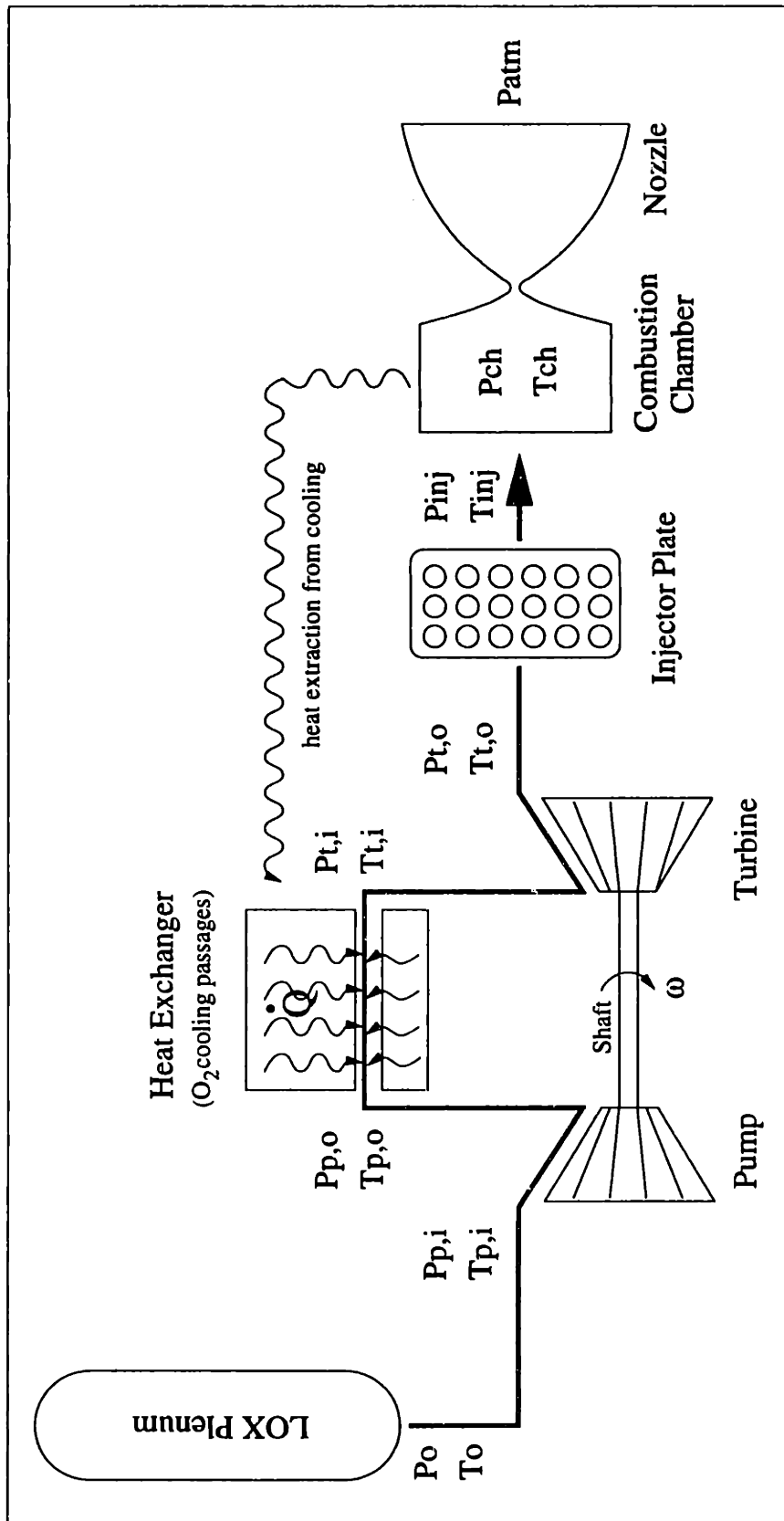
Figure 5-1: System Model Layout.

5.2.2 Component Models

Turbomachinery

The turbomachinery discussed here refers to that described in the chapter on Pumping System Characteristics (Chapter 2). The startup dynamics however require the addition of an inertia parameter to account for the acceleration transients in the system. The pumping system shown on Figure 2-8 is a basis of the micro-rocket concept. Understanding its performance is crucial in establishing the rocket response time and thus its functionality as well as determining its margin of operation.

The conservation of angular momentum may be written as:

$$I\dot{\omega} = T_{turbine} - T_{pump} \tag{5.1}$$

where I is the pump-turbine inertia, T the respective torque, and ω the angular velocity.

Multiplying both sides of the equation by ω and using the left hand side of equation 5.1 to express the pump and turbine power difference, the unsteady power balance equation becomes:

$$\omega(I\dot{\omega}) = \dot{m}Cp(T_{t,o} - T_{t,i}) - \dot{m}\frac{(P_{p,o} - P_{p,i})}{\eta_p \rho} \tag{5.2}$$

where η_p is the pump efficiency. The turbine efficiency is not mentioned since it is inherently contained in the expression for the pressure ratio across the turbine stage (see Chapter 2). (Other notations refer to Figure 5-1).

Oxygen is assumed to enter the pump in the liquid state. While this assumption has been relaxed in studying the feasibility of a gas fed pump it has nevertheless been enforced for most calculations. Fluid behavior well beyond the critical point tends to resemble that of an ideal gas [29]. However, for modeling purposes, where the goal is to obtain characteristic times and feasibility studies, the fluid was considered to remain in the liquid state (constant density) throughout the entire span of the pump. For further details concerning the pump and turbine, refer to Chapter 2.

Injectors

Injectors (see Figure 5-2) were treated as choked throughout the entire start-up time period. This assumption is valid if a minimum pressure ratio of about two is maintained between the inlet and exit stations of the injector plate. The statement is reasonable (assuming no significant pressure losses in the cooling passages) if the device is tested at 1 atm with an upstream supply tank pressure above 3 atm. Assuming isentropic flow, the injector exit pressure $P_{inj,e}$ may then be related to the inlet pressure $P_{inj,i}$ by the following relation [29]:

$$P_{inj,e} = P_{inj,i}(\frac{2}{\gamma+1})^{\frac{\gamma}{\gamma-1}} \tag{5.3}$$

and similarly for the injector inlet temperature $T_{inj,e}$:

$$T_{inj,e} = T_{inj,i}(\frac{P_{inj,e}}{P_{inj,i}})^{\frac{\gamma-1}{\gamma}} \tag{5.4}$$

Mass flow rate then follows from continuity :

$$\dot{m} = \sqrt{\frac{\gamma}{R_g}}\frac{P_{inj,e}}{\sqrt{T_{inj,e}}}C_D A_{inj} \tag{5.5}$$

where C_D is the discharge coefficient used to account for blockages due to the sharp inlet corners imposed by microfabrication. Here, A_{inj} represents the total equivalent injector plate area for oxygen, $\dot{m}$ the oxidizer mass flow rate, γ the fluid specific heat ratio and R_g the gas constant for oxygen.

Reconciling the above description with the system schematic in Figure 5-1 requires one clarification concerning nomenclature. The injector inlet pressure and temperature refer to the turbine exit pressure and temperature respectively. (Figure 5-1 however, only features the exit quantities referring them as P_{inj} and T_{inj}).

Combustion Chamber

The combustion chamber was modeled as a heat source which generates a constant temperature at the onset of combustion. Whereas in reality, chamber temperature is pressure dependent, the relationship is weak especially at the high pressures required to instigate

ignition. Combustion temperature was therefore held constant throughout the simulation at 3000 K (as determined by the thermochemical calculations). Pumping response time has been evaluated to lie in the range of 10^{-4} seconds (as demonstrated further on), and since the characteristic time required to complete combustion is on the same order, the model also features a combustion time lag. The combustion temperature time delay (τ_{comb}) accounts for both reaction and mixing times. The residence time (τ_{res}) is defined as the amount of time the mixture spends inside the chamber and is thus proportional to the chamber volume, for a given mass flow. In the case where τ_{res} is less than the required combustion time τ_{comb}, combustion cannot occur and the chamber temperature is set to room temperature (300 K). In addition, τ_{comb} varies approximately inversely with pressure. The Chamber temperature is thus given by:

$$
T_{ch} = \begin{cases} 300\text{K} & \text{for } \tau_{res} < \tau_{comb} \text{ or } t < \tau_{comb|P_{ch}} \\ 3000\text{K} & \text{for } \tau_{res} \geq \tau_{comb} \text{ and } t \geq \tau_{comb|P_{ch}} \end{cases}
\tag{5.6}
$$

where t is the simulation time, P_{ch} the chamber pressure, τ_{res} the residence time and $\tau_{comb|P_{ch}}$ the combustion time (mixing and reaction) associated with P_{ch}.

The combustion time delay may be expressed in terms of the chamber pressure as:

$$
\tau_{comb} = \frac{P_{ch,ref}}{P_{ch}} \tau_{comb,ref}
\tag{5.7}
$$

where $P_{ch,ref}$ is a reference chamber pressure and $\tau_{comb,ref}$ its associated combustion delay time.

Assuming a choked isentropic nozzle flow where A_t is the throat area, the chamber pressure P_{ch} may be evaluated using classical theory [24] as:

$$
P_{ch} = \frac{\dot{m}\sqrt{\gamma R_g T_{ch}}}{A_t \gamma (\frac{2}{\gamma+1})^{\frac{\gamma+1}{2(\gamma-1)}}}
\tag{5.8}
$$

Figure 5-3 shows a schematic of the combustion chamber illustrating the basic layout as well as the different combustion processes occurring along its span. Note however that two pressures are provided: P_{inj} and P_{ch}. Since both the injectors and the nozzle throat are choked no flow of information can occur between the two pressures.
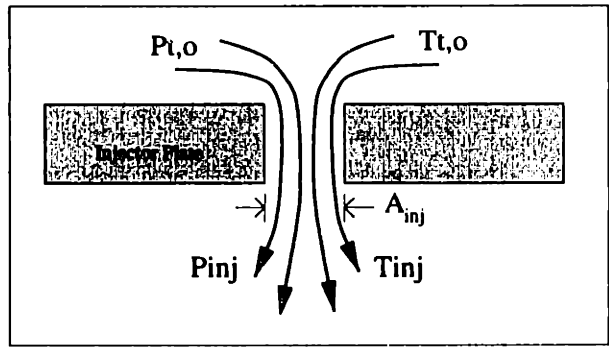
Figure 5-2: Injector Hole Schematic.
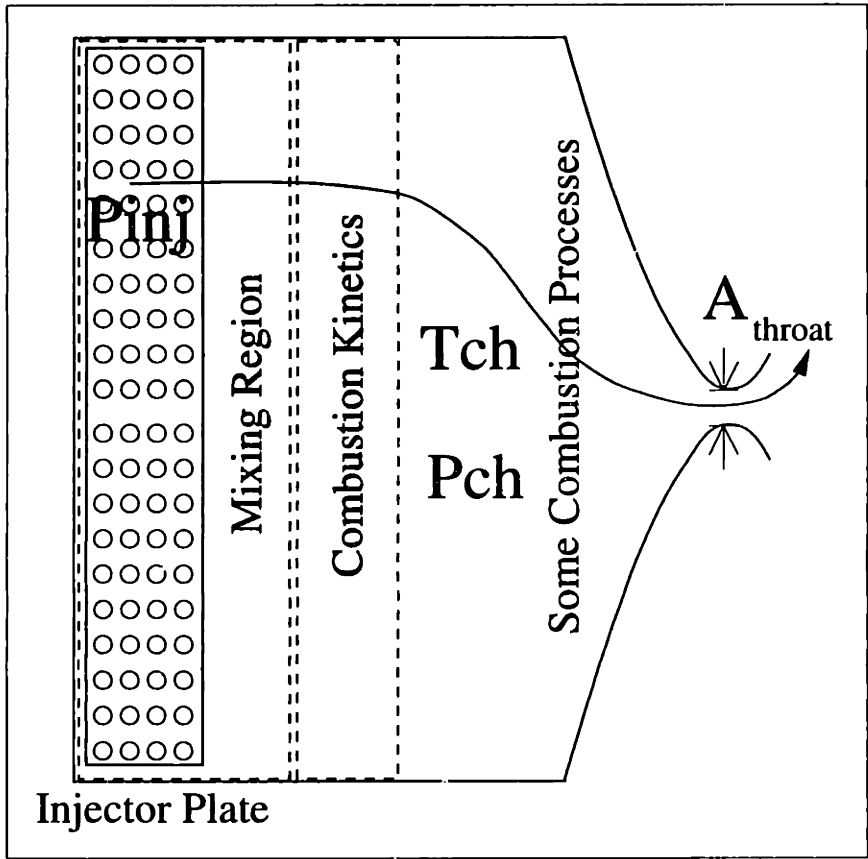
Figure 5-3: Chamber Schematic.

Heat Exchanger

The heat exchanger model accounts for the heat absorption of the working fluid (O_2) due to the cooling of the chamber and nozzle walls. The actual micro-rocket benefits from a complex cooling scheme where passages have a variable cross sectional area. This allows tailoring of the local heat transfer rate along the passage length in order to maintain constant wall temperatures and thus reduce thermal stresses in the structure. This design consideration is necessary due to the large heat transfer variations along the nozzle inner wall especially near the throat. While the model doesn't grasp the level of complexity inherent to the actual design, it does however consider representative length scales for the passage hydraulic diameter d_{hx}, its associated cross sectional area as well as its total length and area of heat exposure so as to match the total heat absorbed in the actual rocket. Figure 5-4 illustrates the basic layout and provides a starting point in analyzing the heat transfer processes involved.

The heat exchanger is composed of two walls: an inner thin wall exposed to the combustion chamber and a thicker wall representing the silicon block casing of the device. Wall temperatures may be assumed to be uniform if the convective heat transfer to the walls is significantly less than the conductive heat transfer. This assumption is considered accurate if the Biot number (Bi) is found to be less than 0.1 [9]. The Biot number is defined as $Bi \equiv \frac{h(V/A)}{k}$ where V is the block volume, A the area exposed to the cooling flow, h the heat transfer coefficient and k the conductivity of the material. For the case of the heat exchanger, h is on the order of 10^5 W/m^2-K (as will be shown further on), k on the order of 10^2 W/m-K for silicon and V/A varies between 10^{-3} and 10^{-4} meters depending on whether the inner or outer wall is considered. The resulting Bi is therefore less than 0.1 for the inner wall and about 1 for the outer casing. A lumped capacity model is therefore validated for the chamber wall liner but turns out to be less accurate for the chamber outer casing. The assumption is nonetheless maintained throughout the simulation as it does not significantly affect the system behavior. Furthermore, radiation has not been considered because its effects have been shown to be small, accounting for less than 5% of the total heat flux.

If T_{w1} and T_{w2} represent the silicon inner and outer wall temperatures respectively, then

considering the cooling fluid bulk temperature T_{bulk}, a heat balance may be performed on the heat exchanger such that for the inner wall:

$$\frac{dT_{w1}}{dt}\rho_{si}V_1Cp_{si} = h_1A_{hx}(T_{ch} - T_{w1}) - h_2A_{hx}(T_{w1} - T_{bulk}) \tag{5.9}$$

where h_1 and h_2 are the hot side (combustion chamber) and cool side (cooling flow) heat transfer coefficients (see Figure 5-4).

For the outer wall:

$$\frac{dT_{w2}}{dt}\rho_{si}V_2Cp_{si} = h_2A_{hx}(T_{bulk} - T_{w2}) \tag{5.10}$$

The fluid temperature rise is obtained by performing a heat balance on a cooling channel element of length δx and integrating the expression to obtain the resulting fluid exit temperature T_{fluid}. Since the flow time in the cooling passage is negligible next to the wall temperature transients, T_{w1} and T_{w2} are assumed constant when integrating along the cooling channel length. Referring to figure 5-4, the heat balance equation may be expressed as:

$$\dot{m}Cp\frac{dT_{fluid}}{dx}\delta x = h_2w\delta x(T_{w1} - T_{fluid}) + h_2w\delta x(T_{w2} - T_{fluid}) \tag{5.11}$$

where w is the passage width.

Integrating the above expression gives:

$$T_{fluid} = \frac{(T_{w1} + T_{w2}) - (T_{w1} + T_{w2} - 2T_{in})e^{\frac{-2wh_2L_{hx}}{\dot{m}Cp}}}{2} \tag{5.12}$$

where L_{hx} is the heat exchanger length and T_{in} refers to the fluid inlet temperature or pump exit temperature $T_{p,o}$ as indicated on Figure 5-1. The fluid bulk temperature is then simply evaluated as the average temperature across the cooling passage and is expressed as follows:

$$T_{bulk} = \frac{\int_0^{L_{hx}} T_{fluid}(x)dx}{L_{hx}} \tag{5.13}$$

The fluid stagnation temperature entering the turbine ($T_{t,i}$) is then evaluated as:

$$T_{t,i} = T_{fluid}(1 + \frac{\gamma - 1}{2}M^2)$$ (5.14)

where M is the Mach number at the passage exit.

Pressure drop across the cooling passages is estimated according to pipe flow empirical correlations [10] as follows:

$$\Delta P_{hx} = \frac{1}{2}f\frac{L_{hx}}{d_{hx}}\rho u^2$$ (5.15)

where u is the fluid velocity, f the tube friction coefficient, L_{hx} the channel characteristic length and d_{hx} its equivalent hydraulic diameter.

For the given passage, f ranges from 0.02 for fully developed laminar flow to 0.08 for turbulent flow in rough pipes [10]. For simplicity, an average constant value of 0.05 has been adopted for the friction factor. Calculations of the heat transfer coefficients h_1 and h_2 require particular attention and are discussed in the following section.

5.3   Heat Transfer Considerations

LOX enters the heat exchanger cooling passages at the pump exit pressure and temperature. Given that the boiling point for O_2 is approximately 100 K [22] for pressures near atmospheric and that the silicon walls are initially at room temperature (300 K), boiling occurs along the length of the passage up to the point where all of the oxygen has been vaporized. As pump exit pressures increase well beyond the critical pressure of oxygen, the fluid entering the heat exchanger becomes supercritical and thus no boiling can occur (surface tension becomes null beyond the critical point). The complexity of the heat transfer problem thus deserves special considerations and the establishment of a sophisticated model to realistically represent the actual processes involved. For practical purposes, a simplified model has been developed to account for both boiling and convective heat transfers. Whereas boiling doesn't occur at steady state due to the supercritical nature of the fluid (for pressures above 50 atm) it is of interest for the start-up transients as well as for determining the feasibility
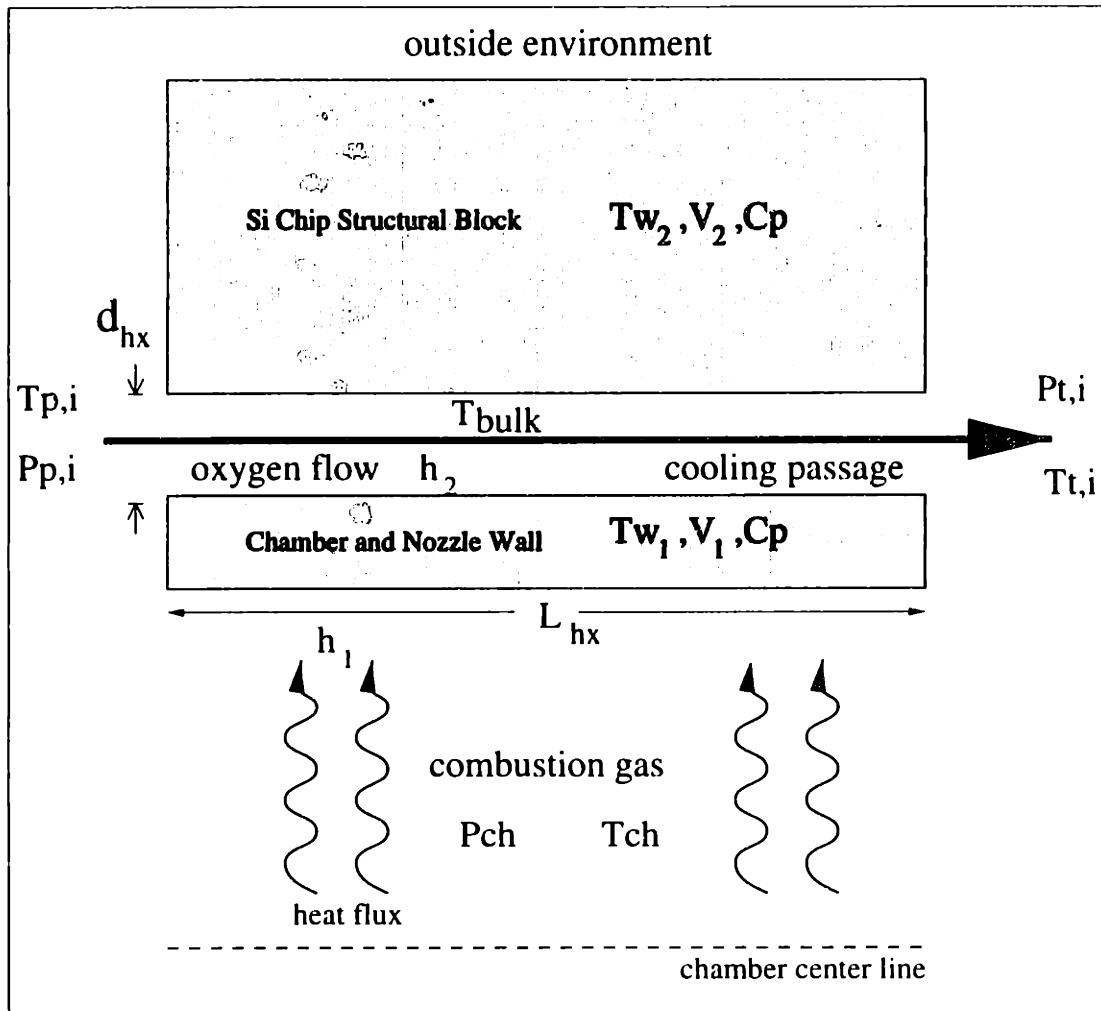
Figure 5-4: Heat Exchanger Schematic.

of a self-starting capability. Three main heat transfer mechanisms have been considered:

- convective heat transfer

- boiling heat transfer

- supercritical convective heat transfer

and the model uses each process accordingly since the fluid entering the cooling channel changes states with time (as the pump exit pressure increases from subcritical to supercritical).

5.3.1 Convective Heat Transfer

The convective heat transfer coefficient may be calculated for either gaseous flow or a two-phase mixture. In general, $h = \frac{k}{d_{hx}} Nu$ where Nu is the Nusselt number and $Nu = f(Re, Pr)$. For single phase flow, $h_{conv,1P}$ is estimated as follows [3]:

$$h_{conv,1P} = \frac{k}{d_{hx}} 0.023 Re^{0.8} Pr^{0.4} \tag{5.16}$$

where k is the thermal conductivity of the fluid. For two-phase flow (which is the case of the passage section where boiling occurs), $h_{conv,2P}$ is given by [3]:

$$h_{conv,2P} = \frac{k_l}{d_{hx}} 0.023 Re_l^{0.8} Pr_l^{0.4} F \tag{5.17}$$

where all properties are evaluated at their liquid state and two-phase flow is accounted for by a quality factor F defined as follows [3]:

$$F = \begin{cases} 2.61(\frac{1}{X_{tt}})^{0.74} & \text{for } 0.7 < (\frac{1}{X_{tt}}) < 100 \\ 2.27(\frac{1}{X_{tt}})^{0.36} & \text{for } 0.1 < (\frac{1}{X_{tt}}) \le 0.7 \end{cases} \tag{5.18}$$

The Martinelli parameter X_{tt} is given by the following relation:

$$X_{tt} = (\frac{1-x}{x})^{0.8} (\frac{\rho_v}{\rho_l})^{0.5} (\frac{\mu_v}{\mu_l})^{0.1} \tag{5.19}$$

where x is the quality of the mixture ($0 \le x \le 1$) and $x = 1$ indicates that the fluid state is 100% gaseous (all the LOX has been vaporized at this point).

Another way of writing the F-parameter involves expressing it in terms of the ratio of a two-phase and a liquid phase Reynolds number [3]:

$$F = (\frac{Re_{2P}}{Re_l})^{0.8} \tag{5.20}$$

The above expression is also useful in providing a definition for Re_{2p} as it is used further on.

5.3.2 Boiling Heat Transfer

The boiling heat transfer provided below also accounts for forced convection through the use of an S-parameter. The boiling heat transfer coefficient can be written as [3]:

$$h_{boil} = 0.00122 \frac{k_l^{0.79} C p_l^{0.45} \rho_l^{0.49}}{\sigma_l^{0.5} \mu_l^{0.29} h_{fg}^{0.24} \rho_v^{0.24}} \Delta T^{0.24} \Delta P^{0.75} S \tag{5.21}$$

where $\Delta T = T_{wall} - T_{sat}$ and $\Delta P = P_{sat|T_{wall}} - P_{sat|T_{sat}}$.

The S-parameter is defined as:

$$S = \begin{cases} 3.63 - 0.65 \log Re_{2P} & \text{for } 2 \cdot 10^4 < Re_{2P} < 3 \cdot 10^5 \\ 0.1 & \text{for } 3 \cdot 10^5 \leq Re_{2P} \end{cases} \tag{5.22}$$

Significant temperature variations of the latent heat of vaporization h_{fg} and the surface tension σ_l require some consideration in the model. Other variables are considered constant throughout the simulation. The relevant oxygen properties [22] are listed in the table provided below:

O_2 Property	Value	Units
h_{fg}	$10^3(-1.72 T_{fluid} + 305)$	J/kg
σ_l	$3 \cdot 10^{-7} - 2 \cdot 10^{-9} T_{fluid}$	kg/m
k_l	0.08	W/m-K
μ_v	$2 \cdot 10^{-5}$	kg/m-s
μ_l	$8 \cdot 10^{-4}$	kg/m-s
Cp_l	2000	J/kg-K
T_{sat}	100	K
$P_{sat|T_{sat}}$	$4 \cdot 10^5$	Pa
$P_{sat|T_{wall}}$	$P_{crit} \simeq 5 \cdot 10^6$	Pa
Pr	1.4	-
ρ_l	~ 1200	kg/m^3

Table 5.1: Oxygen Properties [22].

5.3.3 Beyond the Critical Point

Avampto et al [2] suggest that fluids at or near the critical point may exhibit a pseudo-boiling phenomena in which lumps of varying densities form (as opposed to vapor bubbles forming). At pressures well above the critical point however, supercritical heat transfer resembles very closely that of forced convection for a single phase fluid and the Nusselt number is evaluated empirically as [2]:

$$Nu_{crit} = 0.021Re^{0.8}Pr^{0.4} \tag{5.23}$$

For pressure near the critical point, the heat transfer coefficient is approximated by a weighted average of the supercritical and boiling heat transfer coefficients.

5.3.4 Passage Heat Transfer Coefficient

An overall heat transfer coefficient must now be determined for the heat exchanger cooling passage. Two main cases are considered:

- fluid inlet pressure is above the critical point.

- fluid inlet pressure is below the critical point.

In the first case, the heat transfer coefficient is simply that provided in equation 5.23. In the second case however both boiling and convection must be considered. Assuming that the fluid quality decreases linearly as a function of the passage length, h_{boil} may be calculated for discrete values of quality ranging from 0 to 1 and an average $\overline{h}_{boil}$ may be evaluated. It is then necessary to determine the length over which boiling occurs. The length L_{boil} is determined assuming that the energy required to vaporize the fluid is taken into account by the average boiling heat transfer coefficient acting on an area $A_{boil} = L_{boil}w_{hx}$ (where w_{hx} is the passage width) with a temperature difference of $T_{wall} - T_{in}$. This can be expressed as:

$$A_{boil}\overline{h}_{boil}(T_{wall} - T_{in}) = \dot{m}h_{fg} \tag{5.24}$$

96

where T_{in} is the LOX inlet temperature and thus:

$$L_{boil} = \frac{\dot{m}h_{fg}}{\bar{h}_{boil}(T_{wall} - T_{in})w_{hx}}$$ (5.25)

While running simulations, L_{boil} may be checked against L_{hx} to determine whether the tubes are sufficiently long to allow a complete vaporization of the LOX prior to entering the turbines. Otherwise, redesign of the passages may be necessary.

The passage will first be affected by $\bar{h}_{boil}$ over a length L_{boil} and then by free convection due to the gaseous oxygen flowing through the remainder of the passage length $(L_{hx} - L_{boil})$. And so, the overall heat transfer coefficient in the passage, may be obtained as a weighted average performed on $\bar{h}_{boil}$ and h_{conv} so that:

$$h_{tot} = \frac{\bar{h}_{boil}L_{boil} + h_{conv}(L_{hx} - L_{boil})}{L_{hx}}$$ (5.26)

The expression for h_{tot} is representative of all the heat transfer processes occurring in the cooling passage for subcritical oxygen. It can then be used very simply to predict the total heat flux (for $P < P_{crit}$).

5.4 Characteristic Times

A brief discussion on component characteristic times is presented in this section in order to predict the system behavior and validate the simulation results. Calculations involving orders of magnitude refer to SI units implicitly.

5.4.1 Pumping System

Considering the power balance equation 5.2, neglecting efficiency terms and expressing the pumping power as $P_p = \dot{m}(\omega r)^2$, equation 5.2 may be simplified as:

$$\dot{m}[Cp\Delta T_t - (\omega r)^2] = (I\dot{\omega})\omega$$ (5.27)

Using continuity and taking u_r as the radial velocity of the pump to be about $\frac{1}{10}$ that of its tangential velocity, $\dot{m}$ can be written as:

$$\dot{m} = \frac{1}{10}\rho(\omega r)A_p \qquad (5.28)$$

where A_p is the pump exit area. Using equation 5.27, the following differential equation may be developed for ω:

$$\dot{\omega} + \frac{\rho A_p r^3}{10I}\omega^2 - \frac{\rho A_p r C p \Delta T_t}{10I} = 0 \qquad (5.29)$$

Now let:

$$x \equiv \sqrt{\frac{\rho A_p r^3}{10I}}\omega \qquad (5.30)$$

$$a \equiv \sqrt{\frac{\rho A_p r C p \Delta T_t}{10I}} \qquad (5.31)$$

and

$$K \equiv \sqrt{\frac{\rho A_p r^3}{10I}} = \frac{x}{\omega} \qquad (5.32)$$

Expressing the pump exit area as a function of the impeller blade aspect ratio AR, A_p can then be expressed as:

$$A_p \simeq 2\pi r^2 AR \qquad (5.33)$$

Then, using equations 5.30, 5.31, 5.32 and 5.33, equation 5.29 can be rewritten as:

$$\frac{1}{K}\frac{dx}{a^2 - x^2} = dt \qquad (5.34)$$

The solution then depends on the sign of $(x - a)$. Considering that the impeller tangential velocity $u_t = \omega r$, $\frac{x}{a}$ may be written from 5.31 and 5.32 as:

$$\frac{x^2}{a^2} = \frac{u_t^2}{C p \Delta T_t} \qquad (5.35)$$

98

Given that the relevant orders of magnitude for u_t, Cp and ΔT_t are respectively 10^2, 10^3 and 10^1 (see Chapter 2), it is then clear that $x < a$ and so integrating both sides of the equation gives the following solution for 5.34:

$$\frac{1}{2Ka} \ln \frac{a+x}{a-x} = t + C_0 \tag{5.36}$$

Initially the system is at rest and so at $t = 0$, $\omega = x = 0$ and thus $C_0 = 0$. Taking the exponential of both sides now gives:

$$x = aC_1 \frac{e^{2aKt} - 1}{e^{2aKt+1}} \tag{5.37}$$

where C_0 and C_1 are constants of integration. Reorganizing the above expression and defining $F \equiv \frac{e^{2aKt}-1}{e^{2aKt+1}}$ leads to:

$$x = (Constant)F(t) \tag{5.38}$$

where:

$$0 \leq F(t) \leq 1 \tag{5.39}$$

The characteristic time for x is equivalent to that of ω and calculating the time for x to reach $\frac{9}{10}$ of its final value is equivalent to evaluating t such that $F(t) = 0.9$. The calculated time should then give a reasonable approximation for the ump time constant:

$$t \simeq \frac{\ln 19}{2aK} \simeq \frac{1}{aK} \tag{5.40}$$

Considering the pump inertia as $I = \frac{1}{2}(\rho_{si}\pi r^3)r^2 \sim \rho_{si}r^5$ then if $r \sim 10^{-3}$, the pump characteristic time may be written as:

$$\frac{1}{\tau_p} \simeq \frac{\rho}{\rho_{si}} \frac{\sqrt{Cp\Delta T_t}}{10r} \tag{5.41}$$

and from Chapter 2, $\Delta T_t \simeq 10$ and so:

$$\tau_p \simeq 10^{-4}\left(\frac{\rho_{si}}{\rho}\right) \tag{5.42}$$

99

But $\rho_{si} \sim 10^3$ and $\rho \simeq 10^3$ for LOX and so:

$$\tau_p \simeq 10^{-4} \text{ sec.} \tag{5.43}$$

which is about three to four orders of magnitude less than conventionally sized pumps.

5.4.2 Heat Exchanger

Two heat transfer mechanisms occur in the heat exchanger:

- heat conduction through the silicon walls.

- heat convection to the cooling fluid.

As discussed previously, conduction mechanisms in silicon are much faster than those involving convection and thus the characteristic time is that of the slower process (convection). The heat transfer balance may then be simplified as:

$$\rho_{si} L_c C p_{si} \frac{d(T_w - T_{fluid})}{dt} = h(T_w - T_{fluid}) \tag{5.44}$$

where L_c is a representative wall thickness. The characteristic time can now be expressed as:

$$\tau_{hx} \simeq \frac{\rho_{si} L_c C p}{h} \tag{5.45}$$

Since $L_c \simeq 10^{-3}$ m for the larger wall casing, then using the previously established orders of magnitudes for Cp and ρ_{si} gives:

$$\tau_{hx} \simeq \frac{10^3}{h} \tag{5.46}$$

Assuming a total of six passages for the oxygen flow in the cooling jacket [16], the Reynolds number becomes:

$$Re \simeq \frac{\dot{m} d_{hx}}{6 d_{hx}^2 \mu} \tag{5.47}$$

where d_{hx} represents the fluid passage hydraulic diameter. The heat transfer coefficient is approximated by the following empirical correlation:

$$h = 0.0023 \frac{k}{d_{hx}} Re^{0.8} Pr^{0.4} \tag{5.48}$$

And since $d_{hx} \sim 10^{-4}$ m (100 μm), $\mu \sim 10^{-5}$ and $k \sim 10^{-2}$ then:

$$h \simeq 10^6 \dot{m} \tag{5.49}$$

thus using equation 5.46, it can be shown that for the outer wall:

$$\tau_{hx} \simeq \frac{10^{-3}}{\dot{m}} \tag{5.50}$$

At steady state $\dot{m} \sim 10^{-3}$ kg/sec and thus the heat exchanger outer wall characteristic time may be predicted at:

$$\tau_{hx,o} \simeq 1 \text{ sec} \tag{5.51}$$

The same calculation can be carried out for the inner wall using a characteristic thickness of $L_c \sim 10^{-4}$ m. The inner wall characteristic time then becomes:

$$\tau_{hx,i} \simeq 10^{-1} \text{ sec} \tag{5.52}$$

Note however that $\tau_p \ll \tau_{hx}$ indicating that fluid transients need not be taken into account in developing the pumping system's governing equations.

5.4.3   Combustion Chamber

The combustion time lag is conservatively estimated as 100 times the minimum chemical kinetics time as a means to take into account the mixing time. It is approximated as follows:

$$\tau_{comb} \simeq 100(10^{-6}) = 10^{-4} \text{ sec.} \tag{5.53}$$

The minimum chemical reaction time of 10^{-6} sec. is obtained from chapter 3.

5.4.4 Summary of System Characteristic Times

The table below provides a brief outlook on the different component characteristic times. The heat exchanger characteristic time has been shown to be three orders of magnitude greater than either that for the pumps or the combustion chamber and thus dictates the rocket steady state time. Note however, that for a working design, transients involving the pumps and combustion chamber may be omitted from the model as they would not provide any additional information concerning performance trends during start-up. Investigating the feasibility of a design however requires the above transients in order to validate the configuration or otherwise provide insight on possible design ramifications.

System Component	τ_{char} [sec]	Driving parameter
Pump	10^{-4}	ρ
Heat Exchanger (inner)	10^{-1}	$\dot{m}$
Heat Exchanger (outer)	1	$\dot{m}$
Chamber	10^{-4}	P_{ch}

Table 5.2: Component Characteristic Times.

5.5 Numerical Procedure

Integration of the governing equations was performed with the MATLAB ODE23 solver which uses a 2nd and 3rd order Runge-Kutta method. The following steps describe the numerical procedure used in the computer simulation.

- *step 1*: Load design variables (L_{hx}, A_{throat}, C_d, μ_{hx} etc...).

- *step 2*: Initialize all pressure states to atmospheric conditions, initialize silicon wall temperatures, set time to $t = 0$.

- *step 3*: Assuming choked injectors, evaluate the mass flow rate $\dot{m}$ through the system for the given upstream pump exit pressure. (The choked condition assumption is valid if the pressure ratio across the injector plate is greater than 2 at $t = 0$. This statement is reasonably valid given that the upstream tank pressure is 5 atm and that the valve is considered to be suddenly opened at $t = 0$).

- *step 4*: Evaluate the chamber pressure and combustion temperature (determine the onset of combustion).

- *step 5*: Evaluate the turbine torque $T_{turbine}$ given $\dot{m}$ and the wheel speed ωr (at $t = 0$, ω is assumed to be essentially zero and for numerical purposes $\omega_{|_{t=0}} = 1$ rad/sec).

- *step 6*: From $T_{turbine}$ evaluate the temperature drop and equivalent pressure drop across the turbine.

- *step 7*: Evaluate the heat transfer coefficients h_1 and h_2 according to the fluid state (subcritical, critical or supercritical).

- *step 8*: Evaluate the fluid temperature rise across the cooling passage as well as its equivalent average bulk temperature.

- *step 9*: Evaluate the pressure drop through the cooling channel.

- *step 10*: Evaluate $\frac{dT_{w1}}{dt}$ and $\frac{dT_{w2}}{dt}$ and update the wall temperatures T_{w1} and T_{w2} for the next time step.

- *step 11*: From the power balance, evaluate $\frac{d\omega}{dt}$ and update the pumping system rotational speed ω for the next time step.

- *step 12*: Using the new value for ω, evaluate the pressure rise across the pump and update the pump exit pressure.

- *step 13* : Update time t.

- *step 14* : Proceed to step 3 until $t = t_{end}$.

5.6 Simulation Results and Discussion

5.6.1 System Transient Response

The system under study delivers a steady state pump pressure rise of 500 atm with an oxygen mass flow rate of 2.5 grams/sec (about half the combined total oxygen and ethanol mass flow rate of 5 grams/sec). The reason for requiring a 500 atm pressure rise as opposed to the previously stated 300 atm is discussed at the end of this section. The steady state

mass flow rate ($\dot{m}$) is determined by the total injector hole area which must be adjusted for the injector hole discharge coefficient C_D. Given $\dot{m}$, the desired pressure rise is obtained by setting the turbine rotor blade angle to its appropriate value so that it can satisfy the steady state torque requirement of the pump. The oxygen flow maximum temperature through the cooling channel can also be controlled by adjusting the channel's hydraulic diameter and thus the effective heat transfer coefficient. Table 5.3 lists the design specifications of the micro-rocket under study.

Design Variable	Description	Specification
P_{plenum}	LOX feed tank pressure	5 atm
R_{pump}	pump radius	0.5 mm
$R_{turbine}$	turbine radius	0.7 mm
η_p	pump efficiency	70%
η_t	turbine efficiency	90%
β_c'	turbine rel. turning angle	85°
d_{ch}	chamber / nozzle height	1.4 mm
d_{th}	nozzle throat width	0.37 mm
d_{hx}	passage hydraulic diameter	80 μm
w_{hx}	passage width	0.450 mm
L_{hx}	passage length	2.5 cm
t_1	inner wall thickness	100 μm
t_2	outer wall thickness	3 mm
N_p	number of O_2 passages	6
d_{inj}	injector hole diameter	21 μm
N_{inj}	number of injectors	200
C_D	injector discharge coefficient	0.6

Table 5.3: Relevant System Design Variables for the Micro-Rocket.

Pump Transient

Figure 5-5 shows the oxygen internal flow transients during the initial start-up time period. Flow pressures and temperatures are plotted over a 2 ms time period corresponding to the pumping system characteristic time. As illustrated in Figure 5-5a, the pump experiences a steep acceleration from t=0.5 ms to t=1.3 ms with an exit pressure reaching 225 atm at t=1.3 ms. After t=1.3 ms, the pump rate of acceleration is shown to start decreasing, following a second transient mode. Although the pump transient is 10 times larger than

predicted analytically, most of the acceleration occurs in the predicted time of about 10^{-4} sec. The pump characteristic time is much smaller than that of the heat exchanger wall temperature and thus the pump adjusts instantaneously to the heat exchanger initial wall temperature (300 K) and only later to the higher wall temperatures induced by combustion. The time period presented in Figure 5-5 is representative of the initial adjustment and reflects the transients dictated by the pumping system inertia. Figure 5-5b shows that during this period, the oxygen flow temperature at the passage exit is fairly constant and this fact is furthermore supported by Figure 5-6b where the wall temperature is shown to remain in the vicinity of 300 K.

Heat Exchanger Transients

After t=1 ms, the wall inner temperature starts increasing steadily, indicating the second acceleration regime of the pumping system. This acceleration regime is slower and closely follows the inner wall temperature transients. The reason for the sudden increase of the inner wall temperature at t=1 ms is explained in Figure 5-6c where the cooling passage heat transfer coefficient is shown to decrease dramatically at t=1 ms by one order of magnitude thus reducing the effective cooling in the channel. This allows the combustion processes to heat up the chamber inner wall, providing additional heating to the oxygen flow which in turn increases the turbine inlet enthalpy and thus the turbine power output. The heat transfer coefficient drop can be explained by the fact that near t=1 ms, the pump exit pressure is beyond critical at which point boiling (of the LOX) ceases to occur in the channel thus greatly reducing the heat transfer in the passage. This sudden decrease is also accompanied by a drop in the oxygen flow temperatures as shown in Figure 5-5b. The outer wall temperature however remains constant as its characteristic time is one order above that of the inner wall. The pumping system thus experiences two transient responses in this figure, a first one corresponding to pumping system inertia and a second corresponding to the heating up of the heat exchanger inner wall. Figure 5-6a shows the turbine and pump torque curves converging at t=1.5 ms, and then slowly creeping upwards as T_{w1} starts to increase.

Figure 5-7 reports the different internal flow characteristics such as passage Mach number and Reynolds number. The Mach number (Figure 5-7d) is of particular interest as it helps

to verify that the passages are not choked at any time during the start-up period. Choked passages would contradict the model assumptions and may in fact impede the start-up process. Here, M is shown to be clearly less than 1 ($M < 0.6$) which validates the system design as well as the model assumptions thus far. Another interesting plot illustrates the tube length required to completely vaporize the LOX entering the channels as a fraction of the total passage length. Figure 5-7b shows that length fraction to be under 1% thus ensuring complete vaporization of the oxygen and consequently the proper functioning of the turbine downstream of the passage.

The steady state response is illustrated on Figure 5-8. The pumping system is now shown to follow three transient modes: a first one associated with the pump-turbine inertia, a second related to the heating of the heat exchanger inner wall and a third associated with the heating of the heat exchanger outer wall. For clarity purposes, the simulation is only represented over a 0.1 sec time frame. The actual steady state time however, occurs at around 0.3 sec as the heating of the outer wall casing takes longer to reach steady state. On average, the wall temperature transients obtained in the simulation are about 5 times less than those predicted analytically (this discrepancy is representative of the round off errors involved in the determination of a characteristic time order of magnitude). The pressure drop across the cooling passage is shown to be small compared to the total pressure rise but is still significant in absolute value representing a drop of about 10 atm (see Figure 5-8a. Note that the oxygen flow temperature reaches the desired [16] value of 600 K at the passage exit as shown on Figure 5-8b. Also, the inner wall temperature is shown to asymptote the 1000 K line which corresponds to its maximum allowable design temperature (see Figure 5-8c). The wall temperature limit was chosen based on the fact that silicon begins to creep at around 900 K (its melting temperature is approximately 1600 K). For completeness, Figure 5-9 shows the same results for an engine with an outer wall casing of average thickness 0.5 mm, thinner than the 3 mm case previously studied (see Table 5.3). As expected, steady state is shown to occur earlier (0.1 sec. vs. 0.3 sec.).

The Transient "Unchoking" Problem

Designing the micro-rocket with choked injectors and a 125 atm chamber pressure at steady state requires a pump pressure rise of approximately 300 atm. A closer look at the pressure

transients however reveals that for such a design, the choked injector assumption would fail during the first transient mode of the system involving the initial pump acceleration. This is due to the fact that during the initial acceleration of the pumping system, the turbine power is used to both accelerate the pump and pressurize the fluid. The turbine power is thus not entirely devoted to increasing the pump pressure and thus the system experiences a relatively low mass flow rate to turbine power ratio as compared to steady state conditions. The chamber pressure is set by $\dot{m}$ and the injector inlet pressure by the turbine exit pressure $P_{t,o}$. During the pump initial transient mode, the temperature drop (and thus the pressure drop) across the turbine is more than that which would be required in order to deliver an equivalent mass flow rate at steady state. Thus the ratio of the chamber pressure to the injector exit pressure increases until the injectors unchoke. Having unchoked injectors would not only mitigate the validity of the transient results but would also shed some doubt on the stability of the system. Choked flow in the injectors isolate the pumping system from any combustion instabilities occurring in the chamber and thus improve the robustness of the overall design . Simulation results were obtained for a system operating at a steady state pump exit pressure of 500 atm. This pressure rise is necessary to ensure that the injectors are choked at all times during the simulation. While this excessive pressure rise maintains choked conditions at the injectors, it incurs additional pressure losses leaving a 30% additional pressure loss between the chamber and the injector plate. Figure 5-10 is a plot illustrating the ratio of the chamber pressure to the choked injector exit pressure . The ratio is thus 1 or less for choked conditions and superior to 1 for the unchoked case. Ideally, this number would be 1 at steady state so as no to incur any additional pressure drop inside the chamber. In our case however, the minimum required pump pressure rise ensuring a maximum ratio of 1 during the pump transients was found to be 500 atm. This leaves a steady state ratio of about 0.7 for $\frac{P_{ch}}{P_{inj}}$ (see Figure 5-10), indicating appreciable pressure losses in the system.

An important question is whether the micro-rocket design should enforce choked conditions at all times or only during steady state. In order to better answer this question, one must compare the instability growth characteristic time with the time period during which the injectors are unchoked. If the time characteristic for the instability growth is much larger than the unchoked time period than the micro-rocket design need not account for the

transients and thus a 300 atm pump would be adequate. Otherwise, design considerations must include transient behavior requirements.

5.6.2   Start-Up Feasibility

In this section , the system was evaluated under two possible conditions:

- Start-up with a low heat exchanger initial temperature.

- Start-up with gaseous O_2 ingestion into a turbine-driven compressor system.

The first test was performed in order to evaluate the feasibility envelope of the regeneratively cooled system. Results have suggested that due to the large L/d ($L/d > 100$) present in the cooling passages, the boiling heat transfer is sufficiently large to vaporize the entire LOX mass flow rate as long as the initial wall temperature is $5°$ above saturation. Starting at cool wall temperatures is thus not a limiting issue for the self-starting capability of the rocket.

The second test was performed in order to determine whether the rocket would start if the LOX were to be fully or even partially vaporized in the delivery channels, before entering the pump. This test was conducted by changing the pump model to a gas compressor model and evaluating the system performance. The system was observed to develop a maximum pressure rise of 15 atm with a mass flow rate on the order of 10^{-4} kg/sec. Thus gas ingestion severely impedes the system performance and must absolutely be avoided. Further work is required in order to elaborate a delivery scheme which would allow for the LOX to enter the pump in a 100 % liquid state (subcooling may only be part of the solution).

5.6.3   Sensitivities

A sensitivity analysis was performed in order to test the robustness of the design as well as to identify any inherent instability with the present layout. The system performance was checked against 13 key variables and oxygen fluid properties. Sensitivity tables were obtained by varying the variables individually by an amount of ± 10% (depending on the case) and observing the percent change in crucial system performance indicators. These

108

represent the pump exit pressure $P_{p,o}$, the chamber pressure P_{ch}, the mass flow rate $\dot{m}$, the fluid maximum temperature T_{fluid} and the silicon maximum wall temperature T_{w1}. System sensitivities to uncertainties in oxygen fluid properties and pertinent design variables are recorded in tables 5.4 and 5.5 respectively. Note however that a blank entry ('-') signifies that the percent change is less than 0.5% and is thus negligible.

Sensitivities to Uncertainties in Fluid Properties (see Table 5.4)

It was observed that the sensitivities of the fluid and wall temperatures are negligible to uncertainties in the fluid properties to the exception of the Prandtl number (Pr). Uncertainties in Pr have an important effect on temperatures (about double that of the uncertainty in the fluid property itself) and thus a detailed design of the rocket would require an accurate representation of the physical properties involved especially if wall temperatures are designed to remain at only 200 K below melting. Note that the Prandtl number also greatly affects the system performance (20% for the pump exit pressure and about 10% for the mass flow rate and chamber pressure). Uncertainties in the oxygen viscosity were found to have a negligible impact on the system. Errors in the specific heat ratio γ were shown to have a multiplier effect of 200% on the system mass flow rate and chamber pressure thus suggesting again an accurate representation of fluid properties for a detailed design.

Fluid Property (% change)	$\%\Delta T_{fluid}$	$\%\Delta T_{w1}$	$\%\Delta P_{p,o}$	$\%\Delta P_{ch}$	$\%\Delta\dot{m}$
ρ_{liq} (+10%)	-	-	+9	+9	+8
γ(+10%)	+1	+1	-9	-17	-21
μ_{hx} (+10%)	-	+3	-	-	-
Pr (+10%)	+21	+23	+20	+10	+8

Table 5.4: System Sensitivities to Uncertainties in the Oxygen Fluid Properties.

Sensitivities to Design Variables (see Table 5.5)

The turbine rotor blade relative turning angle β'_c was found to have a very large impact on the system performance, as much as a 600% multiplier effect on the pump exit pressure. This is due to the fact that the high steady state pressure requirement of 500 atm (mentioned

Property (% change)	$\%\Delta T_{fluid}$	$\%\Delta T_{wl}$	$\%\Delta P_{p,o}$	$\%\Delta P_{ch}$	$\%\Delta \dot{m}$
P_{plenum} (+10%)	-	-	-	-	-
$R_{turbine}$ (+10%)	+1	+1	-22	-17	-17
R_{pump} (+10%)	-	-	-5	-4	-4
η_{pump} (+10%)	-	-	+9	+9	+8
$\eta_{turbine}$ (+10%)	-	-	+1	+6	+5
β'_c (-10%)	+3	+2	-63	-56	-58
d_{ch} (+10%)	-5	-6	-4	-2	-4
A_{inj} (-10%)	+1	+1	-15	-19	-21
d_{hx} (+10%)	-	+4	-	+1	-

Table 5.5: System Sensitivities to Design Alterations and Uncertainties.

previously) imposes a very large turning angle on the turbine blade (about 85°). Since turbine power relates to the tangent of the angle, sensitivity becomes significant as the derivative of the tangent increases rapidly when the angle approaches 90°. A 300 atm design however, would require an 80° blade turning angle which would reduce the multiplier effect to 200% (a more reasonable value). There is therefore an incentive to lower the steady state design pump pressure to 300 atm. Doing this would require a combustion stability analysis as that particular design would feature unchoked injectors during the start-up transients.

Another important design issue addresses the injectors. The uncertainty in the injector total area impacts the mass flow of the system by a multiplier effect of 200%. This is a very important fact since the injector total effective area is based on both geometry and an approximative estimation of the injector area discharge coefficient C_D. Errors may then multiply as uncertainties may accrue in both the C_D and the injector hole area simultaneously. This issue must be addressed by stressing a high tolerance in the manufacturing process as well as accurately evaluating the discharge coefficient of the injector through experiments and/or CFD analyses.
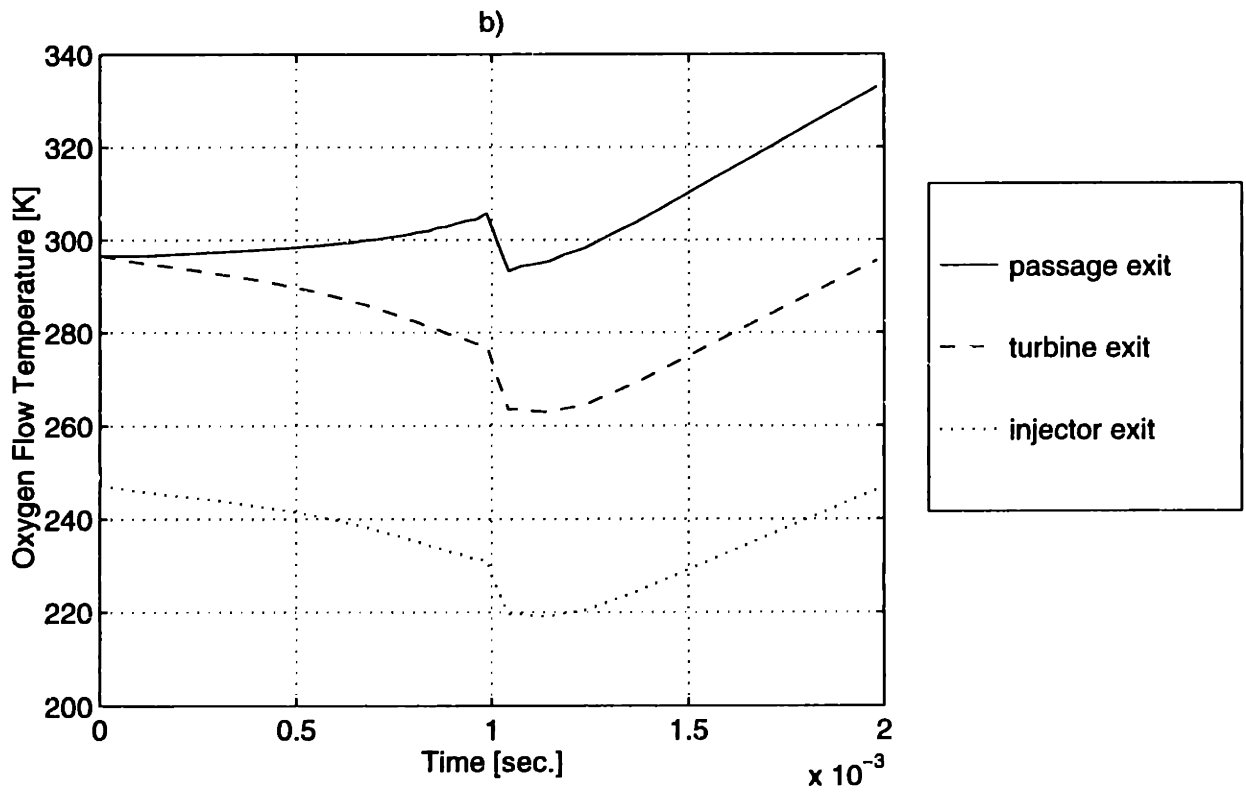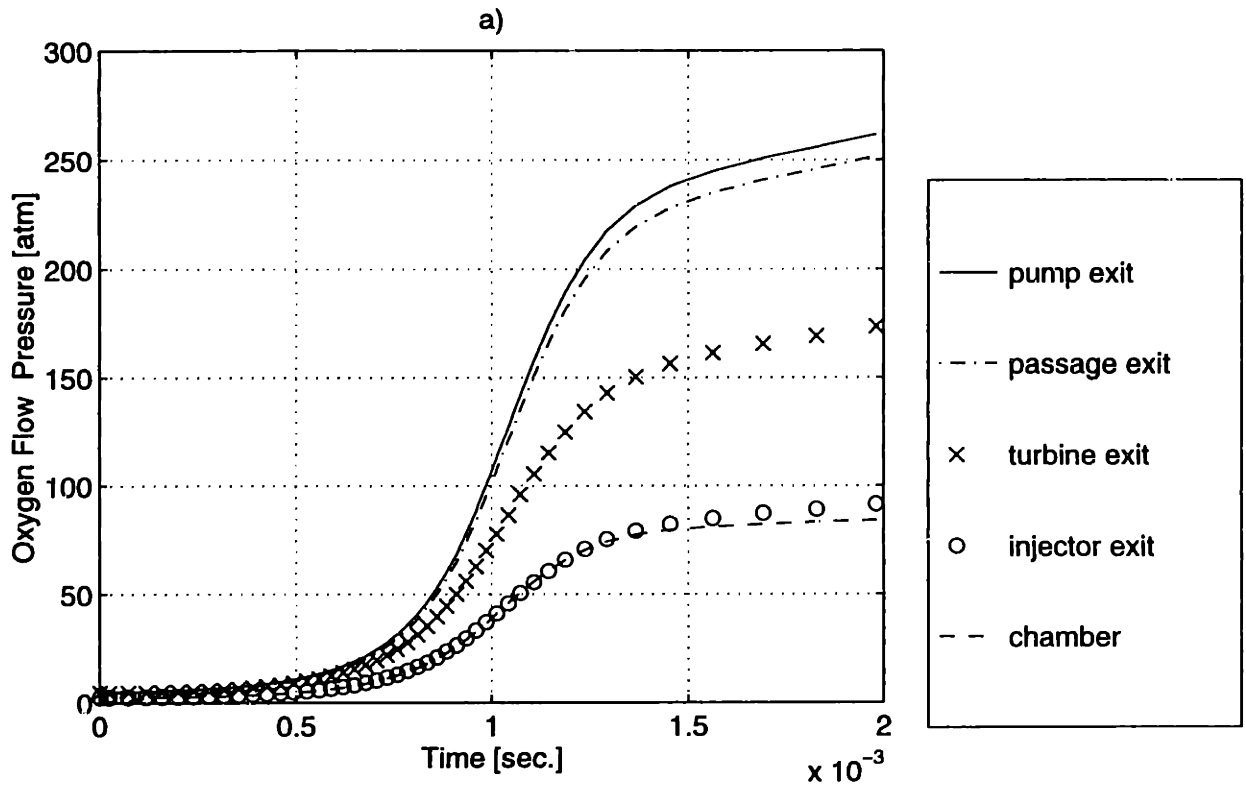
Figure 5-5: Oxygen Flow Pressure and Temperature Transients.
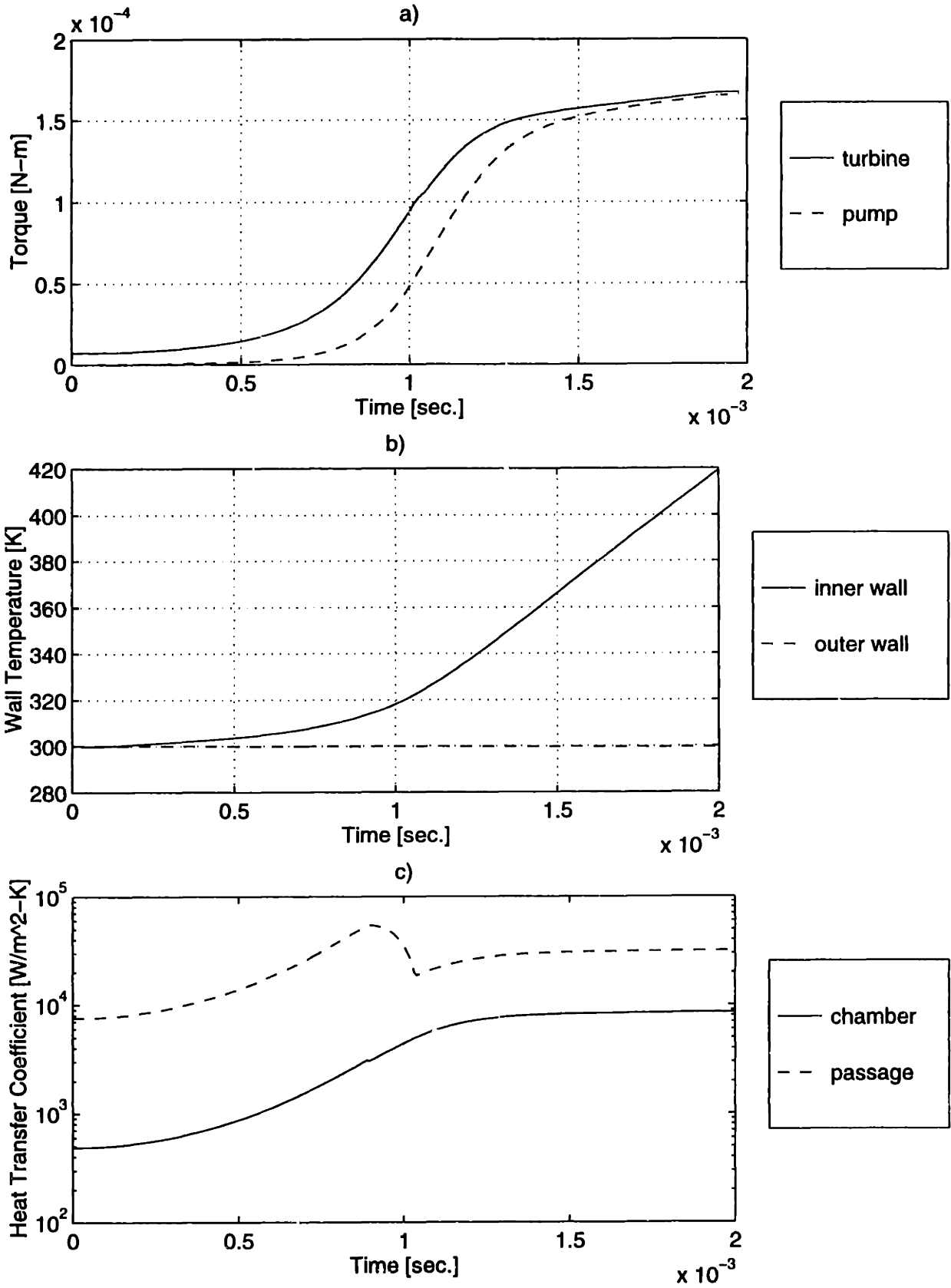
Figure 5-6: Detailed Characterization of System Transients -1-.
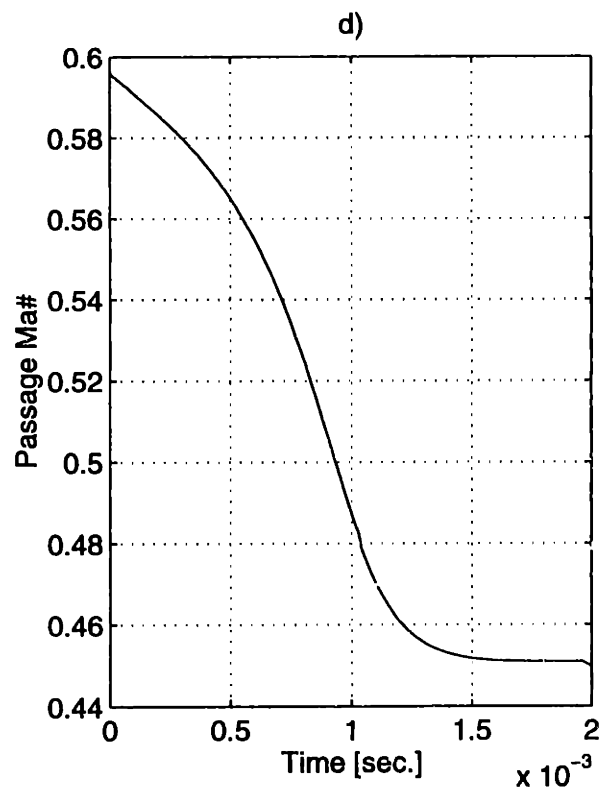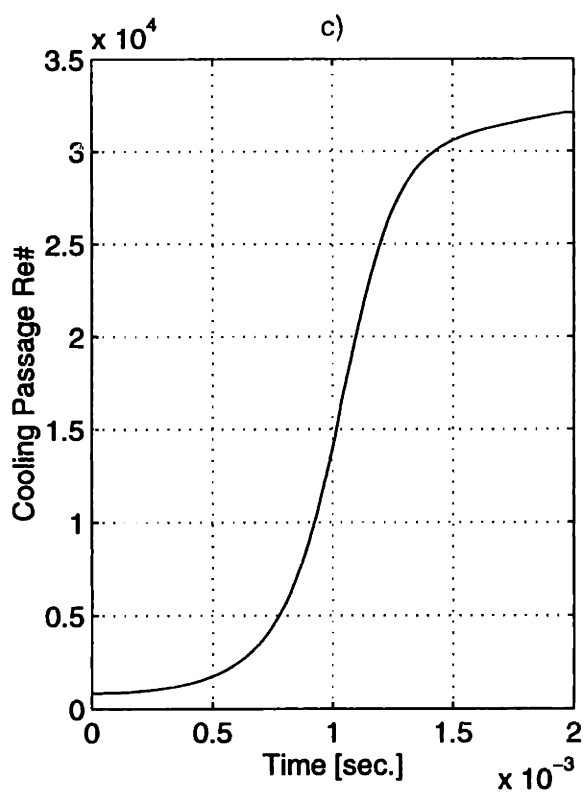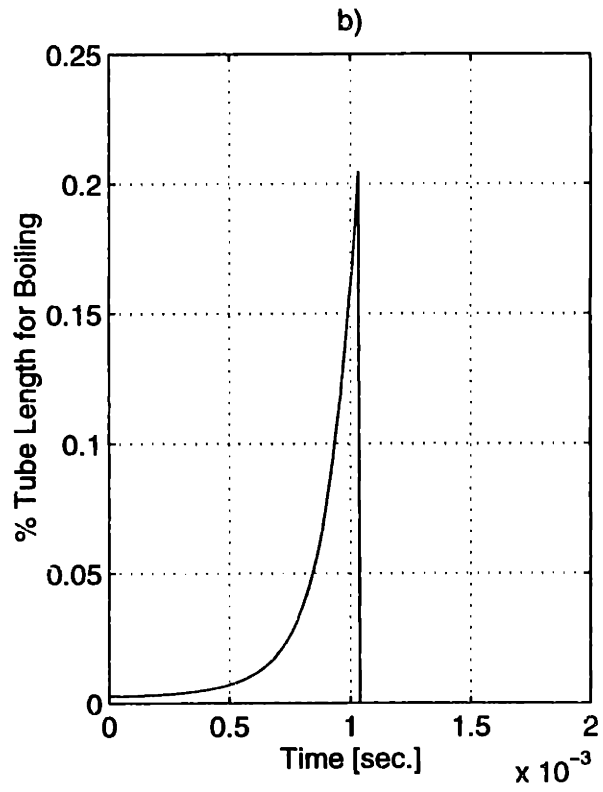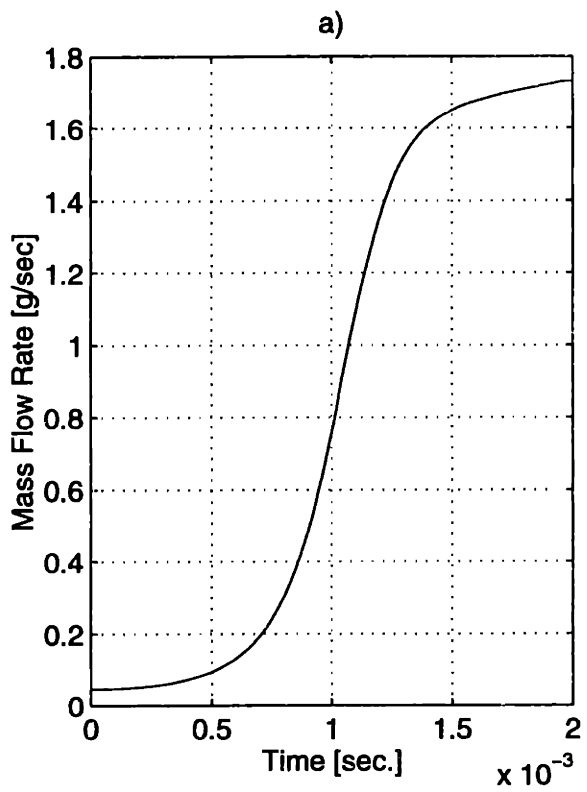
Figure 5-7: Detailed Characterization of System Transients -2-.
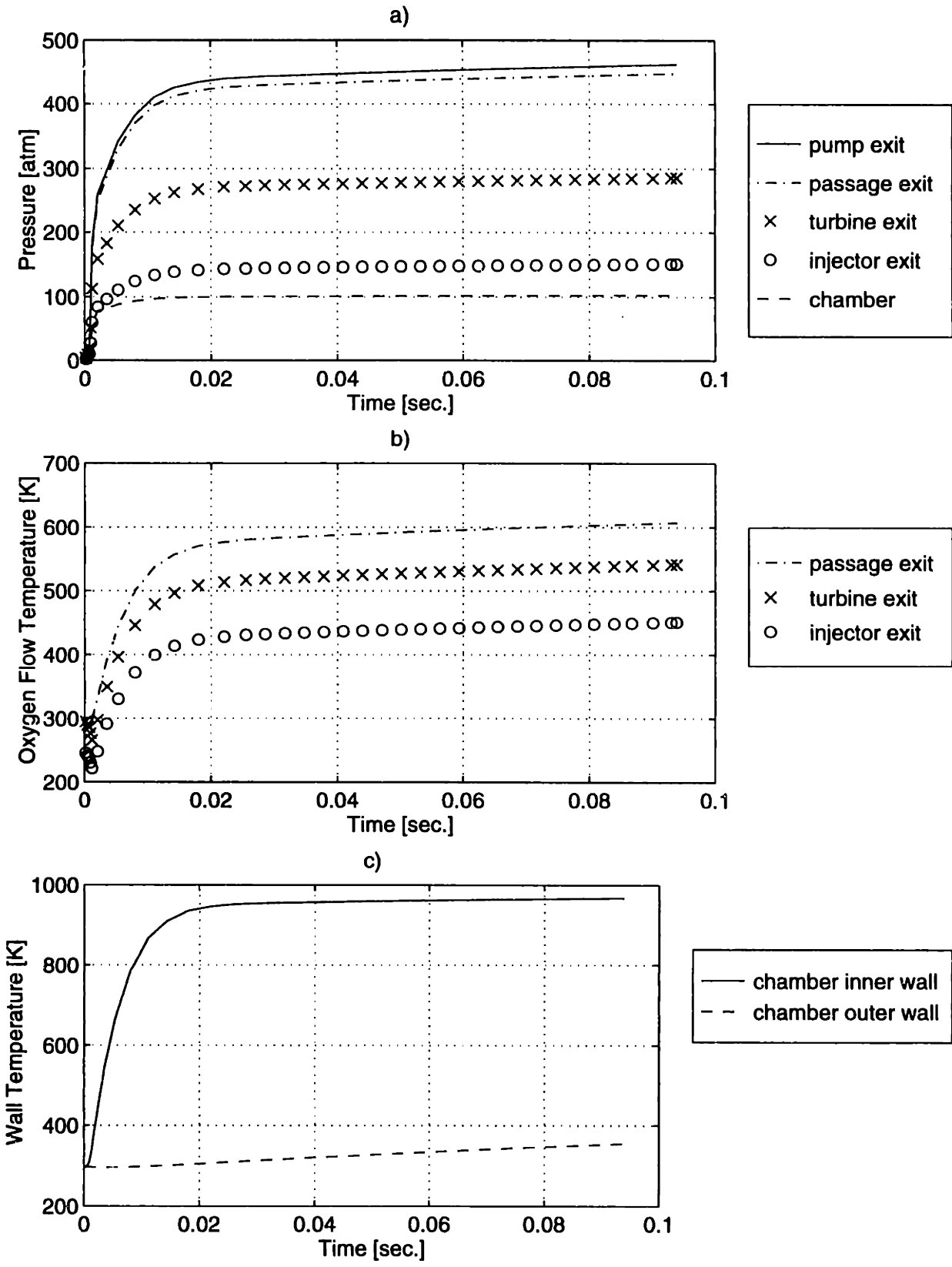
Figure 5-8: Characterization of System Approaching Steady State (outer wall thickness set at 3 mm).
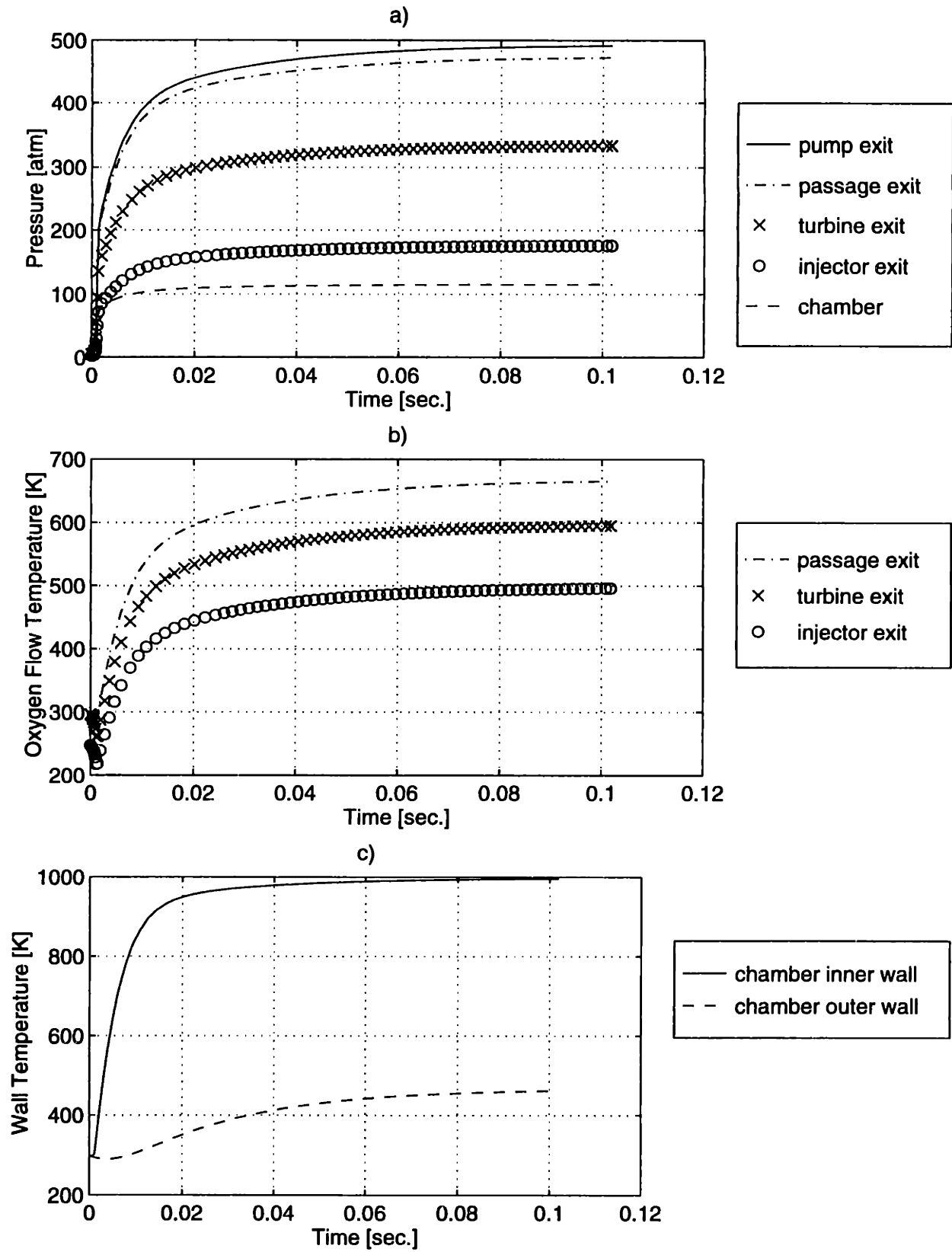
Figure 5-9: Characterization of System Having Reached Steady State (outer wall thickness set at 0.5 mm).

115
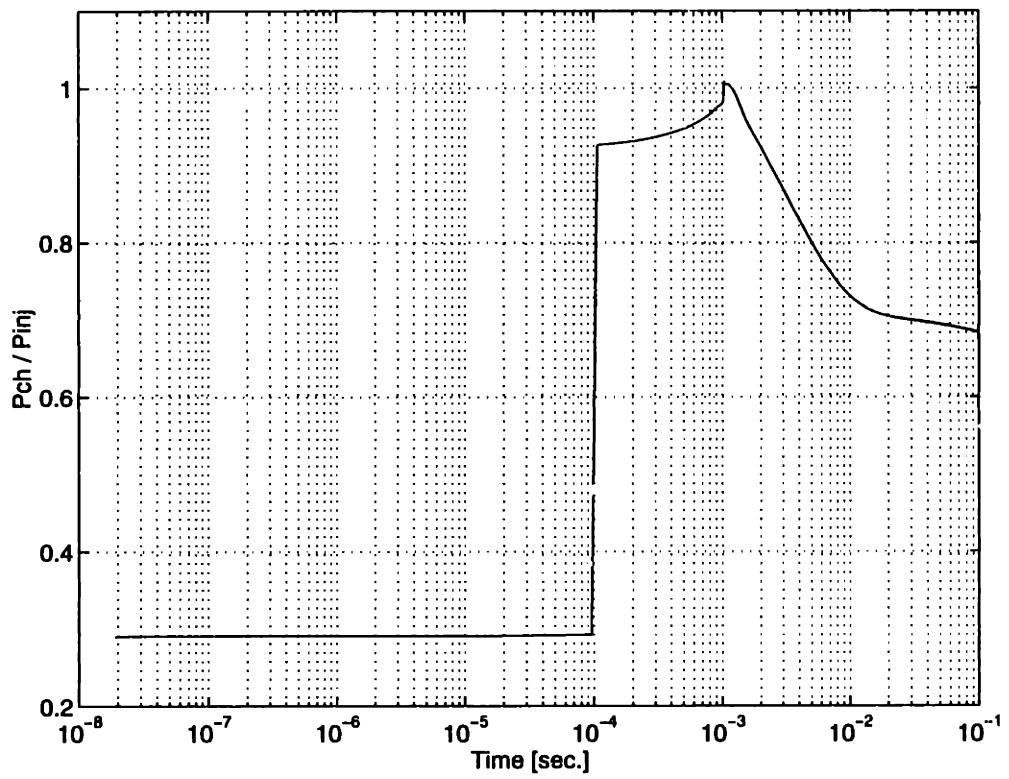
Figure 5-10: Injector Choking State During Pumping Transients.
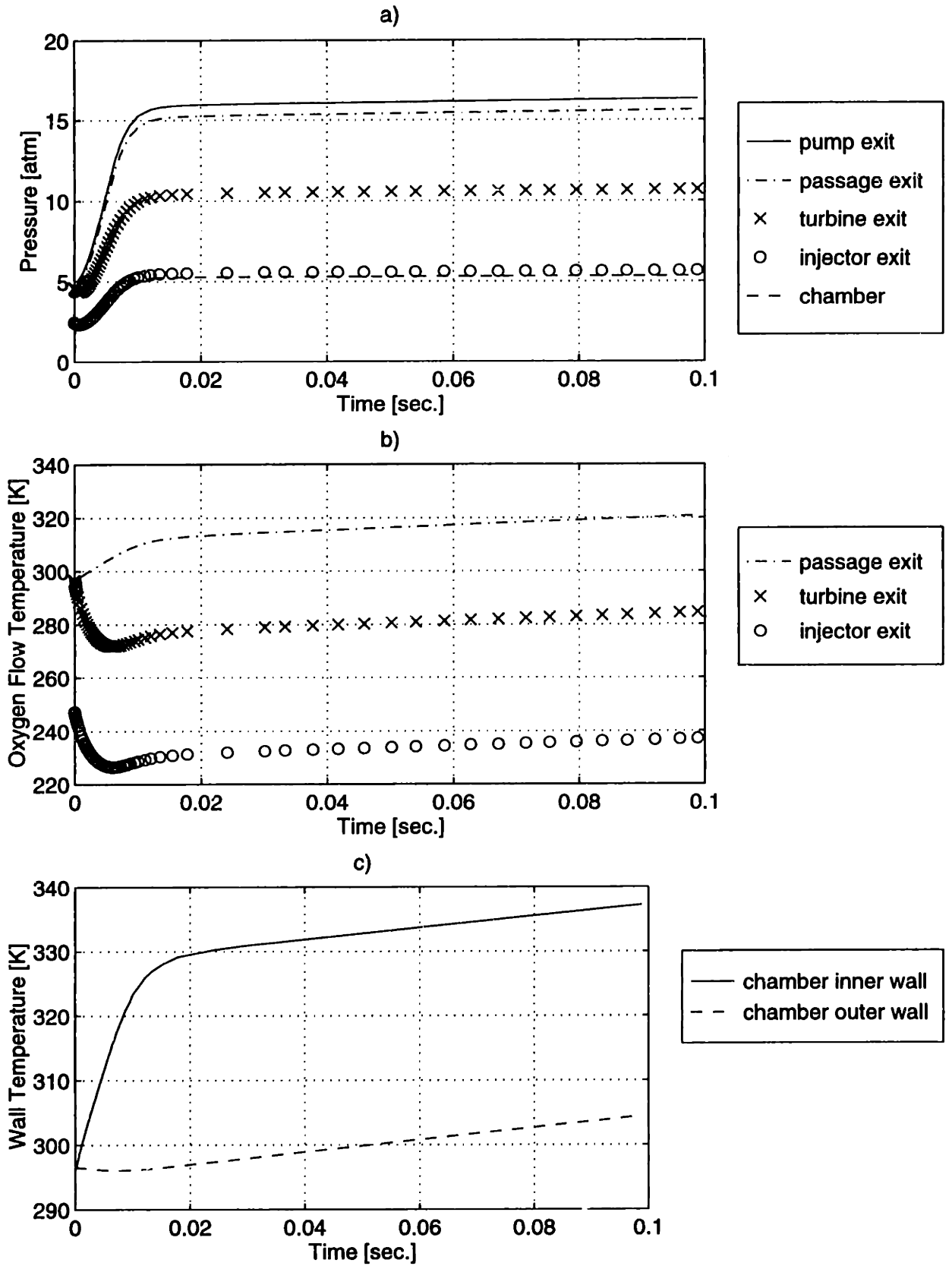
Figure 5-11: Feasibility of Gas Ingestion Start-Up.

CHAPTER 6

CONCLUSION

In the first chapter, the concept underlying the design of a micro-rocket engine was introduced. The device was shown to have tremendous advantages for satellite and other aerospace applications by significantly reducing the weight of the propulsion system. Performance implications translate into an increase in payload or an equivalent increase in propellant storage capacity. Overall, the concept allows for a significant reduction in launch and operation costs as well as an extended life in orbit.

This thesis has focused on the characterization of the various engine components including pumps, the combustion chamber and the thrusting nozzle. Research findings are summarized below followed by recommendations and a brief discussion on future project endeavors.

6.1 Summary of Work

6.1.1 Pumps

Two pumping systems have been analyzed including a micro-electrostatically driven pump and a micro-turbopump. While electrostatic motors have been suggested to offer greater control and system modularity (i.e. mass flow throttling), performance analyses have suggested that they may not provide sufficient power to drive the propellant pumps (requiring

$\simeq 75$ Watts each). The turbopump concept, on the other hand was shown to be feasible for fluid pressurizations up to 500 atm. This is explained by the fact that the energy stored into the cooling fluid through the regenerative cooling processes is more than sufficient to run the propellant pump turbines. The current design features a pump impeller radius of 0.5 mm and a turbine radius of 0.7 mm. Bearing performance still remains unanswered and while preliminary considerations indicate that the current pump layout is feasible from a stability standpoint, additional comprehensive analyses would still be required to fully validate the system.

6.1.2 Chamber

The combustion chamber temperature for an ethanol/LOX mixture was evaluated to be 3000 K for a O/F mass ratio of 1.15. Thermochemical calculations have indicated a minimum combustion residence time on the order of 1 μs assuming perfectly mixed propellants. Chamber size thus ultimately depends on the mixing times thus reinforcing the need to develop a high performance injection and mixing scheme. Conventional mixing practices have been considered inadequate for the micro-chamber sizes at stake and thus a new injection scheme was proposed. It is composed of hundreds of inter-digitated fuel and oxidizer injectors, impinging at a 180° angle. Jets run across the chamber walls, hoping to create a superior mixing environment which would allow sustained combustion for chamber sizes of 1 cm or less. Ultimate validation will take place during an actual firing test.

6.1.3 Nozzle

The nozzle flow characteristics have been analyzed for viscous losses and flow separation using a CFD 2D solver (SPARK [12]). Several nozzle configurations were studied indicating that the nozzle length could be significantly reduced without incurring notable performance losses. The baseline design was set to a nozzle length of 4.6 mm, a throat width of 480 μm and an overall aspect ratio of 0.8. Viscous losses were shown to be minimal for this configuration for a total thrust performance loss of 2% as compared to the calculated ideal thrust. 3D viscous effects have been argued to add an additional loss of about 2% for a total viscous loss of 4% (3D CFD analyses would be required to better support the latter

assumption). The micro-rocket nozzle configuration thus seems feasible and viscous effects do not appear to significantly affect performance at these scales (~ 1 mm).

6.1.4 Overall System

The micro-rocket engine system behavior was evaluated by modeling the system components and physical processes and performing simulations of the start-up transients. The system was found to reach steady state in under 1 sec., attaining 50% thrust in 1 msec. and 80% thrust in under 10 msec., thus opening the door for possible thrust pulsing capabilities. Designing the micro-rocket with choked injectors for steady state operation was shown to cause unchoking during the initial pump acceleration phase for a pumping requirement of 500 atm or less. This may come as an issue if combustion instabilities occur and if their characteristic time is on the order of the unchoked time period (~ 1 ms). Additional investigation would be required in that area.

Sensitivity analyses have indicated that careful attention must be paid to the turbine blade turning angle and the injector hole diameter as errors would have a significant multiplier effects (≥ 2). Feasibility studies involving a gaseous pump have demonstrated such a system incapable of delivering the pressures required for the micro-rocket engine. This issue becomes important for the case of the LOX pumps where vaporization at the impeller surface cannot be tolerated. Further investigation is required to ensure proper fluid quality for the LOX pump impeller. Solutions may include subcooling of the LOX tanks, having thermally isolated LOX deliver channels or even incorporating the LOX pumps as part of the LOX tanks.

6.2 Future Work and Recommendations

The following provides the reader with both recommendations on the research work presented in this thesis as well as a discussion on the future work scheduled until project completion.

6.2.1 Recommendations

Whereas the development of the first microfabricated rocket engine will not feature a pumping system, a detailed analysis and complete characterization of the pumping system is required. This includes bearings and airfoil aerodynamics (pump and turbine side). Also, a full 3D evaluation of the nozzle would be required so as to gain better understanding of the three dimensional effects occurring in the nozzle (i.e. expansion waves, shocks, blockage). Finally, thermal calculations must be performed on the pumping system in order to model the heat transfer rates on the impeller side as this constitutes a fundamental issue in validating the present layout for the LOX pumps. The goal is to confirm that vaporization will not occur in the pumps or to devise a scheme which would prevent it from happening in the first place.

6.2.2 Future Work

The following list provides a brief summary of the future endeavors required to drive this project to completion:

- Characterization of the ethanol heat transfer rates at high pressures and high heat flux rates: This effort, currently under way [17], aims to evaluate ethanol as a coolant as well as provide insight on cooling passage design specifications.

- Final detailed design: Work will essentially regroup all of the findings to date including experimental heat transfer data, CFD results and system analyses in order to establish a baseline design to be built and tested.

- Fabrication and assembly: This task involves fabrication and bonding of the rocket layers.

- Development and testing of a water cooled rocket: This experimental procedure was found to be quick and effective in providing valuable data which could then be used to refine or update the current baseline design.

- Work involving micro-valves: Micro-valves have not yet been considered and thus the necessity to develop a valve system or borrow from existing technology (if available).

- Devising an ignition scheme: The solution must take into consideration fabrication and pressure seals given that pressure gradients across wafers can be as large as 100 atm.

- Researching alternate propellants: One goal would be to replace the LOX with an non cryogenic oxidizer due to the possible vaporization which may occur in the impeller (not to mention propellant storage difficulties).

- Pump design and integration: This constitutes the final and probably most complex part of the project.

- Testing and design re-iteration: This will be pursued at several stages of the product development phase (i.e. water-cooled rocket, ignition testing and turbopump integration).

Appendix A

Perfectly Stirred Reactor Code (ChemkinII-PSR)

A.1 Governing Equations [20] & [21]

Given the mass flow rate ($\dot{m}$) and chamber volume (V), the residence time is determined as follows [20]:

$$\tau_{res} = \frac{\rho V}{\dot{m}} \tag{A.1}$$

The density of the fluid mixture is then calculated from the ideal gas equation of state:

$$\rho = \frac{P\overline{W}}{RT} \tag{A.2}$$

where $\overline{W}$ is the mean molecular weight of the mixture, and R the universal gas constant.

The mass conservation of species between the inlet and outlet stations is given by [20]:

$$\dot{m}(x_k - x_k^i) - r_k W_k V = 0 \tag{A.3}$$

where x_k is the mass fraction of species k, W_k its corresponding molecular weight, and r_k the molar rate of production of species k (by chemical production) inside the chamber.

The conservation of energy equation then takes the following form [20]:

$$\dot{m} \sum_{k=1}^{K} (x_k h_k - x_k^i h_k^i) + Q = 0 \qquad \text{(A.4)}$$

where h is the specific enthalpy for species k, and Q is the heat loss through the reactor walls.

The molar rate of production r_k represents the balance of the individual forward and reverse reaction rates for each chemical reaction involving species k. In reality, the total number of equations involved in the actual combustion processes is far too large to model and thus a smaller number of elementary reactions must be selected.

The chosen set of chemical reactions may be expressed as:

$$\sum_{k=1}^{K} \nu_{kj}' \chi_k \; \underset{\longleftarrow}{\overset{\longrightarrow}{}} \; \sum_{k=1}^{K} \nu_{kj}'' \chi_k \qquad (j = 1, ..., J) \qquad \text{(A.5)}$$
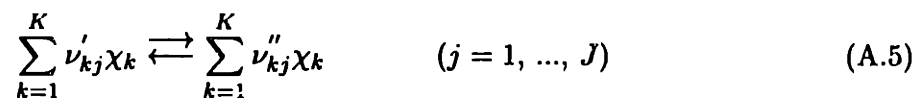
where J is the total number of representative chemical reactions, χ_k the chemical symbol for species k, ν_k the stoichiometric coefficient for species k involved in reaction j and superscript j is the chemical reaction index.

The rate of progress q_j is defined as the rate at which equilibrium is reached for the jth reaction and is expressed as [21]:

$$q_j = k_{fj} \prod_{k=1}^{K} [\chi_k]^{\nu_{kj}'} - k_{rj} \prod_{k=1}^{K} [\chi_k]^{\nu_{kj}''} \qquad \text{(A.6)}$$

where k_{fj} and k_{rj} are the forward and reverse rates for the jth reaction and $[\chi_k]$ is the molar concentration of the kth species.

The forward rates are assumed to be expressed in the modified Arrhenius form [21]:

$$k_{fj} = A T^\beta \exp(\frac{-E_A}{RT}) \qquad \text{(A.7)}$$

where E_A is the activation energy for the reaction, T the mixture temperature, R the universal gas constant and A and β are constants specific to the reaction.

The reverse rate can also be obtained for a given reaction as a function of the forward

rate, the stoichiometric coefficients for the reaction, the combustion temperature T and the change in entropy ΔS and enthalpy ΔH associated with the reaction so that [21]:

$$k_{rj} = f(k_{fj}, T, \nu''_{kj}, \nu'_{kj}, \Delta S, \Delta H) \tag{A.8}$$

The molar rate of production for the kth species is then expressed as:

$$r_k = \sum_{j=1}^{J} (\nu''_{kj} - \nu'_{kj}) q_j \qquad (k = 1, ...,K) \tag{A.9}$$

Equation A.9 can in turn be used to solve the system of equations (S)provided by equations A.3 and A.4.

$$S \Leftrightarrow \begin{cases} \dot{m}(x_k - x_k^i) - r_k W_k V = 0 \\ \dot{m} \sum_{k=1}^{K} (x_k h_k - x_k^i h_k^i) + Q = 0 \end{cases} \tag{A.10}$$

For more details, consult references [20] & [21].

A.2 Numerical Procedure

The system of equations (S) is composed of $K + 1$ non linear algebraic equations. There are K equations provided by the species conservation equation A.3 and 1 equation by the energy conservation equation A.4. The unknowns are the K mass fractions and the combustion temperature T. The species molecular weight, enthalpy and entropy can be readily obtained from thermodynamic tables. The relevant chemical reactions can be selected form chemistry literature, which provide extensive information on the stoichiometric coefficients, the activation energy E_A and the Arrhenius coefficients A and β for each individual reaction. The forward and reverse rates can then be computed form equations A.7 and A.8 and the molar rate of production r_k from equations A.6 and A.9. Having obtained the above information, the system of equations can finally be solved.

In order to develop an accurate model for the combustion processes, a set of 90 chemical reactions (see ref. [27] & [26]) involving ethanol and oxygen were selected (they are listed in appendix B). These reactions were specially recommended for high pressure combustion

simulations. The software [20] utilized was specifically designed to determine the combustion equilibrium in a perfectly stirred reactor. It was provided by Sandia National Laboratories and is part of the CHEMKIN-II [21] chemical analysis software package.

The solver uses the damped modified Newton algorithm. In the case where convergence fails, the solution is further conditioned by a time integration. For more details on the numerical method, see references [20] & [21].

Appendix B

Ethanol/O_2 Reactions

Note: the chemical reactions are presented in the format utilized by the Chemkin-PSR code (see References [21] & [20]).

```
ELEMENTS H O C
END
SPECIES
H O2 OH O H2O CO CO2 CH3 CH4 CH2O HCO CH2 C2H4 CH
C2H6 C2H5 C2H3 C2H2 CH2CO C2H HCCO
C2H5OH CH3CHOH CH3CH2O CH3HCO H2CCH2OH
H2 HO2 CH2OH H2O2 HOCO
END
```

```
! The following reactions are from Warnatz, taken from the paper :
! CHEMISTRY OF HIGH TEMPERATURE COMBUSTION OF ALKANES UP TO OCTANE
```

```
! H-O2 Chain Propagation and Branching Reactions
```

!	A(cm,mol,s)	b	E(J/mole)
REACTIONS JOULES/MOLE MOLES			
H + O2 => OH + O	1.2e17	-.91	69.1e3
OH + O => H + O2	7.1e15	-.91	0
O + H2 => OH + H	1.5e7	2.0	31.6e3

129

OH + H => O + H2	6.7e6	2.0	23.3e3
OH + H2 => H2O + H	1.0e8	1.6	13.8e3
H2O + H => OH + H2	4.6e8	1.6	77.7e3
OH + OH => H2O + O	1.5e9	1.14	0
H2O + O => 2OH	1.5e10	1.14	72.2e3

! Recombination Reactions

H + H + M => H2 + M	1.8e18	-1.0	0

H2/1/ O2/.4/ CH/1/ CO/.75/ CO2/1.5/ H2O/6.5/

H + OH + M => H2O + M	2.2e22	-2.0	0

H2/1/ O2/.4/ CH/1/ CO/.75/ CO2/1.5/ H2O/6.5/

! Formation and Consumption of HO2

H + O2 + M => HO2 + M	2.0e18	-.8	0
H + HO2 => OH + OH	1.5e14	0	4.2e3
H + HO2 => H2 + O2	2.5e13	0	2.9e3
O + HO2 => OH +O2	2.0e13	0	0
OH +HO2 => H2O + O2	2.0e13	0	0

! Oxidation of CO

CO + OH => CO2 + H	4.4e6	1.5	-3.1e3
CO2 + H => CO + OH	1.6e14	0	110.0e3

! Formation and Consumption of CH4

CH3 + H => CH4	6.0e16	-1.0	0
CH4 + H => CH3 + H2	2.2e14	3.0	36.6e3
CH3 + H2 => CH4 + H	6.6e2	3.0	32.4e3
CH4 + O => CH3 + OH	1.2e7	2.1	31.9e3
CH3 + OH => CH4 + O	1.3e5	2.1	19.6e3
CH4 + OH => CH3 + H2O	1.6e6	2.1	10.3e3
CH3 + H2O => CH4 + OH	2.9e5	2.1	70.3e3

! CH3 Consumption

CH3 + O => CH2O + H	7.0e13	0	0

! CH2OH Consumption

CH2O + H => HCO + H2	2.5e13	0	16.7e3
CH2O + O => HCO + OH	3.5e13	0	14.7e3

CH2O + OH => HCO + H2O	3.0e13	0	5.0e3

! CHO Consumption

HCO + H => CO + H2	2.0e14	0	0
HCO + O => CO + OH	3.0e13	0	0
HCO + O => CO2 + H	3.0e13	0	0
HCO + OH => CO + H2O	5.0e13	0	0
HCO + O2 => CO + HO2	3.0e12	0	0
HCO + M => CO + H + M	7.1e14	0	70.3e3

H2/1.0/ O2/.4/ C2H2/1.0/ CO/.75/ CO2/1.5/ H2O/6.5/

! CH2 Consumption

CH2 + H => CH + H2	4.0e13	0	0
CH2 + O => CO + H + H	5.0e13	0	0
CH2 + O2 =>CO2 + H + H	1.3e13	0	6.3e3
CH2 + CH3 => C2H4 + H	4.0e13	0	0

! CH Consumption

CH + O => CO + H	4.0e13	0	0
CH + O2 => CO + OH	2.0e13	0	0

! Formation of C2 Hydrocarbons by CH3 Recombination

CH3 + CH3 => C2H6	2.4e14	-.4	0
CH3 + CH3 => C2H5 + H	8.0e13	0	111.0e3
CH3 + CH3 => C2H4 + H2	1.0e16	0	134.0e3

! C2H6 Consumption

C2H6 + H => C2H5 + H2	5.4e2	3.5	21.8e3
C2H6 + O => C2H5 + OH	3.0e7	2.0	21.4e3
C2H6 + OH => C2H5 + H2O	6.3e6	2.0	2.7e3
C2H5 + H => CH3 + CH3	3.0e13	0	0
C2H5 + O =>CH3HCO + H	5.0e13	0	0
C2H5 + O2 => C2H4 + HO2	2.0e13	0	20.9e3
C2H5 => C2H4 + H	2.0e13	0	166.0e3

! C2H4 Consumption

C2H4 + H =>C2H5	1.0e13	0	6.3e3
C2H4 + O => HCO + CH3	1.6e9	1.2	3.1e3

C2H4 + OH => C2H3 + H2O	7.0e13	0	12.6e3
C2H4 + H => C2H3 + H2	1.5e14	0	42.7e3

! C2H3 Consumption

C2H3 + H => C2H2 + H2	2.0e13	0	0
C2H3 + O2 => C2H2 + HO2	1.0e12	0	0
C2H3 => C2H2 + H	1.0e15	0	178.0e3

! C2H2 Consumption (abstraction reactions excluded)

C2H2 + H => C2H3	5.5e12	0	10.1e3
C2H2 + O => CH2 + CO	4.1e8	1.5	7.1e3
C2H2 + OH => CH2CO + H	3.0e12	0	4.6e3

! CH3HCO Consumption

CH3HCO + H => CH3 + CO + H2	4.0e13	0	17.6e3
CH3HCO + O => CH3 + CO + OH	5.0e12	0	7.5e3
CH3HCO + OH => CH3 + CO + H2O	1.0e13	0	0

! CH2CO Consumption

CH2CO + H => CH3 + CO	7.0e12	0	12.6e3
CH2CO + O => HCO + HCO	2.0e13	0	9.6e3
CH2CO + OH => CH2 + HOCO	1.0e13	0	0
CH2CO + M => CH2 + CO + M	1.0e16	0	248.0e3

! CHCO Formation and Consumption

C2H2 + O => HCCO + H	4.3e14	0	50.7e3
HCCO + H => CH2 + CO	3.0e13	0	0
HCCO + O => CO + CO + H	1.2e12	0	0

! C2H Formation and Consumption

C2H2 + H => C2H + H2	1.5e14	0	79.6e3
C2H2 + OH => C2H + H2O	1.0e13	0	29.3e3
C2H + O => CO + CH	1.0e13	0	0
C2H + H2 => C2H2 + H	3.5e12	0	8.8e3
C2H + O2 => CO + HCO	5.0e13	0	6.3e3

! The following reactions are from Westbrook, taken from the paper :
! SHOCK TUBE IGNITION OF ETHANOL, ISOBUTENE AND MTBE : EXPERIMENTS AND MODELING

132

! Ethanol Reactions

Reaction	A	n	E
C2H5OH + H = CH3CHOH + H2	4.47e6	2.0	2.1e4
C2H5OH + H = H2CCH2OH + H2	9.12e6	2.0	3.2e4
C2H5OH + H = CH3CH2O + H2	8.32e5	2.1	2.0e4
C2H5OH + O = CH3CHOH + OH	3.09e13	0.0	2.2e4
C2H5OH + O = H2CCH2OH + OH	2.24e13	0.0	3.2e4
C2H5OH + O = CH3CH2O + OH	4.79e13	0.0	2.9e4
C2H5OH + OH = CH3CHOH + H2O	6.76e7	1.61	1.5e2
C2H5OH + OH = H2CCH2OH + H2O	7.59e9	.97	6.6e3
C2H5OH + OH = CH3CH2O + H2	9.55e12	0.0	1.4e4
C2H5OH + CH3 = CH3CHOH + CH4	1.74e00	3.46	2.3e4
C2H5OH + CH3 = H2CCH2OH + CH4	3.16e1	3.17	3.0e4
C2H5OH + CH3 = CH3CH2O + CH4	1.45e1	3.10	2.9e4
C2H5OH + HO2 = CH3CHOH + H2O2	5.89e13	0.0	7.4e4
C2H5OH + HO2 = H2CCH2OH + H2O2	8.32e12	0.0	8.6e4
C2H5OH + HO2 = CH3CH2O + H2O2	0.0	0.0	0.0
H2CCH2OH = C2H4 + OH	3.24e14	−.24	1.4e5
CH3CHOH + M = CH3HCO + H + M	1.86e24	−2.5	1.4e5
CH3CHOH + O2 = CH3HCO + HO2	4.79e14	0.0	2.1e4
CH3CH2O = CH3 + CH2O	2.09e12	0.0	9.0e4

END

BIBLIOGRAPHY

[1] ANDERSON, W. E. "Spray Formation Processes of Impinging Jet Injectors". Tech. rep., Pennsylvania State University.

[2] AVAMPATO, T. J., AND SALTIEL, C. "Dynamic Modeling of Starting Capabilities of Liquid Propellant Rocket Engines". *Journal of Propulsion and Power, Vol. 11*, No. 2 (March-April 1995), pp. 292–300.

[3] BECKER, M. *Heat Transfer: A Modern Approach*. Plenum Press, 1986, ch. 9.

[4] BONNIE, M. B. "Thermodynamic properties to 6000 K for 210 substances involving the first 18 elements.". Tech. rep.

[5] EPSTEIN, A. "Micro-Heat Engines, Gas Turbines, and Rocket Engines", 1997. AIAA 97-1773.

[6] FRÉCHETTE, L. G. 1998. Personal Communications.

[7] HAMROCK, B. J. *Rocket Propulsion Elements*. McGraw-Hill, Inc., 1994, ch. 11.

[8] HAMROCK, B. J. *Rocket Propulsion Elements*. McGraw-Hill, Inc., 1994, ch. 12.

[9] HOLMAN, J. P. *Heat Transfer*, 7 ed. McGraw Hill, 1990, ch. 6.

[10] HOLMAN, J. P. *Heat Transfer*, 7 ed. McGraw Hill, 1990, ch. 4.

[11] I.A. WAITZ, F.E. MARBLE, E. Z. "A Systematic Experimental and Computational Investigation of a Class of Contoured Wall Fuel Injectors".

[12] KAMATH. "Parabolized Navier Stokes Algorithm for Chemically Reacting Flows", 1989.

[13] KERREBROCK, J. L. *Aircraft Engines and Gas Turbines*, 2 ed. The MIT Press, 1992, ch. 5,6.

[14] LONDON, A. "Microfabricated Liquid Bipropellant Rocket Engines". Ninth Annual NASA-JPL Advanced Propulsion Research Workshop.

[15] LONDON, A. P. "A System Study of Propulsion Technologies for Orbit and Attitude Control for Microspacecraft". Master's thesis, MIT, May 1996.

[16] LONDON, A. P., 1997. Personal Communications.

[17] LOPATA, J. B. 1998. Personal Communications.

[18] MUNSON. *Fundamentals of Fluid Mechanics*, 2 ed. John Wiley & Sons, Inc., 1994, ch. 12.

[19] NAGLE, S. F. "Design of an Electrostatic Induction Machine for the Micro Gas Turbine". Gtl presentation document, Massachusetts Institute of Technology, 1997.

[20] P. GLARBORG, R. J. KEE, J. F. G., AND MILLER, J. A. *PSR: A Fortran Program for Modeling Well-Stirred Reactors*. Sandia National Laboratories, Albuquerque, New Mexico 87185 and Livermore, California 94551, June 1995. SAND86-8209.

[21] R. J. KEY, F. M. R., AND MILLER, J. A. *CHEMKIN-II: A Fortran Chemical Kinetics Package for the Analysis of Gas-Phase Chemical Kinetics*. Sandia National Laboratories, Albuquerque, New Mexico 87185 and Livermore, California 94551, September 1989. SAND89-8009.

[22] RODER, H. M., AND WEBER, L. A. "ASRDI Oxygen Technology Survey: Thermophysical Properties". NASA SP- 3071, 1972.

[23] SCHETZ, J. A. *Injection and Mixing in Turbulent Flow*. AIAA, 1980, ch. 8.

[24] SUTTON, G. P. *Rocket Propulsion Elements*, 6 ed. John Wiley & Sons Inc., 1992.

[25] TCC. "Thermo-Chemical Calculator". http://adam.caltech.edu/cgi-bin/tcc.

[26] TWENTIETH SYMPOSIUM (INTERNATIONAL) ON COMBUSTION / THE COMBUSTION INSTITUTE. *Chemistry of High Temperature Combustion of Alkanes up to Octane* (1984). pp. 845-856.

[27] TWENTY-FOURTH SYMPOSIUM (INTERNATIONAL) ON COMBUSTION / THE COMBUSTION INSTITUTE. *Shock Tube Ignition of Ethanol, Isobutene and MTBE: Experiments and Modelling* (1992). pp. 769-776.

[28] WHITE, F. *Viscous Fluid Flow.* McGraw-Hill, 1991.

[29] WU, P.-K., AND CHEN, T. H. "Injection of Supercritical Ethylene in Nitrogen". *Journal of Propulsion and Power, Vol. 12* (July-August 1996).